UNIVERSITY OF CALIFORNIA, SAN DIEGO

Tailored Charged Particle Beams from Single-Component Plasmas

A dissertation submitted in partial satisfaction of the
requirements for the degree
Doctor of Philosophy

in

Physics

by

Tobin Robert Weber

Committee in charge:

Professor Clifford M. Surko, Chair
Professor Farhat Beg
Professor Fred Driscoll
Professor Thomas O'Neil
Professor George Tynan

2010

The dissertation of Tobin Robert Weber is approved, and it is acceptable in quality and form for publication on microfilm and electronically:

_____

_____

_____

_____
Chair

University of California, San Diego

2010

EPIGRAPH

All things are flowing

—Heraclitus? quoted by Aristotle

TABLE OF CONTENTS

---

[1]This Chapter is based upon the paper, T. R. Weber, J. R. Danielson and C. M. Surko, Phys. Plasmas, 012106 (2008). Mr. Weber was the lead scientist on this work.

[2]This Chapter is based upon the paper, T. R. Weber, J. R. Danielson and C. M. Surko, Phys. Plasmas, 057105 (2009). Mr. Weber was the lead scientist on this work.

LIST OF FIGURES

LIST OF TABLES

ACKNOWLEDGEMENTS

The past six years of my life have been some of those most fruitful I have ever had thanks to many people. First and foremost, I would like to thank my advisor Cliff Surko for not only giving me the opportunity to work with a high quality research group, but for caring enough to see me develop as a scientist. I would also like to thank James Danielson and Gene Jerzewski for taking the time to explain things to me and help me at every point along the way. I am further eternally grateful to all the professors at UCSD for helping me learn physics at a deeper level. Patrick Diamond, Anesh Manohar and Tom O'Neil, to name a few. Last but not least, I would like to thank my parents for raising and supporting me, and the members of my committee for their service.

2003	B. S., Physics, University of Wisconsin-Madison.
2004-2005	Teaching Assistant, University of California, San Diego.
2005	M. S., Physics, University of California, San Diego.
2005-2010	Research Assistant, University of California, San Diego.
2010	Ph. D., Physics, University of California, San Diego.

PUBLICATIONS

T. R. Weber, J. R. Danielson, and C. M. Surko, "Energy Spectra of Tailored Particles Beams from Trapped Single-Component Plasmas", *Physics of Plasmas* **16**, 051705 (2009).

T. R. Weber, J. R. Danielson, and C. M. Surko, "Creation of Finely Focused Particles Beams from Single-Component Plasmas", *Physics of Plasmas* **15**, 012106 (2008).

J. R. Danielson, T. R. Weber, and C. M. Surko, "Extraction of Small-Diameter Beams from Single-Component Plasmas", *Applied Physics Letters* **90**, 081503 (2007).

J. B. Boffard, B. Chiaro, T. Weber, and C. C. Lin, "Electron-Impact Excitation of Argon: Optical Emission Cross Sections in the Range of 300-2500 nm", *Atomic Data and Nuclear Data Tables* **93**, 831-863 (2007).

J. R. Danielson, T. R. Weber, and C. M. Surko, "Plasma Manipulation Techniques for Positron Storage in a Multicell Trap", *Physics of Plasmas* **13**, 123502 (2006).

T. Weber, J. B. Boffard, and C. C. Lin, "Angular Momentum Coupling and Electron-Impact Excitation Cross Sections of Rare-Gas Atoms", *International Journal of Mass Spectrometry* **233**, 75 (2004).

T. Weber, J. B. Boffard, and C. C. Lin, "Electron-Impact Excitation Cross Sections of the Higher Argon 3p5np, (n=5,6,7) Levels", *Physical Review A* **68**, 032719 (2003).

ABSTRACT OF THE DISSERTATION

Tailored Charged Particle Beams from Single-Component Plasmas

by

Tobin Robert Weber

Doctor of Philosophy in Physics

University of California, San Diego, 2010

Professor Clifford M. Surko, Chair

There are currently many uses of positrons as well as a strong potential for
novel applications on the horizon. Due to the scarce nature of antimatter, positron
research and technology is frequently limited by the ability to collect, confine,
and manipulate antiparticles. Trapping large numbers of positrons as nonneutral
plasmas has proven ideal in this endeavor. This thesis focuses on exploiting the
attractive properties of single-component positron plasmas to develop new tools
for antimatter research.

A Penning-Malmberg trap is used to confine single component electron
(used for increased data rate) plasmas. The trap consists of a cylindrical electrode
structure, centered in the bore of a superconducting magnet. The superconducting
magnet supplies a uniform 5 tesla field that provides radial confinement, while
voltages applied to both ends of the electrode structure confine the plasma axially.
The trap exhibits long confinement times ($\sim$ days) and low plasma temperatures
($T < 20$ meV).

The focus of this thesis is the development of a nondestructive technique
to create narrow beams with narrow energy spreads and transverse spatial widths

from single-component plasmas in a Penning-Malmberg trap. This technique is valuable for effectively and efficiently utilizing trapped positrons. Beams are extracted by carefully lowering the confining trap potential V_C on one end to some extraction voltage V_E. Due to the plasma space charge, beam pulses ($\triangle t < 10$ μsec) emerge from near the plasma center with radii as small as $\rho_b = 2\lambda_D$ (HW 1/e), and energy spreads $\triangle E \sim T$. Through cyclotron radiation and the rotating wall, the plasma temperature and density is tailored such that beams are narrow ($\rho_b = 2\lambda_D$) and cold ($\triangle E \sim T$), resulting in quality beams of a low emittance.

A simple nonlinear model is used to derive equations predicting a wide range of beam properties from only the plasma parameters and V_E. An expression is first derived for the radial profile of the beam $\sigma_b(r)$. A relation for the total number of escaping particles as a function of V_E, $N_b(V_E)$, is developed. From this expression, the full energy distribution of the beam $f(E_\parallel, E_\perp)$ is obtained, where $E_\parallel$ and $E_\perp$ are the kinetic energies in direction parallel and perpendicular to the magnetic field. The equations are generically written in terms of the scaled beam number $\xi = e^2 N_b / L_p T$, extraction voltage $\eta = (V_E - \phi_0(0))/T$, and electrode radius R_W/λ_D, only. Here, L_p is the plasma length. The resulting expressions are verified experimentally over a wide range of ξ and R_W/λ_D. General trends in the RMS energy spread of the beams $\triangle E$ are discussed. The extraction of more than 50 % of a trapped plasma into a train of nearly identical beams is demonstrated.

The techniques described above result in beams in a high (e.g., several tesla) magnetic field. However for many applications, such as atomic-physics scattering experiments and the creation of microbeams by electrostatic focusing and remoderation, beams in a magnetic-field free region are desired. For these applications, a technique is described to create high-quality electrostatic beams by extracting the initial beam from the confining magnetic guide field. The beam is first adiabatically transferred to a low field region, then brought through a magnetic shield to a region of zero field by means of a nonadiabatic fast extraction. Once in this zero field region, the beam is focused to smaller transverse dimensions using an electrostatic (Einzel) lens. This technique is shown to produce quality electrostatic beams in an efficient and reproducible way. Potential applications and the pos-

sibilities for further advances in magnetically guided and electrostatic beams are discussed.

Finally, results of RW compression in low fields ($B = 2$ T) are briefly reported. Difficulties encountered while operating the RW in low fields (e.g., $B = 2$ T) are presented and discussed.

Chapter 1

Introduction

Although our world is composed exclusively of matter, antimatter is created naturally during high energy processes when the energies involved exceed the rest mass of an antiparticle ($E > mc^2$). With recent progress in antimatter research such as antihydrogen formation, positron (antielectron) microscopy, and the formation of positron molecule bound states, future prospects for antimatter are both bountiful and exciting [2, 15, 3]. Unfortunately, current antiparticle sources (e.g., radioactive isotopes or high energy accelerators) are a major impediment to progress in these areas as they are seriously limited in both current ($J \sim 100$ pA) and energy spread ($\triangle E \sim 1$ MeV). Sophisiticated schemes (e.g., moderators) employed to decrease the energy spread of the positrons are met with major difficulties as these volatile particles readily annihilate with electrons, their matter counterpart. Fortunately, a Penning-Malmberg trap has proven an effective tool to improve positron sources by trapping and cooling antiparticles emitted from an afore mentioned high energy process [25, 59]. Once large numbers are trapped and cooled, positrons can be used for a wide variety of applications [25, 59]. This thesis explores the exciting possibilities for exploiting the wonderful properties of a Penning-Malmberg trap to create high quality effective positron sources and drive antimatter research and technology.

1.1 Antimatter applications

The unique charge and mass of a positron make it an attractive tool to explore basic physics and develop new technological applications. A positron's electron mass ($m_{e+} = m_e$) and positive charge ($q_{e+} = +e$) creates a landscape of new physical systems to investigate. For example, recently at UCSD we have discovered positron molecule bound states that occur as a positron induces, and is attracted to, a dipole polarized molecule [3]. Further, a positron can bind to an electron, creating an extremely light boson known as positronium. This unique, short lived boson has opened up a wealth of new physical systems to investigate including excited positronium states and di-positronium molecules [10, 34, 8].

Additionally, positrons possess the unique and exciting property that they annihilate with electrons and produce gamma rays. This property creates a tremendous potential for technological applications. One powerful example of this is the use of positrons to probe surfaces [63, 38]. While ionization, auger emission, and scattering by a positron beam are effective tools for analyzing a surface, a more powerful technique is in measuring the annihilation lifetime of the positron in the material [15]. These lifetimes are incredibly sensitive to small defects in materials, and easily measured to high accuracies by recording the emitted gamma ray. By scanning a positron beam across a surface and recording the annihilation lifetimes, a wealth of information comes available that is inaccessible to a scanning electron microscope.

Further, there is a serious effort at CERN to create antihydrogen [2]. Antihydrogen consists of an antiproton and positron bound together in an atom. By combining trapped positrons and antiprotons, antihydrogen has been created at CERN. Presently, the challenge is to cool and trap the atoms with non-uniform magnetic fields. Once captured, plans are in place to perform spectroscopy on the atom and measure the atomic energy levels. This measurement would constitute a extremely precise test of the fundamental CPT symmetry of nature [7].

There are still many exciting positron applications on the horizon. One exciting possibility is the formation of a Bose-Einstein condensate from positronium [44]. Positronium's light mass and boson nature allow for the possibility to

achieve Bose-Einstein condensation at relatively high temperatures ($T \sim 300$ K). The creation of Bose-Einstein condensed positronium brings the possibility of a gamma ray laser. This could be achieved via stimulated emission of a dense cloud of positronium atoms into a coherent gamma ray source. While many hurdles most be overcome before this is a reality, none are insurmountable. Finally, a great potential exists to use positrons to diagnosis plasmas [61]. By injecting positrons into a known region of a plasma, the particles serve as an electron mass test particles to measure transport. A measurement could be made by recording the gamma rays emitted as the positrons reach the wall and annihilate.

Many positron applications exists, and there are great possibilities for the future. But as you will see in the next section, these applications are limited by the positron source, which currently has serious restrictions.

1.2   Antimatter sources

The two main challenges facing positron applications are the lack of bright positron sources and the difficulties involved in working with a particle that annihilates with matter. Because positrons do not readily exist in the world, sources must be created from pair production (e^- and e^+) in high energy processes. Examples of these are collisions of accelerated electrons with a high Z-material [28, 19], interactions with intense laser fields [48], and matter interactions with the bright flux of high energy photons and neutrons emitted from nuclear fission reactors [31, 26]. Such sources can achieve slow positrons fluxes of at most $\approx 10^9$/sec ($J \approx 100$ pA).

Another positron source is radioactive isotopes that emit positrons naturally during their decay process. This commonly used source is superior to high energy accelerator and reactor sources in simplicity, cost, and convenience. For many reasons, a popular source is sodium-22. One reason is that the half life of ^{22}Na is 2.6 years, allowing for continual use over several years. Secondly, over 90% of all decays in ^{22}Na produce positrons, resulting in high positron outputs. Finally, in comparison to other radioactive isotopes, ^{22}Na has a low cross section to absorb positrons. This further increases the outward flux of positrons, as less are lost in

the sodium by reabsorbtion.

For all sources, positrons are born at high energies ($\sim$ MeV) with large energy spreads ($\sim$ MeV). This is undesirable and creates many challenges for applications that require cold beams (e.g., $T \approx 25$ meV) with low mean energy (e.g., $E \sim 50$ V). To address this problem, positrons are typically cooled to low energies ($\sim$ eV) via a moderator, or a solid material that positrons can efficiently lose energy in while avoiding annihilation in some cases [47]. In typical moderators, positrons will thermalize through ionization, hole creation, and phonon creation [33]. One common material used for a moderator is a thin metal film, such as tungsten. However, $\approx 99.9\%$ of incident positrons are lost to annihilation in these materials. A superior moderator is one made of a solid nobel gas. Such moderators have superior efficiencies ($> 1\%$ of incident positrons cool and avoid annihilation), and can produce slow positron beams of sub eV temperatures [46]. For example, by freezing neon onto the surface of a cold head, a high quality moderated radioactive source, with low energy positron currents of $\approx 5 \times 10^6$/sec ($J \approx 1$ pA), has been achieved [37, 66].

Unfortunately, moderated radioactive sources leave much to be desired. As mentioned, they are still limited by weak currents and have unusably high energy spreads (~ 1 eV) for some applications. However, if positron trapping is used in conjunction with the moderated source, positron currents can be increased, and energy spreads lowered. By gathering and cooling large numbers of positrons in a charged particle trap, an effective bright source of low energy positrons is created. The Surko group at UCSD has perfected this technique with a Surko buffer gas positron trap [47]. Although the details of the trap will not be discussed here, the trap produces bright pulses (10^8) of low energy positrons ($\triangle E \sim 300$ K) that originate from a moderated radioactive source. This style of trap is used all over the world, and has led to the discovery of many new facets of positron physics including positron molecule bound states [3]. Positron molecule bound states, for example, are unobservable with moderated radioactive positron sources alone.

This thesis will focus on new positron trapping tools to produce high quality, effective positron sources to help drive current antimatter research.
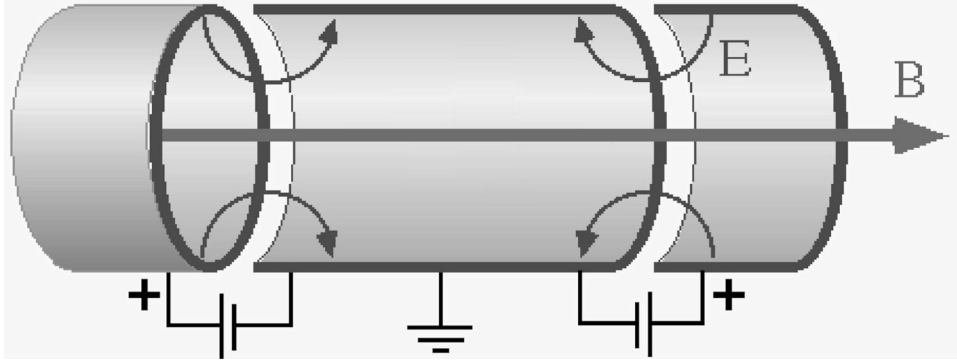
Figure 1.1: A generic Penning-Malmberg trap.

1.3 Penning-Malmberg trap: future positron source

For many reasons that will be explained shortly, a Penning-Malmberg trap is a superior choice for trapping positrons. A generic Penning-Malmberg trap is illustrated in Fig. 1.1 and consists of a uniform magnetic field through a cylindrical electrode structure. A positron is confined radially by the magnetic field and axially by electric fields generated at both ends by applying confinement voltages V_C to the two end electrodes. This is one of the fundamental trapping principles behind the Surko buffer gas trap.

A truly great body of work has been done investigating electron trapping in Penning-Malmberg traps [17, 50, 49]. Fortunately, the physics is literally identical for positrons. By simply flipping the sign of the confinement voltage and magnetic field, all electron results apply identically to positrons. One landmark result from this extensive work is that by injecting large numbers of electrons into the trap, it is possible to create a trapped nonneutral plasma (plasma of a single sign of charge) in thermal equilibrium [50]. In equilibrium, these nonneutral plasmas are uniform density rigid rotors, with a frequency that is proportional to the density n_0. The plasma rigidly rotates from the $E \times B$ drift motion resulting from the large radial electric fields generated by the column of nonneutral charge.

Perhaps the most remarkable property of these trapped plasmas is that they are confined in a state of thermal equilibrium [50]. Specifically, they relax into thermal equilibrium in the rotating frame of the plasma. Potential surfaces

of constant radius contain a local maxwellian velocity distribution in the rotating frame of the plasma. This amazing property is exclusive to nonneutral plasmas. It is impossible to confine a neutral plasma in thermal equilibrium using electric and magnetic fields, a fact that has plagued magnetic confinement fusion for decades.

All of these properties make the Penning-Malmberg trap a perfect antimatter trap and allow for the creation of high quality effective positron sources. The latter point refers to the potential to gather a large number of positrons into the trap, allow the particles to cool, then extract the particles in one bright pulse. This idea is the main focus and motivation of this work.

1.4   Experimental overview

All the work presented here was done on the Penning-Malmberg trap illustrated schematically in Fig. 1.2. This trap is known as the "High Field trap" for its high magnetic field of 5 T generated by a superconducting magnet. In Fig. 1.2, note the presence of a cylindrical electrode structure and uniform magnetic field. These are the two stables of a Penning-Malmberg trap. In this work, we will be using a cylindrical coordinate system (r, θ, z) where the z-axis corresponds to the axis of cylindrical symmetry of the electrodes. As mentioned in Sec. 1.3, particles are confined radially by the uniform magnetic field, and axially by electric fields that are generated at both ends by confinement voltages V_C applied to end electrodes.

The large trapping magnetic field of the HF trap has a number of beneficial properties. In addition to increasing the plasma confinement time, the cooling time of the particles τ_c decreases dramatically as $\tau_c \propto 1/B^2$ [5, 4]. This is because the plasma primarily cools via cyclotron radiation of the charged particles. In the 5 tesla field, the plasma cooling time is approximatley $\tau_c \approx 150$ msec. There are many great benefits to short cooling times. In addition to decreasing the time required to wait for particles to cool and then be used, the large cooling power will routinely dominate any external heating sources, allowing the plasma to cool to the temperature of the walls. When strong external heating sources are present,
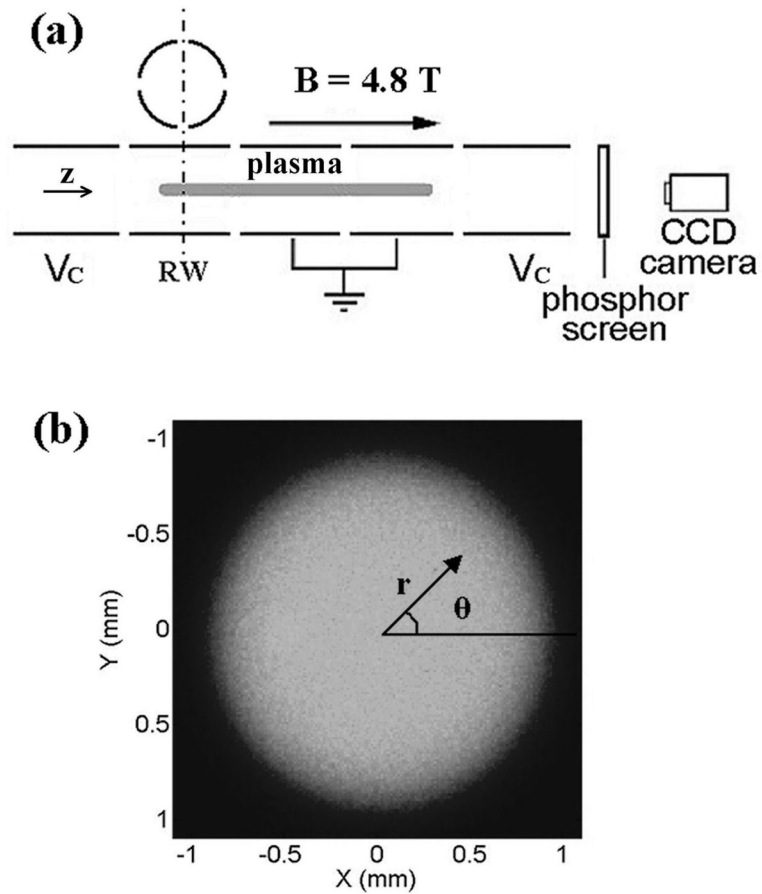
Figure 1.2: (a) Schematic diagram of the experimental arrangement and (b) a CCD image of the areal z-integrated plasma density distribution $\sigma_z(r, \theta)$ for an equilibrium "flat-top" plasma.

like from the "Rotating Wall" discussed shortly, large cooling powers are critical.

The main diagnostic tool used on this device is a CCD camera and phosphor screen located outside the trap. By dropping V_C to zero on one end, the plasma exits the trap by streaming along field lines, and collides with the phosphor screen emitting light. This light is imaged using the CCD camera. Because the plasma is in a highly magnetized state, the particles stay glued to their respective field lines thus making the images z-integrated density profiles of the plasma inside the trap. An example of a z-integrated plasma profile $\sigma_z(r, \theta)$ is shown in Fig. 1.2. Note that for plasmas with large aspect ratios ($L_p/R_p \gg 1$, Lp being the plasma length, R_p the plasma radius), the plasma is approximately z-independent with flat ends.

With this property, one can simply divide the z-integrated plasma density profile by L_P to approximately obtain the 3 dimensional density profile of the plasma inside the trap $n(r, \theta, z) = \sigma_z(r, \theta)/L_P$. Although this is a destructive measurement, the trap exhibits excellent shot to shot reproducibility ($\Delta N/N \leq 5$ %), allowing for multiple measurements of a given plasma configuration.

Another exciting property of this trap is that the electrodes are thermally connected to a cold head and have the potential to be cooled to as low as 10 K. This creates the possibility of a trapped cryogenic positron plasma if the plasma is quiescent enough to cool to the temperature of the surrounding electrodes. One difficulty with cooling plasmas to cryogenic temperatures is that the cooling power (cyclotron cooling) is proportional to the plasma temperature T [5]. To cool a trapped plasma, cyclotron cooling has to exceed any external heating sources. Thus, cold plasmas are more vulnerable to external heating sources when trying to, for example, cool to the wall temperature. As a result, great care must be taken in isolating the plasma from any external heating sources when cooling to temperatures $T < 25$ meV. Previously, groups have achieved liquid helium temperature trapped plasmas by submerging an entire trap in a dewar of liquid helium [5]. In this way, the plasma is completely isolated from any external non-cryogenic black body radiation. Unforunatley, this is not the case here. An unavoidable external heating source here is room temperature black body radiation that enters from the ends of the trap. At this point, it remains unclear if the trapped plasmas here can be cooled to cryogenic temperatures. On this trap, plasmas have been cooled to $T < 200$ K. At these temperatures, the plasma temperature becomes very difficult to measure, so uncertainty remains as to how far below 200 K the plasma is. However, the important question is if external heating sources are keeping the plasma from cooling below 200 K, is it possible to eliminate them? Until these questions are answered, the effectiveness of this experimental arrangement to achieve cryogenic plasmas remains an unknown.

Lastly, this trap has a wonderful tool called the "Rotating Wall" (RW), illustrated schematically in Figs. 1.3. The RW consists of one electrode divided into 4 electrically isolated sectors. Each sector receives a different phase of a time
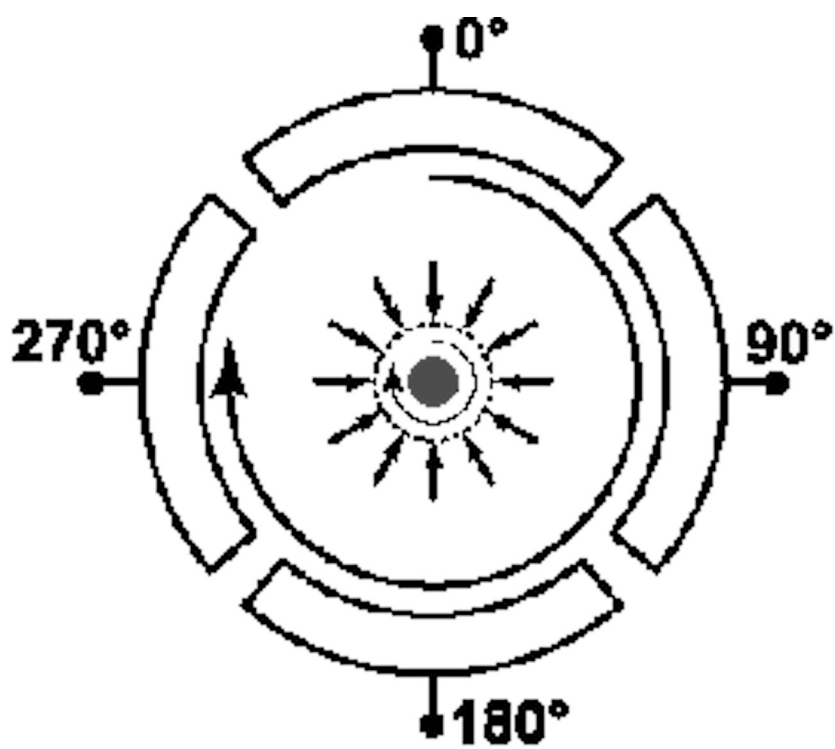
Figure 1.3: Schematic of the sectored RW in the HF trap.

varying, sinusoidal voltage. The phase of the sinusoid is fixed to match the θ value at which the center of the respective sector resides. The net result is that in the trap, the plasma sees an azimuthally asymmetric potential that appears to be rotating azimuthally in time, hence the name, "Rotating Wall". In this work, the "strong drive" regime will be exploited [13]. The strong drive regime occurs when the voltage of the applied sinusoid V_{RW} is sufficiently large ($V_{RW} \approx 1$ V) such that the plasma spins up or down to match the frequency of the applied sinusoid. Because frequency is proportional to density, this results in either a compression or expansion of the plasma. An example of this tool in use is shown in Fig. 1.4, where the plasma is compressed up by a factor of 10. Here a slice of constant θ from σ_z is plotted. Note that this tool varies the density in an in-situ, non-destructive manner. This is beneficial for two major reasons. One is that it counteracts the natural expansion of the plasma due to unavoidable trap asymmetries, allowing the plasma to be confined indefinitely ($\tau \sim$ days). The other advantage of the RW is it allows for direct control of the plasma density when performing experiments.

The experiment just discussed is an excellent trap for positrons. Large numbers of positrons (10^{10}) have been confined for long periods of times ($\tau \sim$ days) and at low temperatures ($T < 20$ meV). As a result, a great potential exists for these traps to serve as effective positrons sources that could help drive positron research [59]. However, most positron applications require more than just large numbers of trapped positrons. Typical positron applications, both current and future, requires or will require high quality positron beams of small spatial width, low energy spread, high brightness, and good reproducibility. The question this work will address is if these HF Penning-Malmberg traps are capable of providing such high quality beams.

A short aside before we continue: As mentioned earlier, in the Surko lab we have a wonderful positron source known as the Buffer Gas Trap. Using this trap, we are very confident in our ability to load positrons into the HF trap. However, in this work we will only trap electrons for increased data rate, and so as to leave the Buffer Gas trap free for other positron research.
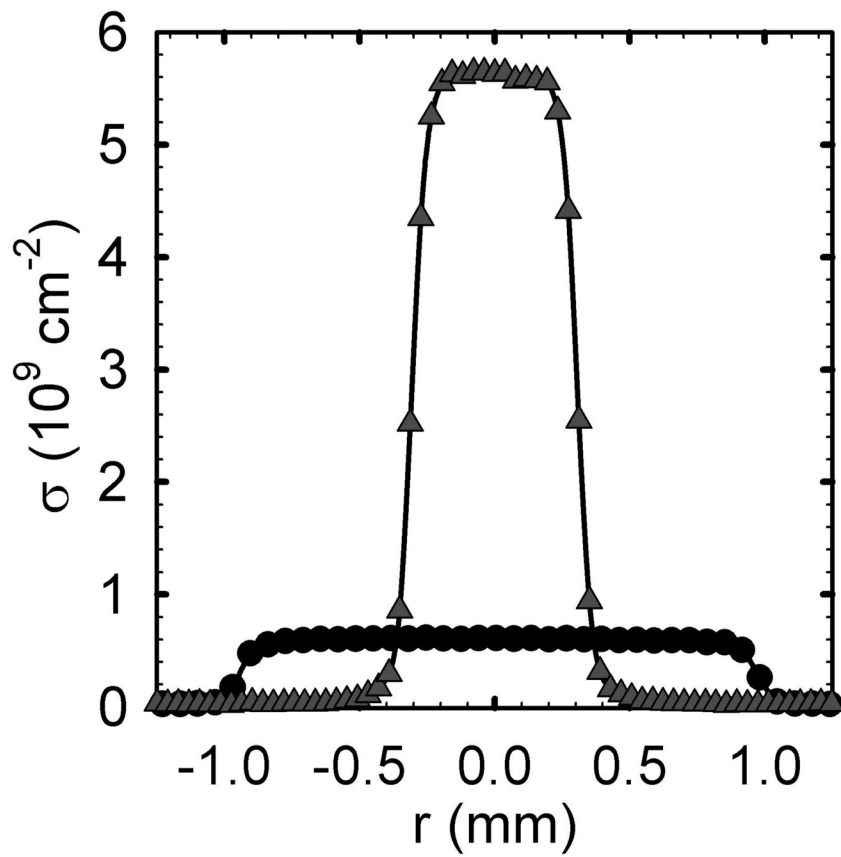
Figure 1.4: Example of plasma compression by a factor of 10 using the RW.

1.5 Outline of the dissertation

Chapter 2 will present a technique to extract high quality, tailored beams from trapped nonneutral plasmas. A simple model of the beam creation process is introduced and used to derive expressions for the transverse profile of the beam $\sigma_b(r)$. Predictions are verified using electron plasmas in the HF trap. The ability to extract multiple beams from the trapped plasmas and efficiently use an entire population of trapped particles is also demonstrated.

Next, Ch. 3 will address the energy spreads of the beams. Using the same simple model of the beam creation process, the full beam energy distribution function will be derived. Additionally, an expression will be developed for the total number of beam particles, given only the plasma parameters and extraction voltage V_E. These predictions will also be verified on the experiment using electron plasmas. Beams will be shown to have energy spreads on the order of the parent plasma $\triangle E \approx T$.

Chapter 4 will describe a technique to create electrostatic beams, or beams in a magnetic field free region, from plasma originating in a high magnetic field. Beams are extracted from the HF in two stages: A slow reduction in the field, followed by a fast extraction to zero field. A full theoretical treatment will be presented, deriving the modifications to the beam energy and spatial distributions from the magnetic extraction process. Once extracted from the field, the beam is focused with an Einzel lens to smaller transverse dimensions.

Finally, Ch. 5 briefly reports the results of RW compression in low magnetic fields (e.g., $B = 2$ T), followed by a short summary and conclusion in Ch. 6.

Chapter 2

Beam extraction [1]

This Chapter describes a protocol for generating high quality magnetized beams from plasmas in a Penning-Malmberg trap. The physics of the beam creation process is illustrated through a simple model from which many properties of the beams are derived. These predictions are all verified using electron plasmas on the device discussed in Sec. 1.4.

2.1   Experimental procedure

The beam extraction method is simple and illustrated in Fig. 2.1. By carefully lowering the confinement voltage V_{C} on one end to some extraction voltage V_{E}, particles with sufficient energy escape. These escaping particles constitute the beam. Because the equilibrium plasma potential $\phi_0(r)$ is quadratic in r, escaping particles come exclusively from the plasma center where $|e\phi_0(r)|$ is the largest [53].

A cartoon is shown in Fig. 2.2 to further illustrate the extraction process. Notice that while electrons at the center do not possess enough energy to pass over the confinement potential, when V_{C} is lowered on one end to V_{E}, some particles escape axially on that side. To reiterate, the escaping particles are the ones near $r = 0$, where the potential energy of the charged particles is the largest. This is illustrated in Fig. 2.2, where an image of the plasma before and after the beam

---

[1]This Chapter is based upon the paper, T. R. Weber, J. R. Danielson and C. M. Surko, Phys. Plasmas, 012106 (2008). Mr. Weber was the lead scientist on this work.
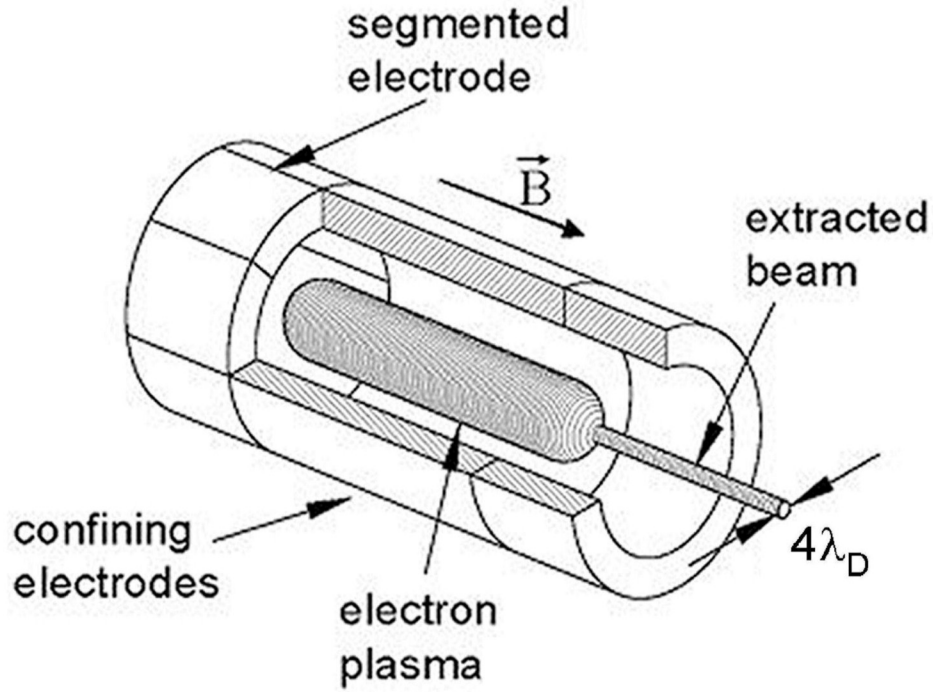
Figure 2.1: Simplified schematic diagram of the technique used to extract beams with small transverse spatial extent.

extraction process is shown. Notice the small divot or hole in the center of the plasma. This represents a depleted region where the escaping beam particles have left.

Once out of the trap, the beam is measured in two ways. The main diagnostic is using the CCD camera and phosphor screen to image the beam in the same way that the plasma is imaged. This is accomplished by allowing the beam to collide with the phosphor screen, then imaging the emitted light creating z-integrated transverse beam profiles $\sigma_{\mathrm{b}}(r)$. This z-integrated quantity is assumed to be azimuthally independent, therefore θ is suppressed. The second type of measurement is to record the voltage signal on the aluminum coating of the phosphor screen as the beam collides there. This voltage is related to the total number of beam particles N_{b} through the capacitance of the system. By taking the time derivative of this signal, the beam current is additionally obtained. Figure 2.3 illustrates examples of these two beam measurements. In Fig. 2.3, note that the beam is smaller than the width of the parent plasma, and occupies a temporal

(a)

(b)
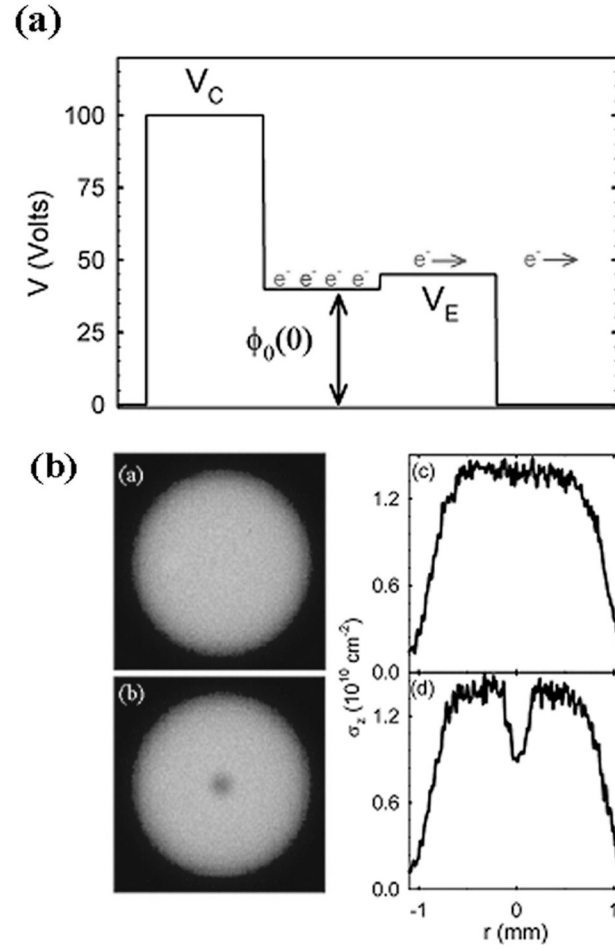
Figure 2.2: (a) Schematic diagram of the beam extraction process and (b) camera images of the areal z-integrated plasma density $\sigma_z(r,\theta)$ for a flat top plasma before beam extraction (above) and 10 μ sec after beam extraction (below); also shown are the corresponding radially averaged slice distributions $\sigma_z(r)$.

width of $\approx 5\ \mu$sec.

As illustrated in Fig. 2.3, the extraction voltage is set by a voltage pulse of width $\triangle t \approx 10\ \mu$sec. This time is determined as the minimum time required for all escaping particles to exit the trap. Because particles are streaming axially along field lines and bouncing off the confining potential barrier, a rough lower limit for this pulse time is $\Delta t \geq \tau_b \equiv 2L_{\mathrm{p}}/v_{\mathrm{t}}$, where τ_{b} is the "bounce time" required for an electron with the thermal velocity $v_{\mathrm{t}} = (T/m)^{1/2}$ to travel the distance $2L_{\mathrm{p}}$. Here, the minimum pulse width is determined empirically as the minimum time required to maximize the signal on the phosphor screen. The extraction window is minimized subject to this constraint to avoid instabilities, radial transport or collisions that might occur during the beam extraction process. The upper limit on this window to avoid these effects is discussed in more detail in Sec. 2.4. As seen in Fig. 2.3, the entire current pulse occurs within the extraction window, verifying that no escaping particles remain in the trap.

The time dependence of the beam current $I(t)$ in Fig. 2.3 is of interest to applications where pulses with a short time duration are required [11, 40, 27]. In other applications, however, the time dependence of the beam pulse is not important [3]. The beam extraction procedure described here produces beams that exit the trap with an initial temporal width Δt_0 roughly equal to the bounce time of a typical escaping particle (i.e., $\Delta t_0 \approx 2L_{\mathrm{p}}/v_{\mathrm{t}}$ for an exiting particle with axial velocity v_{t}). For the beams studies here, $2L_{\mathrm{p}}/v_{\mathrm{t}} \leq 1\ \mu$sec. Because these beams contain particles with a distribution of axial velocities, the pulse width will increase as the beam travels away from the trap. This is likely the dominant effect responsible for pulse width shown in Fig. 2.3.

Note that no particles are lost in this extraction process. It is a non-destructive process that conserves particles. This is an important feature for anti-matter applications where it is of critical importance to conserve what few particles one actually collects.
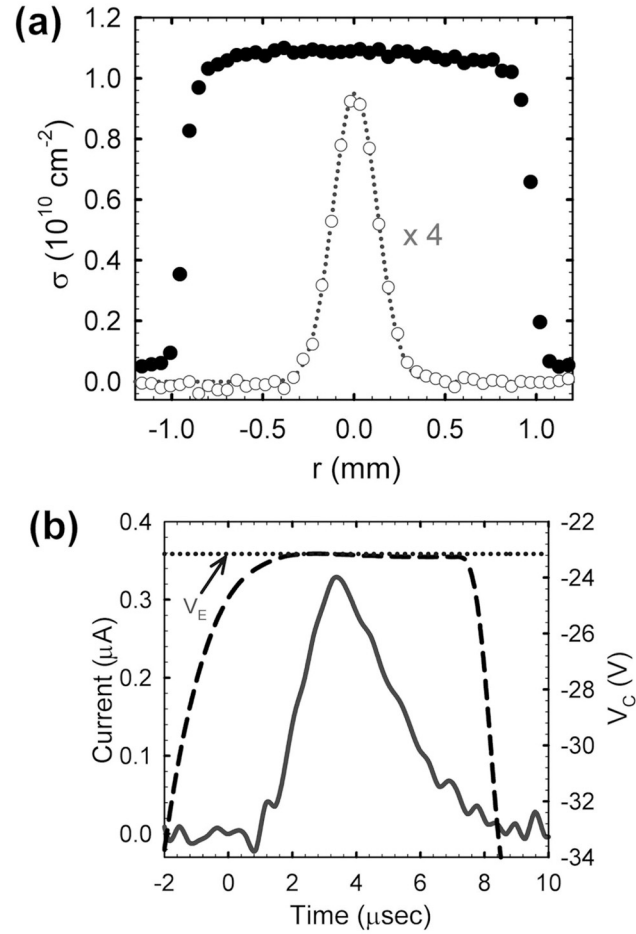
Figure 2.3: Examples of two beam diagnostics: (a) image of the beam with the CCD camera and phosphor screen and (b) measurement of the total charge on a collector screen. Here, a time derivative of the signal, or beam current, is plotted along with the confinement potential $V_C(t)$ (- - -). The value of V_E ($\cdots$) for this extraction is also shown.

2.2   Theoretical description

In this section, expressions are developed for the areal distribution $\sigma_b(r)$ of electron beams extracted from a Penning-Malmberg trap. To apply these results to positron beams, change e to $-e$ in the formula below. A final reminder: this work assumes z and θ independence so all quantities are written in terms of r only.

For a charged particle in a nonneutral plasma in equilibrium inside a Penning-Malmberg trap, the minimum velocity parallel to the magnetic field $v_{\parallel\text{min}}$ that a particle requires to escape is set by the escape condition,

$$\frac{1}{2}mv_{\parallel}^2 - e\phi_0(r) \geq |eV_{\text{E}}|, \tag{2.1}$$

where $\phi_0(r)$ is the equilibrium plasma potential found in Ref. [53]. This expression is simply an energy balance equation relating the condition for when a particle has sufficient kinetic and potential energy to pass over a potential hill of height $|eV_{\text{E}}|$. One small layer of complexity is now added. As particles begin to escape, the plasma potential changes because of the loss of charged particles. In fact, the plasma enters a series of complicated nonequilibrium states as more and more particles exit the trap. Generically, the magnitude of the plasma potential lowers, acting to shut off the extraction process by decreasing the potential energy of the particles. This acts to increase the effective potential barrier seen by the plasma particles (see Fig. 2.2). But the details of this changing plasma potential complicate the expression for $v_{\parallel\text{min}}$ as you must write the changing nonequilibrium plasma potential $\phi(r, \theta, z, t)$ rather then the simple and well known $\phi_0(r)$. However, if we assume that the fastest particles escape first, the escape condition is defined by the plasma potential at the end of the extraction process, which we write as,

$$\phi(r) = \phi_0(r) - \Delta\phi(r), \tag{2.2}$$

where $\triangle\phi$ is the change in the plasma potential from the beam. The justification for this is seen by observing that if the fastest particles escape first, the last particle to escape will be at $v_{\parallel\text{min}}$ by definition. This final escaping particle will then see the plasma potential at the end of the extraction process $\phi_0(r) - \Delta\phi(r)$. The

assumption that the fastest particles escape first is validated by the fact that the fastest particles cover the most axial distance in some fixed window of time. With this assumption, Eq. 2.2 is then the appropriate plasma potential to use to define the minimum escape velocity. Using this potential, the new escape condition becomes,

$$\frac{1}{2}mv_\parallel^2 - e[\phi_0(r) - \Delta\phi(r)] \geq |eV_{\rm E}|. \tag{2.3}$$

Note that $\triangle\phi(r)$ obeys the Poisson equation,

$$\nabla^2\left[\Delta\phi(r)\right] = 4\pi e\Delta n(r), \tag{2.4}$$

where $\Delta n(r)$ is the change in plasma density after beam extraction, and related to the z-integrated radial beam profile by $\sigma_{\rm b}(r) = L_{\rm p}\Delta n(r)$, from the assumption of z-independence. To calculate the beam profile, one simply integrates over all the particles in the plasma distribution function that satisfies the escape condition of Eq. 2.3,

$$
\begin{aligned}
\sigma_{\rm b}(r) &= 2L_{\rm p}\int_{v_{\parallel\min}(r)}^\infty f(r,v_\parallel)dv_\parallel \\
&= 2L_{\rm p}n_0(r)\,{\rm erfc}\left(\frac{v_{\parallel\min}(r)}{\sqrt{2}v_{\rm t}}\right),
\end{aligned}
\tag{2.5}
$$

where $f(r,v_\parallel)$ is assumed to be a Maxwellian velocity distribution at temperature, T;

$$v_{\parallel\min}(r) = \sqrt{-\frac{2e}{m_e}\left[V_{\rm E} - \phi_0(r) + \Delta\phi(r)\right]} \tag{2.6}$$

is the smallest velocity of escaping particles from Eq. 2.3; and ${\rm erfc}(x)$ is the complementary error function with argument, $x = v_{\parallel\min}/\sqrt{2}\,v_{\rm t}$.

A quick word on f. In equilibrium, the plasmas are uniform density, with a Maxwellian velocity distribution in the rotating frame of the plasma (i.e., in thermal equilibrium in the rotating frame). Each surface of constant radii is a surface of constant electric potential. As you move outwards in the plasma, the potential of the particles decreases. In this manner, the potential energy of the particles drops with increasing r, making $v_{\parallel\min}$ radially dependent.

Assuming an ideal "flat-top" density distribution (i.e., $n_0 = [N_0/\pi(R_{\rm p})^2 L_{\rm p}]$), the initial space charge in the plasma is [53]

$$\phi_0(r) = -\frac{eN_0}{L_{\rm p}}\left[1 - \frac{r^2}{R_{\rm p}^2} + 2\ln\left(\frac{R_{\rm W}}{R_{\rm p}}\right)\right].$$ (2.7)

Most beams studied here are moderate enough in size to be in the Gaussian beam limit, where the complementary error function in Eq. 2.5 is approximated as,

$$\mathrm{erfc}(x) \approx \frac{\exp(-x^2)}{\sqrt{\pi}\,x}.$$ (2.8)

This approximation if valid for values of $x > 2$. Now, using this approximation, evaluating Eq. 2.5 with Eqs. 2.6 and 2.7 yields,

$$\sigma_{\rm b}(r) \approx \sigma_{\rm b0}\exp\left[-\left(\frac{r}{2\lambda_{\rm D}}\right)^2\right]\exp\left[\frac{e\Delta\phi(r)}{T}\right],$$ (2.9)

where $\lambda_{\rm D}$ is the Debye length of the unperturbed plasma, and

$$\sigma_{\rm b0} \approx A\,\exp\left[\frac{e}{T}(V_{\rm E} - \phi_0(0))\right],$$ (2.10)

with A (approximately) a constant. For $|e\Delta\phi/T| \ll 1$, as is the case for a small beam, Eq. 2.9 becomes,

$$\sigma_{\rm b}(r) \approx \sigma_{\rm b0}\exp\left[-\left(\frac{r}{2\lambda_{\rm D}}\right)^2\right].$$ (2.11)

This is what will be defined as the small beam limit, where $\triangle\phi$ is neglected and the beam width $\rho_{\rm b}$ is equal to $\rho_{\rm b} = 2\lambda_{\rm D}$. As discussed above, $\sigma_{\rm b}(r)$ is the z-integrated radial distribution that would be measured when the extracted beam impinges on a collector plate. At this point, A in Eq. 2.10 is not defined, making Eqs. 2.9 and 2.11 only proportional to the beam radial profile. While this will presently appear as a limitation of the theory, an expression for the total number of beam particles, or $\sigma_{\rm b0}$, will be derived in Ch. 3.

For larger beams where the Gaussian beam approximation (c.f., Eq. 2.8) made in Eq. 2.9 is still valid but the small beam approximation made in Eq. 2.11 is

not, $\triangle\phi$ is no longer negligible and must be addressed. To deal with this term, the change in potential from a Gaussian beam of width ρ_b is calculated analytically and written as,

$$
\begin{aligned}
\triangle\phi(r) &= \frac{T\xi}{e}\left[2\ln\frac{r}{R_W} + \Gamma\left(0,\frac{r^2}{\rho_b^2}\right) - \Gamma\left(0,\frac{R_W^2}{\rho_b^2}\right)\right] \\
&\approx \triangle\phi(0) + \xi\frac{T}{e}\frac{r^2}{\rho_b^2},
\end{aligned} \tag{2.12}
$$

where the parameter ξ is,

$$
\xi = \frac{e^2 N_b}{TL_p}. \tag{2.13}
$$

Equation 2.12 has been tailored expanded to 2nd order about $r = 0$, and ρ_b is the half width to $1/e$, or the radial spread of the Gaussian. The 2nd order Taylor expansion is reasonably good over the region in the plasma where the beam is extracted, or $|r/\rho_b| \leq 1$. As will be seen later, the approximation in Eq. 2.12 still works as an effective approximation for $\triangle\phi(r)$ when beams become non-Gaussian or Eq. 2.8 is no longer valid. One reason for this, as will be seen, is non-Gaussian beams here typically resemble uniform density flat-top beams. For these flat-top beams, $\triangle\phi(r)$ is exactly equivalent to a quadratic, or the approximation written in Eq. 2.12.

In Eq. 2.9, although the magnitude of $e\triangle\phi/T$ will alter the total amount of extracted charge, it is only the variation in $e\triangle\phi/T$ *across the beam profile* that is important in changing the transverse beam shape. In this sense, the key parameter in Eq. 2.12 is the dimensionless parameter ξ. This parameter is equal to the change in $\triangle\phi$ across the beam (in terms of T) or $\xi = \triangle\phi(\rho_b) - \triangle\phi(0)$. Note that ξ is simply the beam amplitude N_b scaled to the plasma parameters. This parameter is key because when inserting Eq. 2.12 into Eq. 2.9, the areal density becomes,

$$
\sigma_b(r) \approx \sigma_{b0}\exp\left[-\left(\frac{r}{2\lambda_D}\right)^2 + \xi\left(\frac{r}{\rho_b}\right)^2\right], \tag{2.14}
$$

where σ_{b0} contains the radius-independent term arising from $\triangle\phi(0)$. Since ρ_b is defined as the half-width to $1/e$ (i.e., $\sigma_b(r = \rho_b) = \sigma_{b0}e^{-1}$) the beam width is,

$$\rho_{\mathrm{b}} \approx 2\lambda_{\mathrm{D}}(1 + \xi)^{1/2}. \tag{2.15}$$

Equations 2.14 and 2.15 predict a Gaussian beam just as with Eq. 2.11, but now ρ_{b} is $\geq 2\lambda_{\mathrm{D}}$ and determined by ξ. The small-beam condition required for the validity of Eq. 2.11 can now be expressed as simply $\xi \ll 1$. Since Eq. 2.13 can also be written as $\xi = (N_{\mathrm{b}}/N_0)(R_{\mathrm{p}}/2\lambda_{\mathrm{D}})^2$, this condition places an important practical constraint on the number of plasma particles that can be extracted in a small-beam, namely $N_{\mathrm{b}}/N_0 \ll (2\lambda_{\mathrm{D}}/R_{\mathrm{p}})^2$.

Equations 2.14 and 2.15 describe well a range of beam profiles observed in experiment. However, when $\xi > 1$ non-Gaussian beam profiles are observed. In this case, numerical solutions of Eq. 2.4 and Eq. 2.5 can be used to predict the measured profiles, even when $N_{\mathrm{b}} \approx N_0$. As will also be seen, Eq. 2.15 remarkably remains valid for all beam sizes.

2.3 Description of the experiment

The Penning-Malmberg trap used for these experiments is shown schematically in Fig. 1.2. It consists of a series of hollow conducting cylindrical electrodes 0.5 m in total length with radii $R_W = 1.27$ cm. A uniform magnetic field of $B = 4.8$ T lies parallel to the z-axis of cylindrical symmetry of the electrodes. For a more complete description of the apparatus, see Ch. 1.

Plasmas are created using a standard electron gun to fill a potential well of variable depth ($V_{\mathrm{fill}} \sim + 50$ V). The magnetic field provides radial confinement while axial confinement is achieved by the application of confinement voltages $V_{\mathrm{C}} = -100$ V to electrodes on both end of the trap. The plasma length L_p is roughly the distance between the confining electrodes.

In equilibrium, the plasma has a constant density n_0 (i.e., a flat top radial distribution) and undergoes E x B rotation at a frequency set by n_0 [13, 12]. The plasma temperature T is set by the balance between heating sources (e.g., background drag and rotating wall heating) and cyclotron cooling ($\tau_{\mathrm{c}} = 0.16$ s).

Unless otherwise noted, for the plasmas described here: $N_0 \approx 4 \times 10^8$

electrons; $n_0 \approx 1 \times 10^9$ cm^{-3}; $R_\mathrm{p} \approx 0.1$ cm; $L_\mathrm{p} \approx 15$ cm; and $T \approx 0.05$ eV. For these plasmas, the Coulomb collision time ($\tau_{ee} < 1$ ms) is rapid compared to τ_c, thus ensuring that the plasmas are constantly in states of thermal equilibrium, even while cooling [12]. Plasmas here exhibit excellent shot-to-shot reproducibility, with $\Delta N_0 / N_0 \leq 1\%$.

Density and total charge are measured using an aluminum-coated phosphor screen located adjacent to one of the ends of the trap (see Fig. 1.2). The confining potential V_C on electrodes at one end of the trap is lowered and exiting electrons are accelerated into an aluminum screen which is biased to a positive electric potential. For low screen potentials (e.g., 25 V), the total charge is measured, giving the number of electrons exiting the trap. When V_C is lowered to 0 V, this number is equivalent to N_0; when lowered to V_E, this number is equivalent to N_b. At much higher potentials (e.g., 5 kV), the exiting electrons penetrate the aluminum coating and produce light in the phosphor that is imaged using a CCD camera. When V_C is lowered to 0 V, this image is the two-dimensional (i.e., areal) z-integrated density distribution $\sigma_\mathrm{z}(r, \theta)$ of the trapped plasma, where $n(r, \theta) \approx \sigma_\mathrm{z}(r, \theta) / L_\mathrm{p}$, and is independent of z. For a typical situation described here with rotational symmetry, $\sigma_\mathrm{z}(r, \theta)$ is written as $\sigma_\mathrm{z}(r)$ with the θ dependence suppressed. Plots such as Fig. 2.3 include values $r < 0$ to represent measurements taken along a major chord through the circular distribution. When V_C is lowered to V_E, the image is then equivalent to the radial beam profile $\sigma_\mathrm{b}(r)$.

The plasma temperature is varied using the technique described in Ref. [5]. It consists of repeatedly compressing and expanding the plasma by changing L_p, thereby heating the plasma through Coulomb collisions. The temperature is determined by a time-resolved measurement of the number of electrons escaping from the trap while V_C at one end is *slowly* lowered [18].

The plasma density is varied using the RW technique [13, 12]. As discussed in Sec. 1.4, phased sine waves applied to a sectored electrode are used to generate a rotating electric field with azimuthal mode number $m_\theta = 1$. These fields produce a torque on the plasma, thus providing a way to compress or expand the plasma in a non-destructive manner. See Ref. [13] for details.

2.4 Single beam extraction

As discussed above, to extract a beam from a trapped plasma, V_{C} is raised at one end of the trap from -100 V $\rightarrow V_{\mathrm{E}} \approx \phi_0(0)$ for a brief extraction time $\triangle t \approx 10$ μs. Using this technique, small beams ($\xi < 0.1$) were extracted over a factor of approximately 40 in both density ($0.06 < n_0 < 2.2 \times 10^{10}$ cm^{-3}) and temperature ($0.05 < T < 2$ eV). Figure 2.4 shows examples of $\sigma_{\mathrm{b}}(r)$ and the corresponding Gaussian fits over a wide range of T and n_0, respectively. However, due to extra heating during RW compression, not all temperatures were achieved at all densities. The observed beam distributions are seen to be in excellent agreement with the Gaussian form of Eq. 2.11.

From the Gaussian fits, the beam width ρ_{b} is found for each extracted beam. Data for ρ_{b} over a factor of 30 in λ_{D} are shown in Fig. 2.5, and compared with the predictions of Eq. 2.11. As shown in Fig. 2.5, the average of all the data $< \rho_{\mathrm{b}} > / \lambda_{\mathrm{D}} = 2.2 \pm 0.2$ is in good agreement with the predicted value of 2.0 in Eq. 2.11. The small discrepancy between data and the predictions of Eq. 2.11 is currently unexplained.

The data in Fig. 2.4 show that at constant T, the width of an extracted small beam is determined by λ_{D} and hence by the plasma density n_0. By varying n_0 in a non-destructive manner *without particle loss* using the RW, the extracted beam can be transversely focused. This focusing procedure is illustrated in Fig. 2.6, where n_0 is increased so as to narrow the resulting extracted beam. Here, since $\lambda_{\mathrm{D}} \propto 1/\sqrt{n_0}$, as the density is increased by a factor of 30, the measured beam width drops by a factor of 6. Note that in addition to decreasing the width, the beam brightness is increased dramatically by a factor of 25. Further, the energy spread remains constant as the plasma temperature changes only marginally which, as will be shown in Ch. 3, approximately sets the beam energy spread. Thus, this RW focusing technique allows one to decrease the beam width, increase the beam brightness, and keep the energy spread constant all in a nondestructive way. This technique is therefore superior to any aperture or electrostatic focusing technique which would decrease the beam width at the cost of either losing particles while holding brightness constant, or increasing the beam energy spread [32].
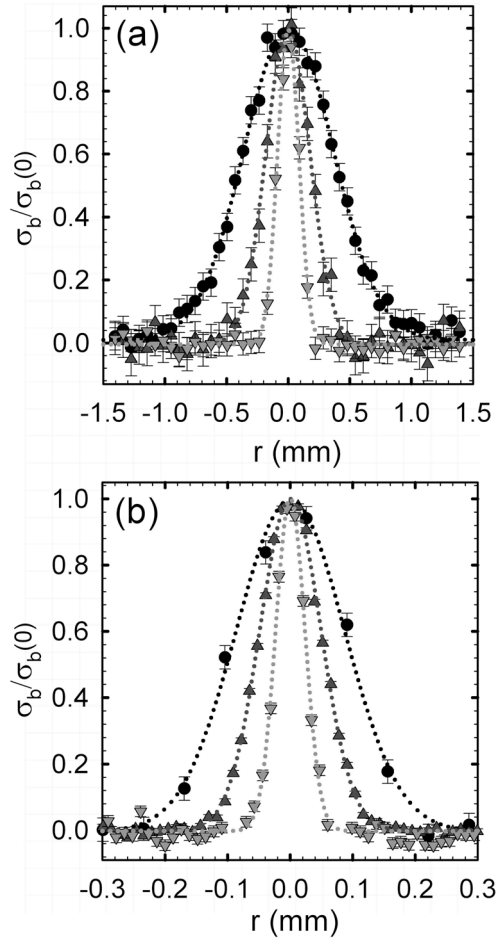
Figure 2.4: Small beam profiles $\sigma_{\mathrm{b}}(r)$: (a) $n_0 \approx 1 \times 10^9$ cm^{-3}, and $T \approx 1$ eV ($\bullet$), 0.2 eV ($\blacktriangle$), 0.04 eV ($\blacktriangledown$). (b) $T \approx 0.1$ eV, and $n_0 \approx 1 \times 10^9$ cm^{-3} ($\bullet$); 6.5×10^9 cm^{-3} ($\blacktriangle$); 1.2×10^{10} cm^{-3}, ($\blacktriangledown$). Gaussian fits ($\cdots$) are also shown. $\xi < 0.1$ for all beams.
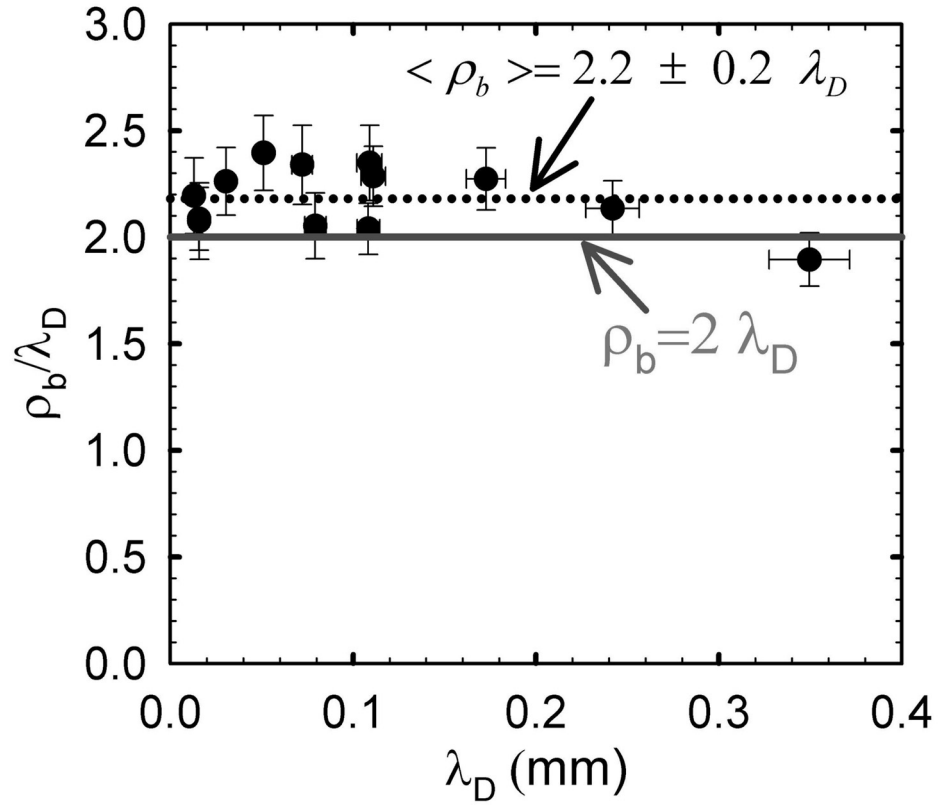
Figure 2.5: Log-log plot of ρ_b vs. λ_D along with the prediction $\rho_b = 2\lambda_D$ from Eq. 2.11 (—). The average $\langle \rho_b/\lambda_D \rangle = 2.2 \pm 0.2$ for all data $(\cdots)$ is also included. For all beams, $\xi < 0.1$.
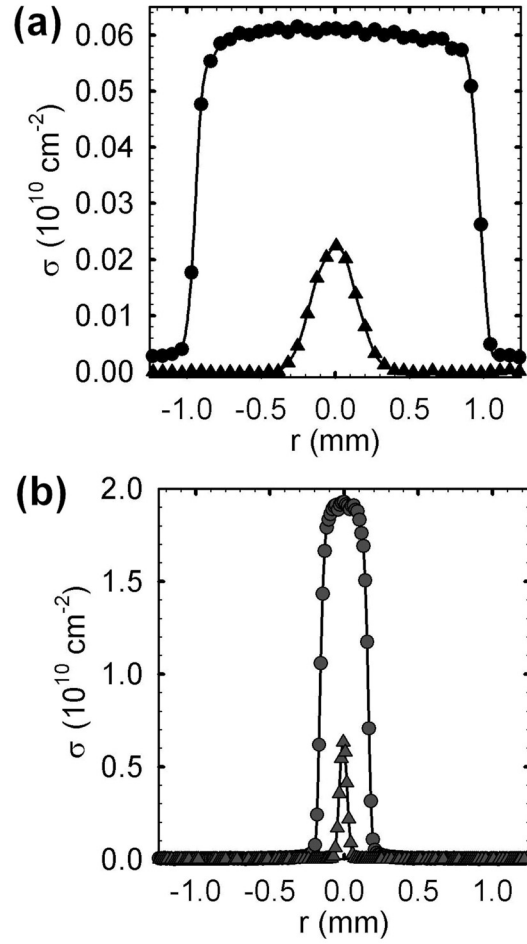
Figure 2.6: Radial distributions $\sigma_{\mathrm{b}}(r)$ (▲) for beams extracted from a plasma (a) before ($n_0 = 0.65 \times 10^{10}$ cm^{-3}), and (b) after RW compression ($n_0 = 2.2 \times 10^{10}$ cm^{-3}). The initial plasma profiles $\sigma_{\mathrm{z}}(r)$ (●) are also shown. Here $L_{\mathrm{p}} \approx 22$ cm, and $T \approx 0.1$ eV.

As mentioned above, Eq. 2.11 is valid only for $\xi \ll 1$. If ξ exceeds this limit, the extracted beams may exhibit radial distributions that are described more accurately by Eq. 2.14, which describes a Gaussian beam with a width that is dependent on ξ. But in what regime are Eqs. 2.14 and 2.15 accurate? Experimentally, as N_b is increased to intermediate values $0.1 < \xi < 1$, the beams remain Gaussian and well described by Eqs. 2.14 and 2.15. As N_b increases further to $\xi > 1$, the profiles become non-Gaussian and ultimately evolve to "flat-tops", with steep edges and flat maximum that are no longer well described by Eq. 2.14. Remarkably, as will be shown later, Eq. 2.15 remains valid for extracted beams of any ξ.

The validity of Eq. 2.14 is illustrated in Fig. 2.7, where beam profiles are plotted over the entire range of N_b from two plasmas with the same density ($n_0 \approx 1 \times 10^9$ cm^{-3}) but different temperatures, along with the theoretical predictions of Eq. 2.14. For the three smallest beams ($\xi < 1$), the predictions of Eq. 2.14 are plotted as dotted lines, showing excellent agreement with the measured profiles. For the three larger beams ($\xi > 1$), the profiles become non-Gaussian and are no longer described by Eq. 2.14. There, predictions are obtained by numerically solving Eqs. 2.4 and 2.5 using the measured values for $n_0(r)$, T, L_p and N_b. These predictions, shown as solid lines in Fig. 2.7, are in reasonable agreement with the measurements, demonstrating that the profile of an arbitrary sized beam (i.e., all beams such that $0 < N_b \leq N_0$) can be predicted numerically.

From the data shown in Fig. 2.7, ρ_b can be obtained over a broad range in N_b. Figure 2.8 shows the results of these measurements together with the predictions of Eq. 2.15 and numerical solutions to Eqs. 2.4 and 2.5. The measured values of ρ_b are in good agreement with the predictions of Eq. 2.15 with no fitted parameters. Remarkably, agreement is seen over the full range of N_b. As mentioned above, this is not expected for $\xi > 1$ because there the beam profiles depart from the Gaussian shapes predicted by Eq. 2.14. Thus, the agreement with Eq. 2.15 shown in Fig. 2.8 is fortuitous. The details of why this expression works are unimportant, but it functions as a convenient expression that makes a good approximation of the beam width over the entire range of possible beams ($N_b = 0 \rightarrow N_0$). The beam width predicted by the numerical solutions is in similar
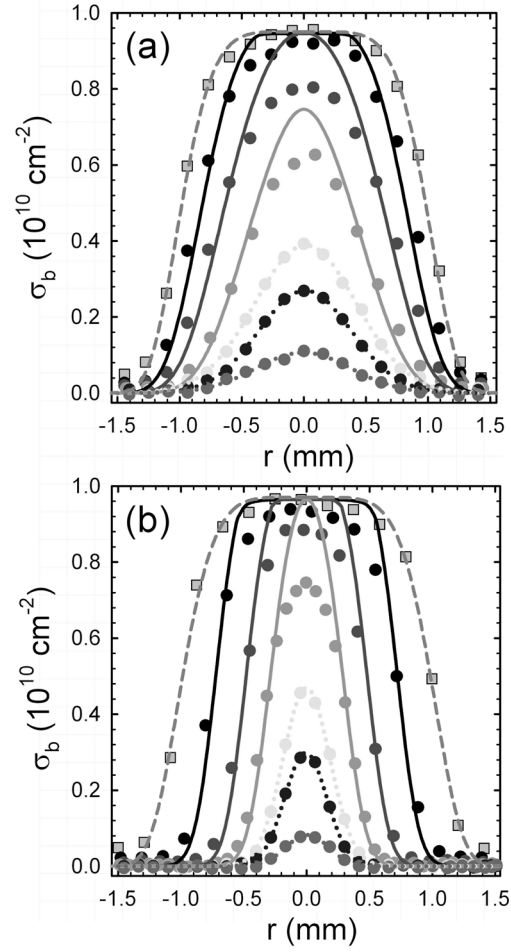
Figure 2.7: Profiles $\sigma_b(r)$ of extracted beams: (a) $T \approx 1.0$ eV, $\xi \approx 0.1$, 0.3, 0.5, 1.0, 1.9, 2.8; and (b) $T \approx 0.2$ eV, $\xi \approx 0.1$, 0.3, 0.5, 2.2, 5.2, 11. In both (a) and (b), the three smallest beams are fit ($\cdots$) to Eq. 2.14, and the three largest beams are fit (—) to numerical solutions to Eqs. 2.4 and 2.5. The initial plasma profile $\sigma_z(r)$ is shown ($\square$), as is the fit (- - -) used in the numerical solutions.

good agreement with the data. This is expected as none of the assumptions made in Sec. 2.2 were used in the calculations.

The extraction of multiple beams from the same plasma is an important practical goal (see Sec. 2.5). If Penning-Malmberg traps are to be used for positron applications, it will be critical to efficiently use all of the trapped particles because of the long times required to gather them initially. Extracting multiple beams is most easily accomplished if the plasma returns to equilibrium after each extraction. If this is the case, it is much easier to achieve reproducibility and to tailor beam pulses using the theory and tools found in this thesis. To investigate this issue, the plasma response following a single-beam extraction was investigated by recording the areal plasma density $\sigma_z(r)$ at discrete time intervals after the extraction of a beam. Four such distributions are shown in Fig. 2.9.

Shortly after the extraction and at $t = 100$ μsec, the profile is the initial "flat-top" profile with a "hole" in the center where the extracted beam particles were removed. By 250 μsec, the hole has moved away from the plasma center, breaking the typical θ symmetry found in $\sigma_z(r, \theta)$. From the time evolution of $\sigma_z(r, \theta)$ (not shown), the density hole is seen to rotate around the center axis of the plasma, as well as drift radially outward. Similar dynamics are discussed in Ref. [16], in which a similar density hole was created in an electron plasma and displaced slightly off-axis to produce an unstable diocotron mode. In both situations, the density hole is convected around the plasma center with a radial location that grows exponentially with time. Here there is no initial off-axis displacement of the density hole, and so the radial displacement does not reach significant amplitudes until times > 100 μsec. However by only 500 μsec, the plasma has fully recovered to equilibrium (the plasma has fully thermalized, as $\tau_{ee} \approx 20$ μsec) via growth of the unstable diocotron mode..

Beneficially, this instability does not interfere with the beam extraction process, which occurs in less than 10 μs. Further, for beams with $\xi < 1$, the instability decreases the plasma recovery time, thereby aiding in the extraction of multiple beams. Without the instability, the plasma would be forced to return to equilibrium via collisional transport in which particles take steps on the order
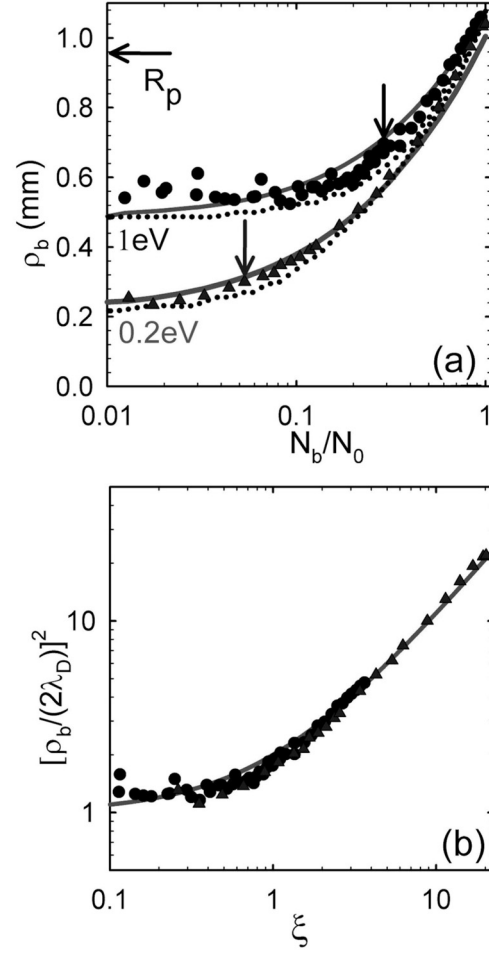
Figure 2.8: (a) Beam width parameter ρ_b plotted vs. N_b/N_0 for $T \approx 1.0$ eV ($\bullet$), and 0.2 eV ($\blacktriangle$). Predictions (—) from Eq. 2.15 with no fitted parameters, and ($\cdots$) numerical solutions to Eqs. 2.4 and 2.5. Arrows correspond to beams with $\xi = 1$. (b) Data from (a) plotted as $(\rho_b/2\lambda_D)^2$ vs. ξ, showing all data lies on a single curve (—) given by Eq. 2.15.
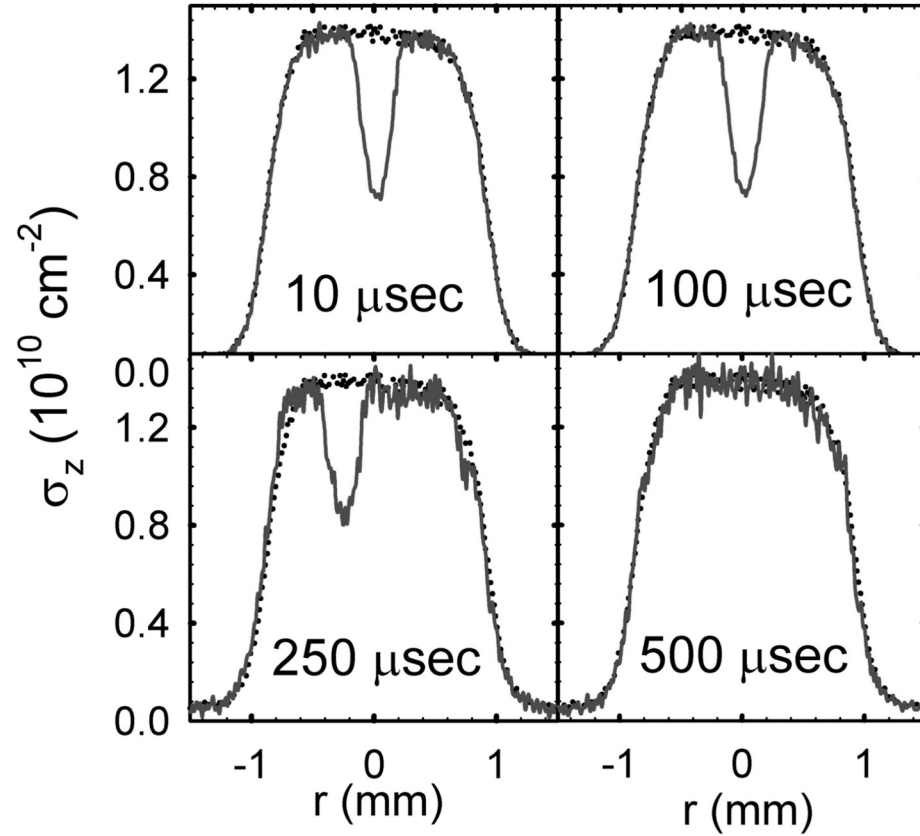
Figure 2.9: Profiles $\sigma_z(r)$ are shown at four times after the extraction of a beam. For the data at 250 μs, the major chord along which $\sigma_z(r)$ is measured is chosen to pass through the center of the off-axis hole. Also shown $(\cdots)$ is $\sigma_z(r)$ before the extraction.

$\Delta r \sim r_c \approx 0.1 \ \mu$m, where r_c is the electron gyro radius. This process would undoubtedly take significantly longer then 500 μs, as no noticeable radial transport is observed in this time in Fig. 2.9. However, for larger beams (i.e., $\xi > 1$), other types of plasma instabilities occur (in times $> 100 \ \mu$s) that increase the plasma re-equilibration time and, in some cases, prevent the plasma from returning to a "flat-top" equilibrium state.

These results indicate that, for appropriate sized beams, extraction times as long as 100 μsec are possible without violating the assumptions of Sec. 2.2. This is verified in Fig. 2.10 where N_b is plotted for beams extracted on two times scales: the typical 10 μs extraction, and a longer extraction over $\approx 200 \ \mu$s. The long time scale extraction is performed by a linear ramp of V_C from $-100 \rightarrow 0$ V at a rate of 0.015V/μs. In this "slow" extraction, unlike the normal beam extraction, both V_C (equivalent to V_E) and N_b are measured continuously as a function of time. As seen in Fig. 2.10, the two methods extract identical size beams when $V_C = V_E$. This, in turn, provides evidence that no significant radial transport or collisions occur during the longer extraction time. The smooth increase in N_b over the first 100 μsec of the slow ramp (indicated by the arrow in Fig. 2.10), further illustrates the stability of the plasma on these time scales. As also shown in Fig. 2.10, for small N_b, the slow extraction data can be fit to an exponential (i.e., Eq. 2.10). This is used to measure plasma temperatures in the present work [5, 18].

2.5 Extraction of multiple beams

As mentioned previously, for practical applications it is desirable to make efficient use of the plasma particles by extracting multiple beams before refilling the trap. One way to do this is to extract a beam at some extraction voltage V_E; wait for the plasma to reach a new equilibrium; then extract another beam at $V_E + \Delta V_E$, chosen to tailor the subsequent beam. Here, ΔV_E is determined empirically to maintain constant N_b however Ch. 3 will present a formula to analytically determine the necessary ΔV_E for any size beam desired.

After a beam is extracted, particles from the plasma are depleted and the
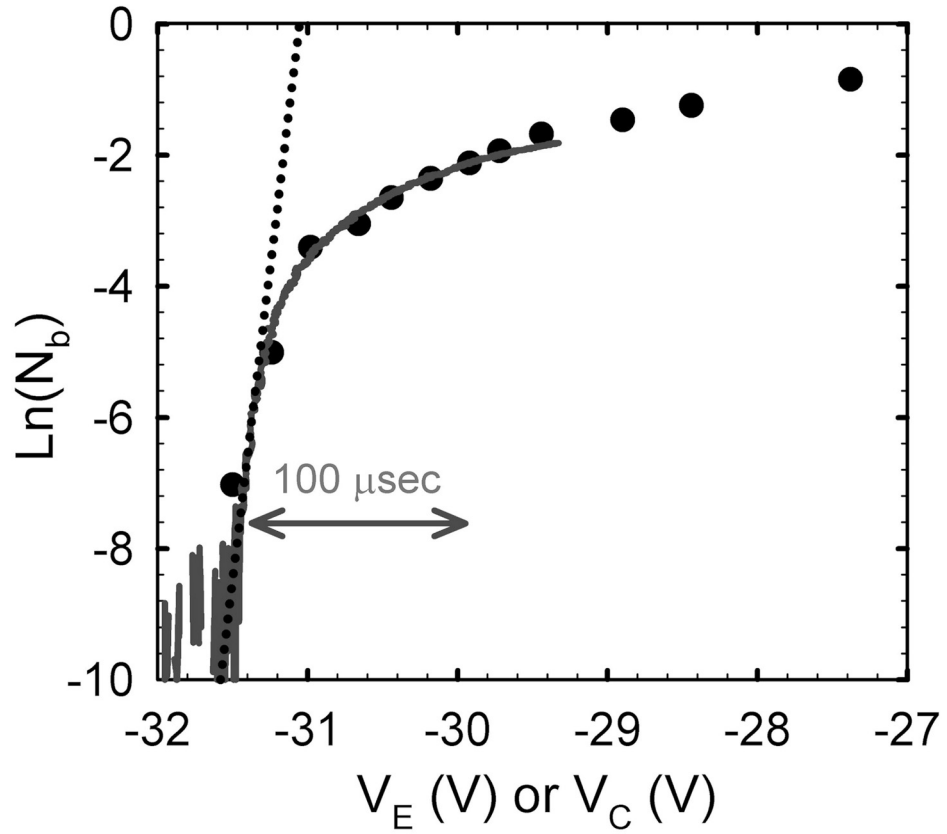
Figure 2.10: Fast and slow beam extraction procedures are compared: $\ln(N_b)$ ($\bullet$) for fast (≈ 10 μs) extractions at different values of V_E; and $\ln(N_b)$ (—) vs. V_C, as measured continuously while V_C is ramped slowly from -100 V $\rightarrow$ 0 V at a rate of 0.015 V/μs. Also shown ($\cdots$) is the prediction in Eqs. 2.10 and 2.11 with $T = 0.05$ eV.

plasma density drops resulting in an increased Debye length. Thus each subsequent beam will have a progressively larger width. This is illustrated in Fig. 2.11, where 50 % of a trapped plasma is extracted in the form of 20 beams. Notice the plasma density drops, while the beam width expands.

To counter this effect, we utilize the RW technique (described in Sec. 1.4) to maintain the plasma at a constant density. For multiple beams extracted in this manner, it was empirically determined that in order to maintain a constant amplitude pulses, ΔV_E must remain fixed throughout the extraction process.

Shown in Figs. 2.12 - 2.14 is an example in which over 50 % of the plasma was removed by extracting a sequence of 20 beams while maintaining fixed n_0 by RW compression. In this case, n_0 is held constant while R_p is allowed to vary with each extraction.

The total collected charge for each extracted beam is shown in Fig. 2.12. The time interval between beam extractions was set to 200 ms in order to allow for full RW compression after each extraction. Here, this process yielded 20 constant-amplitude beams (i.e., $\Delta N_b/N_b < 0.05$) with $N_b \approx 1 \times 10^7$ per pulse.

In Fig. 2.13, the z-integrated plasma density is shown before and after extraction of the 20 beams at fixed density $n_0 \approx 2 \times 10^9$ cm^{-3} and temperature $T \approx 0.3$ eV (the density and temperature change by less than 10% over the total extraction). Here, the RW plasma compression is done at a constant frequency $f_{RW} = 1.05$ MHz and amplitude $V_{RW} = 1.2$ V. For this case, both n_0 and T (and hence λ_D) are approximately constant during the multiple-beam extraction process, while the total number of particles in the plasma drops from $N_0 \approx 4.6 \rightarrow 2.4 \times 10^8$, corresponding to ejecting $\approx 50\%$ of the plasma.

Because the Debye length is the same for each beam, we expect the beam widths to also be the same. This is verified in Fig. 2.14 where the profiles for the 1st, 10th, and 20th extracted beams from Fig. 2.12 are shown. Here, the measured beam width $\rho_b \approx 0.2$ mm remains approximately constant for all beams. Using the measured values for n_0, T, L_p, and N, we find $\lambda_D \approx 0.09$ mm and $\xi \approx 0.2$. Plugging these values into Eq. 2.15, we would expect a beam-width $\rho_b \approx 0.18$ mm, in excellent agreement with the data in Fig. 2.14.
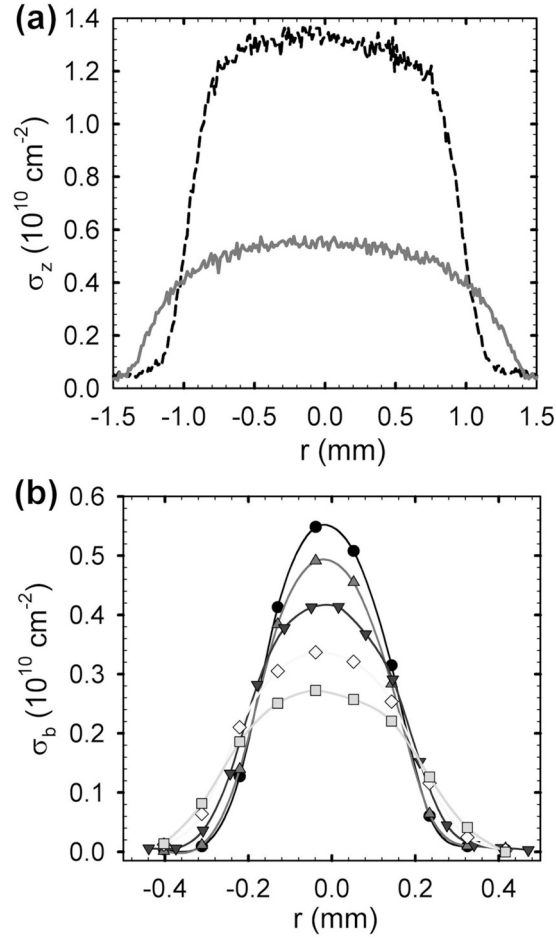
Figure 2.11: (a) Plasma profiles $\sigma_z(r)$ before (- - -) and after (—) the extraction of 20 beams of $N_b \approx 0.07 \times 10^8$. The plasma temperature remains constant, while the density drops a factor of 2 ($T \approx 0.05$ eV, $n_0 \approx 9 \rightarrow 4 \times 10^9$ cm^{-3}). Here $L_p \approx$ 21 cm. (b) The lst, 5th, 10th, 15th and 20th beam profiles are plotted. Note the decreasing plasma density causes the widths to progressively increase.
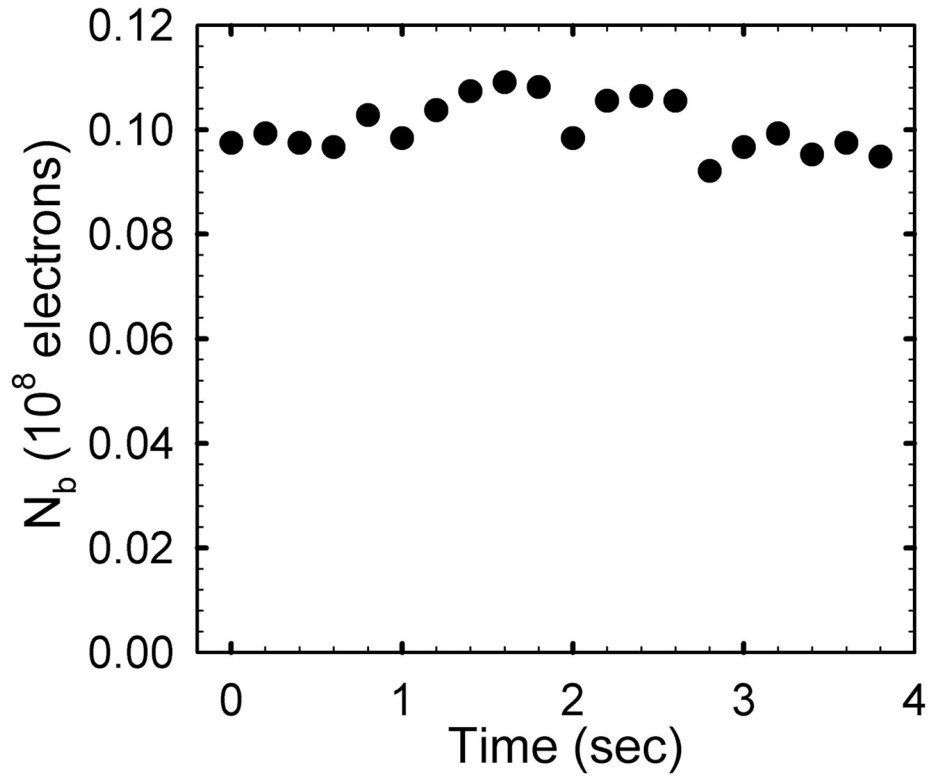
Figure 2.12: N_b for twenty electron beams extracted consecutively with $< N_b > = (0.1 \pm 0.005) \times 10^8$, $\xi \approx 0.2$ and the RW on.
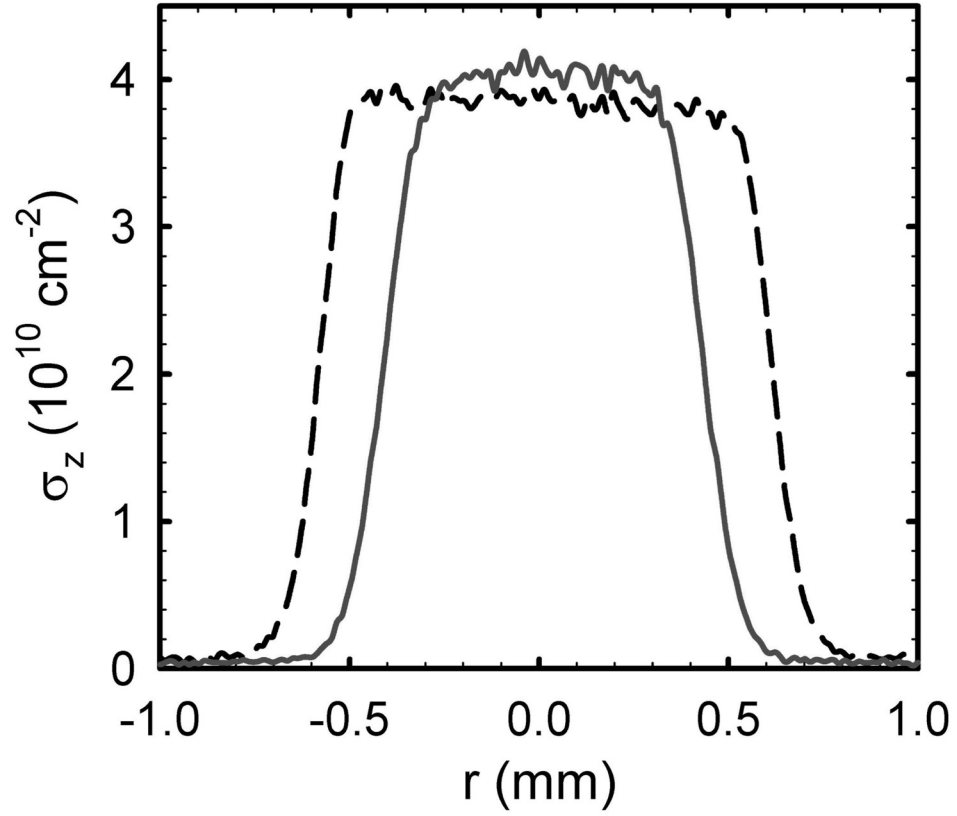
Figure 2.13: Plasma profiles $\sigma_z(r)$ before (- - -) and after (—) the extraction of 20 beams of $N_b \approx 0.1 \times 10^8$. RW compression holds the plasma parameters ($T \approx 0.3$ eV, $n_0 \approx 2 \times 10^9$ cm^{-3}) approximately constant, while the total number drops from $N_0 \approx 4.6 \rightarrow 2.4 \times 10^8$. Here $L_p \approx 21$cm.
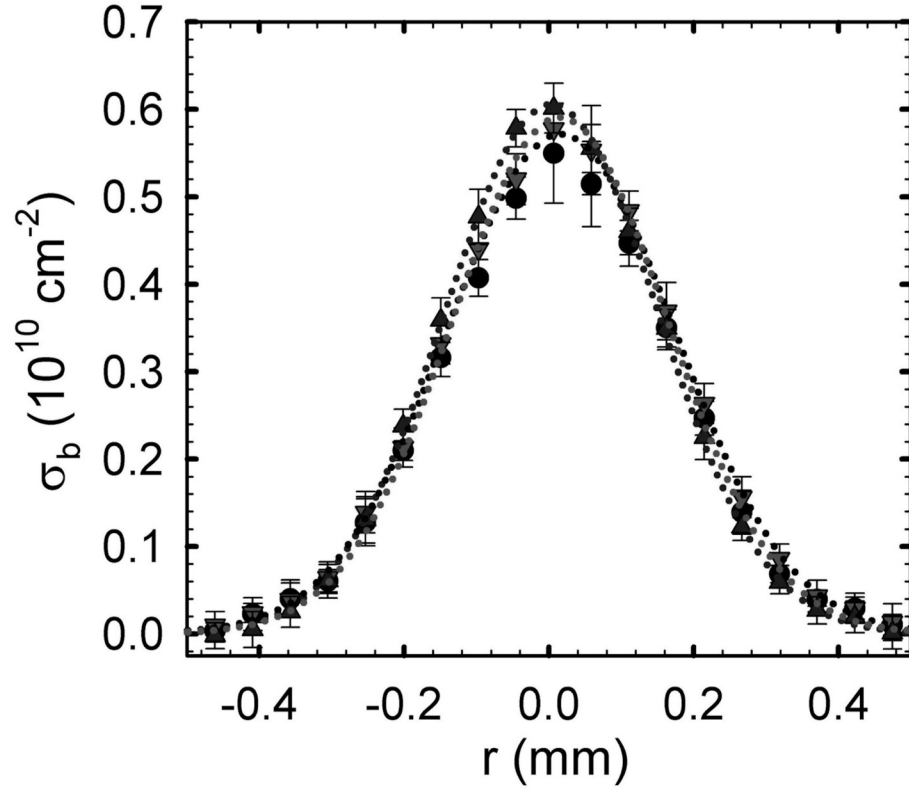
Figure 2.14: Profiles $\sigma_\mathrm{b}(r)$ for the 1st ($\bullet$), 10th ($\blacktriangle$), and 20th ($\blacktriangledown$) extracted beams in Fig. 2.12. $N_\mathrm{b} \approx 0.1 \times 10^8$ for all beams. The beam width ($\rho_\mathrm{b} \approx 0.2$ mm) remains approximately constant because here λ_D is invariant during entire extraction process. Gaussian fits ($\cdots$) are also shown.

It should be noted that a previous experiment with positrons in a Penning-Malmberg trap demonstrated the extraction of multiple beams from a single trapped plasma [23, 39]. However, the positron density was low enough (i.e., $\lambda_{\mathrm{D}}/R_{\mathrm{p}} > 1$) that no plasma effects were observed. Further, the time between pulses was much shorter than the re-equilibration time, and thus the plasma distribution was likely non-Maxwellian for all but the first couple of beams. One effect of this was that a non-constant ΔV_{E} was necessary in order to produce equal-strength beams [39]. In contrast, the experiments shown here (cf., Figs. 2.12-2.14) demonstrate how a suitable plasma (i.e., $\lambda_{\mathrm{D}}/R_{\mathrm{p}} \ll 1$) can be used to extract more than half the plasma into a series of *identical*, high quality beams using a constant ΔV_{E}.

2.6 Summary

We have demonstrated the ability to extract high quality charged particle beams from a Penning-Malmberg trap. Beams were tailored to low spatial spreads (e.g., $\rho_{\mathrm{b}} < 50~\mu\mathrm{m}$) and high brightness using RW compression and cyclotron cooling. A theory is developed based on a simple model that predicts accurately the beam spatial profile and width. The extraction of multiple beams has been demonstrated, showing an exciting possibility for a Penning-Malmberg trap to function as a effective source of positrons. Finally, multiple beams were extracted in a reproducible ($\Delta Nb/N_{\mathrm{b}} < 5~\%$) and efficient ($\approx 100~\%$) manner.

Chapter 3

Beam Energy Distribution Functions [1]

In Ch. 2, a novel technique to extract small beams from a single component plasma in a Penning-Malmberg (PM) trap was presented. Using a simple mode, many properties of the beam were derived including the radial profile, width, and relative brightness. These predictions were all verified using electron plasmas in the high field trap presented in Sec. 1.4. The results demonstrate the potential to use a PM trap to create positron beams of small width and large brightness in a reproducible and nondestructive manner. However, presently there has been no discussion of the beam energy spread which is important for many applications. For energy resolved atomic physics, beam bunching, microscopy, antihydrogen formation, and Bose-Einstein condensed positronium, a low energy spread positron beam is desired [29, 51, 58, 43, 56, 55, 20, 62, 24, 1, 9, 21, 2]. Therefore, to verify the utility of these beams for positron applications we will now determine the energy distribution functions of the beam. Because of the large electric potential gradients across the plasma ($\Delta V \approx 50V$), one might expect the beam spread to be much larger than that of the parent plasma temperature T. This section will show that this is not the case, while illustrating more physics behind the extraction process.

---

[1]This Chapter is based upon the paper, T. R. Weber, J. R. Danielson and C. M. Surko, Phys. Plasmas, 057105 (2009). Mr. Weber was the lead scientist on this work.

3.1   Theoretical description

In this section, an expression is developed for the energy distribution function of the beam as a function of the plasma parameters and extraction voltage V_E only. As mentioned in Ch. 2, it is assumed that the exit gate is lowered for a time which is sufficiently long so that all the particles with enough energy to escape do so. It is also assumed that the plasma particles with largest velocity parallel to the magnetic field $v_\parallel$ escape first. While not strictly valid, this assumption makes the calculations below tractable and is qualitatively correct in that the particles with large $v_\parallel$ traverse the plasma length faster, thus making them more likely to escape first. The finite slewing time of the exit-gate electrode also favors this order.

In this section, rather then working with velocities inside the plasma (i.e., $v_\parallel$ and $v_\perp$) we will work with kinetic energies in motion parallel and perpendicular to the magnetic field outside the plasma, denoted $E_\parallel$ and $E_\perp$ respectively. Inside the plasma, $E_\parallel$ is defined as,

$$E_\parallel = \phi(r) + 0.5mv_\parallel^2, \tag{3.1}$$

or the sum of the potential and kinetic energy in motion parallel to the magnetic field inside the plasma. Once a particle escapes confinement, it is in a zero potential region outside the plasma. Then, $E_\parallel$ is simply,

$$E_\parallel = 0.5mv_\parallel^2, \tag{3.2}$$

where $v_\parallel$ simply represents the particle's velocity parallel to the magnetic field in the zero potential region outside the trap. Note that $E_\parallel$ is conserved between Eqs. 3.1 and 3.2. The main point is that as the particle moves from a region of large electric potential [i.e., $|e\phi_0(0)|$] to a region of low potential (0 V outside the plasma), $v_\parallel$ will increase and solely defines $E_\parallel$. $E_\perp$ is defined as,

$$E_\perp = 0.5mv_\perp^2. \tag{3.3}$$

or the kinetic energy in motion perpendicular to the magnetic field. For beams extracted here, $E_\perp$ remains constant as the particle exits the trap.

The condition that a particle escapes now is simply,

$$E_\parallel > |eV_{\mathrm{E}}|. \tag{3.4}$$

The particles that escape confinement constitute the beam. What we would like to know is the energy distribution function of the beam, or the number beam particles at a given $E_\parallel$ and $E_\perp$ outside the trap.

With this in mind, using the new variables $E_\parallel$ and $E_\perp$, the single particle distribution function for a uniform density "flat-top" plasma in thermal equilibrium is approximately,

$$f_{\mathrm{P}}(E_\parallel, E_\perp, r, \theta, z) \approx \frac{n_0}{\sqrt{\pi} T^{\frac{3}{2}}} \frac{\exp\left(-\frac{E_\perp + E_\parallel + e\phi(r)}{T}\right)}{\sqrt{E_\parallel + e\phi(r)}}, \tag{3.5}$$

where the uniform $E \times B$ rotation has been neglected, an assumption valid when the thermal velocity is greater than the rotation velocity of the particles near the extraction region. This condition is written as $\rho_{\mathrm{b}} f_{\mathrm{E}}/v_{\mathrm{t}} \ll 1$, where f_{E} is the rotation frequency of the plasma. This requirement is well satisfied for all plasmas in the Brillouin limit, the maximum theoretical density for a plasma in PM trap. For plasmas in this work, $\rho_{\mathrm{b}} f_{\mathrm{E}}/v_{\mathrm{t}} < 5 \times 10^{-4}$. Note that Eq. 3.5 is just a convoluted way of writing a Maxwellian in the new variables defined in Eqs. 3.1 and 3.3. In Ch. 2, we found the escaping particles by using a simple particle distribution with a complicated escape condition. Now, we have done the opposite.

As discussed in Sec. 2.2, to determine the beam particles that escape, one uses $\phi(r)$ at the end of the extraction process. There, $\phi(r)$ contains an equilibrium piece $\phi_0(r)$, and a nonequilibrium piece $\triangle\phi(r)$ that depends on the number of escaping particles. Just as in Sec. 2.2, for sufficiently small beams $\triangle\phi(r)$ may be neglected so that $\phi(r) \approx \phi_0(r)$, independent of the number of escaping particles N_{b}. The potential $\phi_0(r)$ is known analytically, and quadratic in r for $r < R_P$ [53]. Then, the energy distribution function of the beam is simply Eq. 3.5 integrated over all r, θ and z,

$$f(E_\parallel) = \frac{n_0}{\sqrt{\pi} T^{\frac{3}{2}}} \int \frac{\exp\left(-\frac{E_\perp + E_\parallel + e\phi_0(r)}{T}\right)}{\sqrt{E_\parallel + e\phi_0(r)}} dE_\perp dr d\theta dz, \tag{3.6}$$

under the condition that $E_\parallel > eV_{\rm E}$; $f(E_\parallel) = 0$ otherwise. Because the $E_\perp$ dependence is trivial and does not change during the extraction process, we here integrate over it to obtain the projection of the distribution function onto $E_\parallel$ space. This will be done in the future with the understanding that the distribution in $E_\parallel$ space is related to the full 3 dimensional distribution function by the trivial transformation,

$$f(E_\parallel, E_\perp) = f(E_\parallel)e^{-E_\perp/T}/T. \tag{3.7}$$

After evaluating Eq. 3.6, we arrive at the energy distribution function for a small beam,

$$f(E_\parallel) = \frac{L_{\rm p}}{e^2}{\rm erfc}\left(\sqrt{\frac{{\rm E}_\parallel + {\rm e}\phi_0(0)}{{\rm T}}}\right), \tag{3.8}$$

where erfc is the complementary error function. Again, this is only valid for small beams and values of $E_\parallel > eV_{\rm E}$; $f(E_\parallel) = 0$ for $E_\parallel < eV_{\rm E}$. When $[E_\parallel + e\phi_0(r)]/T \geq 2$, Eq. 3.8 is approximately,

$$f(E_\parallel) \approx \frac{L_{\rm p}\sqrt{T}}{e^2\sqrt{\pi}}\frac{\exp\left(-\left[E_\parallel + e\phi_0(0)\right]/T\right)}{\sqrt{E_\parallel + e\phi_0(0)}}. \tag{3.9}$$

This is the approximate energy distribution for small beams (i.e., $\xi \ll 1$) when $\triangle\phi$ is negligible. It is also just the tail of a Maxwellian energy distribution starting at energy $|e\phi_0(0)|$.

For larger beam amplitudes, $\triangle\phi(r)$ cannot be neglected and the simple expression for the energy distribution function in Eq. 3.6 is invalid. Now it is necessary to first calculate the total number of escaping particles $N_{\rm b}$ as a function of $V_{\rm E}$ before the energy distribution function can be obtained. To accomplish this, we must first find an accurate approximation for $\triangle\phi(r)$. In Sec. 2.2, it was shown that for $\xi < 1$, radial beam profiles are Gaussians with widths given by

$$\rho_{\rm b} = 2\lambda_{\rm D}(1 + \xi)^{\frac{1}{2}}. \tag{3.10}$$

Further, Sec. 2.2 defined $\triangle\phi(r)$ for these Gaussian beams as,

$$\triangle\phi(r) \;=\; \frac{T\xi}{e}\left[2\ln\frac{r}{R_{\mathrm{W}}} + \Gamma\left(0,\frac{r^2}{\rho_{\mathrm{b}}^2}\right) - \Gamma\left(0,\frac{R_{\mathrm{W}}^2}{\rho_{\mathrm{b}}^2}\right)\right]$$

$$\approx \;\; \triangle\phi(0) + \xi\frac{T}{e}\frac{r^2}{\rho_{\mathrm{b}}^2}, \tag{3.11}$$

where Γ is the upper incomplete gamma function. This expression can be inserted into Eq. 3.5 [i.e., as $\phi(r) = \phi_0(r) - \triangle\phi(r)$] and integrated over all space, both position and energy, with condition that $E_\parallel > eV_{\mathrm{E}}$ to obtain an expression for the total number,

$$N_{\mathrm{b}} = \frac{n_0}{\sqrt{\pi}T^{\frac{3}{2}}}\int_{E_\parallel > eV_{\mathrm{E}}} \frac{\exp\left(-\frac{E_\perp + E_\parallel + e\phi(r)}{T}\right)}{\sqrt{E_\parallel + e\phi(r)}} dE_\parallel dE_\perp dr d\theta dz. \tag{3.12}$$

Evaluating this expression gives,

$$\xi = (1+\xi)\left[\frac{Ae^{-A^2}}{\sqrt{\pi}} - (A^2 - 0.5)\mathrm{erfc}(A)\right], \tag{3.13}$$

where

$$A = \sqrt{\eta + \xi\left[\gamma + 2\ln\frac{R_{\mathrm{W}}}{\rho_{\mathrm{b}}} + \Gamma\left(0,\frac{R_{\mathrm{W}}^2}{\rho_{\mathrm{b}}^2}\right)\right]},$$

and γ is the Euler gamma constant. Here, the expression has been conveniently written in terms of ξ, $R_{\mathrm{W}}/\lambda_{\mathrm{D}}$ and the parameter,

$$\eta \equiv -\frac{e}{T}\left[V_{\mathrm{E}} - \phi_0(0)\right]. \tag{3.14}$$

In Eq. 3.13, the quantities ξ and η are the suitably scaled values of N_{b} and V_{E}, respectively. Equation 3.13 is very useful in that for an initial plasma and extraction voltage, one obtains N_{b}. Thus, it is now possible to know N_{b}, and subsequently $\sigma_{\mathrm{b}}(r)$ and ρ_{b}, without having to measure the beam. Although Eq. 3.13 is not transcendental in ξ, the analytical expression for $\xi(\eta)$ will not be written out. One reason for this is Eq. 3.13 is already in a very convenient form, as all the $\triangle\phi$ effects are isolated on the right hand side (RHS) of the equation. Thus, by simply setting $\xi = 0$ on the RHS, an expression for ξ remains when $\triangle\phi$ is negligible. Further, the

analytic expression for $\xi(\eta)$ is very long and complicated. With the availability of computers, it is much easier to simply find a self-consistent numerical solution to Eq. 3.13 for fixed values of R_W/λ_D, rather then to write out each term in the long expression for $\xi(\eta)$.

The real power of Eq. 3.13 is that now, using this equation, the energy distribution function of the beam including $\triangle\phi$ effects can be obtained without the approximations made in arriving at Eq. 3.8. The more accurate parallel energy distribution function is then simply,

$$f(E_\parallel) = -\frac{1}{e}\frac{dN_b}{dV_E}, \qquad (3.15)$$

evaluated at $E_\parallel = -eV_E$. Or, in the new scaled variables,

$$f(\eta) = \frac{e^2}{L_p}\frac{d\xi}{d\eta}, \qquad (3.16)$$

evaluated at $\eta = \left[E_\parallel + e\phi_0(0)\right]/T$. Again, for the reasons stated above, Eq. 3.16 will not be evaluated analytically. Now, for a given plasma and V_E, the total number, width, spatial and energy distribution of the beam are obtained a priori. Unfortunately, Eq. 3.13, and consequently Eq. 3.16, are very sensitive to the equilibrium plasma potential $\phi_0(0)$, which is only known to $\pm 10\%$ due to uncertainties in L_p. When testing the equations developed here, we will determine $\phi_0(0)$ more precisely by varying it to find the best fit of Eq. 3.13 to data.

As will be shown below, the shape of $f(E_\parallel)$ varies significantly as ξ is changed. In order to provide a clear and concise measure of the distribution function resulting from these changes, we will here define the mean and root-mean-squared energies of the distribution. We define the mean energy relative to the minimum energy of the beam $E_{min} = -eV_E$ as,

$$\delta\bar{E} = \langle E \rangle - E_{min}, \qquad (3.17)$$

and the dispersion in energy (i.e., root-mean-square deviation from the total mean energy) as

$$\triangle E = \sqrt{\langle E^2 \rangle - \langle E \rangle^2}. \qquad (3.18)$$

In Eqs. 3.17 and 3.18, $<>$ denotes the average of the quantity over the full distribution function of the beam $f(E_\parallel, E_\perp, r)$. If one wishes to find the expressions in parallel energy space only, use the relations,

$$\left\langle E_\parallel \right\rangle = \langle E \rangle - T, \tag{3.19}$$

and

$$\triangle E_\parallel = \sqrt{\triangle E^2 - T^2}. \tag{3.20}$$

The quantities in Eqs. 3.17 and 3.18 will be calculated below as a function of ξ and R_W/ld. In the small beam limit ($\xi \to 0$), $\delta \bar{E} \to 2T$ and $\triangle E \to \sqrt{2}T$; while in the dilute charged gas limit (i.e., the non-plasma limit; $|e\phi_0(0)| \ll T$ and $N_b = N_0$), $\delta \bar{E}$ and $\triangle E$ are $(3/2)T$ and $\sqrt{3/2}T$ respectively. The difference between these two cases is that for the former, only the tail of the Maxwellian is extracted as opposed to the entire thermal distribution in the latter.

3.2 Comparison between theory and experiment

Shown in Fig. 3.1 are data for the beam amplitude N_b extracted as a function of V_E, together with two predictions of the theory. The initial plasma parameters were $N = 4 \times 10^8$, $n = 1 \times 10^9$ cm^{-3}, $T = 1$ eV, and $L_p = 15$ cm. The dashed line is the prediction of Eq. 3.13 when ξ is neglected on the RHS. This results in a direct expression for ξ when $\triangle \phi(r)$ can be neglected during the beam extraction process (i.e., for small beams). As seen in the figure, these predictions agree with the data for small values of N_b (or ξ), however they diverge rather dramatically for larger values of N_b. Because $\triangle \phi(r)$ acts to inhibit particles from escaping, neglecting it results in a large overestimation of the number of escaping particles. The solid line in Fig. 3.1 is the prediction of Eq. 3.13 solved self-consistently, with $\phi_0(0)$ adjusted for best fit for the reasons discussed in Sec. 3.2. In this case, the predictions and the data are in excellent agreement.

The beam parallel energy distribution $f(E_\parallel)$ is found from Eq. 3.15, or by numerically by taking the derivative $dN_b/d(eV_E)$ of the data and predictions shown

in Fig. 3.1. This results in both measured and predicted values of $f(E_\parallel)$. For the curve with ξ neglected on the RHS of Eq. 3.13, this derivative is of course identical to Eq. 3.8. The experimental and predicted distribution functions are shown in Fig. 3.2 for two values of ξ. As shown in Fig. 3.2, for the smallest-amplitude beam ($\xi = 0.02$), $\triangle\phi(r)$ can be neglected and the predictions of Eq. 3.8 agree well with the data. For the larger beam ($\xi = 0.4$), the predictions of Eq. 3.8 deviate significantly from data. Equation 3.8 does a poor job at predicting $f(E_\parallel)$ due to the non-negligible effect of $\triangle\phi(r)$. However, good agreement is seen with the predictions using the derivative to the full solution to Eq. 3.13, even for the relatively large beam of $\xi = 0.4$. The corresponding values of $\triangle E/T$ ($\delta\bar{E}/T$) for the distributions shown in Fig. 3.2 are 1.4 (2.0) and 1.8 (3) for $\xi = 0.02$ and 0.4, respectively.

With the validation of the predictions of Eq. 3.13, we consider further its implications for a wide range of plasma parameters and beam amplitudes. Equation 3.13 relates ξ to η with the only adjustable constant being the dimensionless parameter R_W/λ_D. Given R_W/λ_D, one can then solve for ξ as a function of η, relating N_b to V_E for given values of the plasma parameters (i.e., T, n, and L_p). In Fig. 3.3, solutions to Eq. 3.13 are shown for three values of R_W/λ_D spanning a factor of 100 in this parameter. The data from Fig. 3.3 are scaled appropriately and included for reference. As can be seen in Fig. 3.3 and by examining Eq. 3.13, the curves have a noticeable, but relatively weak, dependence on R_W/λ_D.

The energy distribution functions can then be obtained from the solutions for $\xi(\eta)$ using Eq. 3.16. Results are shown in Fig. 3.3 for $\xi = 0.4$ and three values of R_W/λ_D. These energy distributions vary markedly in shape as R_W/λ_D is increased. Useful measures of the changes in the distribution function are obtained by calculating the moments (Eqs. 3.17 and 3.18) of the distribution given by Eqs. 3.13 and 3.16. In Fig. 3.4, the mean beam energy $\delta\bar{E}$ is shown as a function of ξ for a range of R_W/λ_D. This is a critical parameter for many applications. Also shown in Fig. 3.4 are measured data for $R_W/\lambda_D = 50$ that are in good agreement with the predictions. The calculated rms energy spread $\triangle E$ is also shown as a function of ξ for the same values of R_W/λ_D. Experimental data for $R_W/\lambda_D = 50$ are used
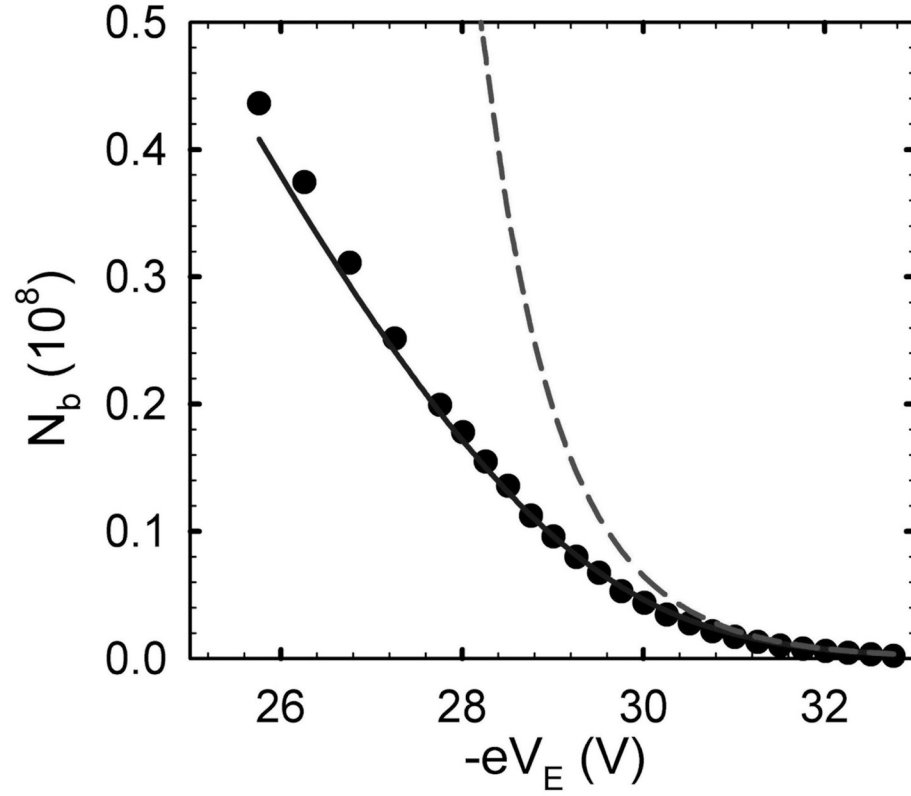
Figure 3.1: The number of beam particles N_b ($\bullet$) is shown as a function of the extraction voltage V_E. Here, $T = 1.0$ eV, $n_0 \approx 1 \times 10^9$ cm^{-3} and $\phi_0(0) = 27$ V. Also shown are the predictions of Eq. 3.13 (—), solved numerically, along with the solution (- - -) obtained from Eq. 3.13 when setting $\xi = 0$ on the RHS.
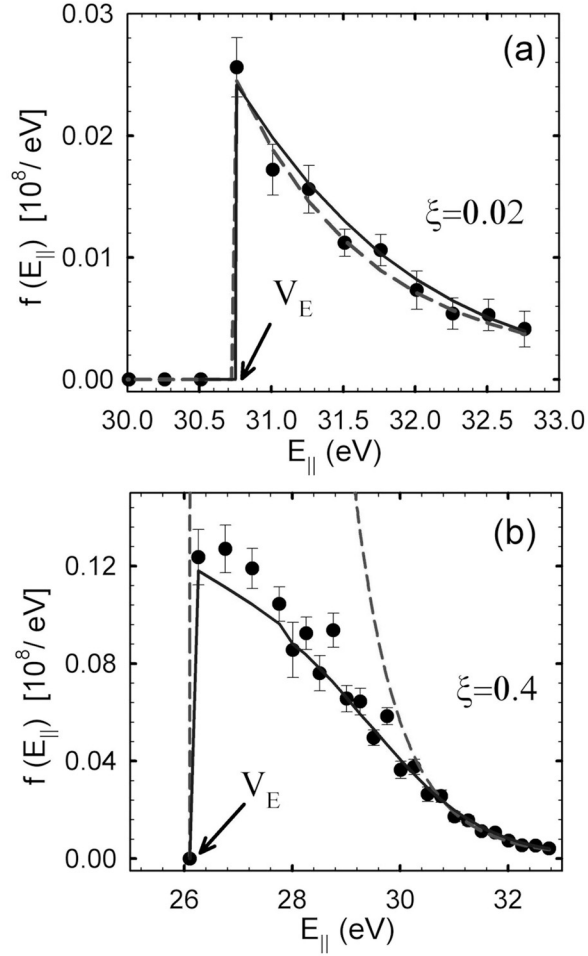
Figure 3.2: Comparison of the beam energy distribution functions $f(E_{\parallel})$ for different beam amplitudes: (a) $\xi = 0.02$ and (b) $\xi = 0.4$. These distributions were obtained from Eq. 3.15 using the experimental data and the theoretical predictions shown in Fig. 3.1. The experimental conditions and symbols are the same as in Fig. 3.1.
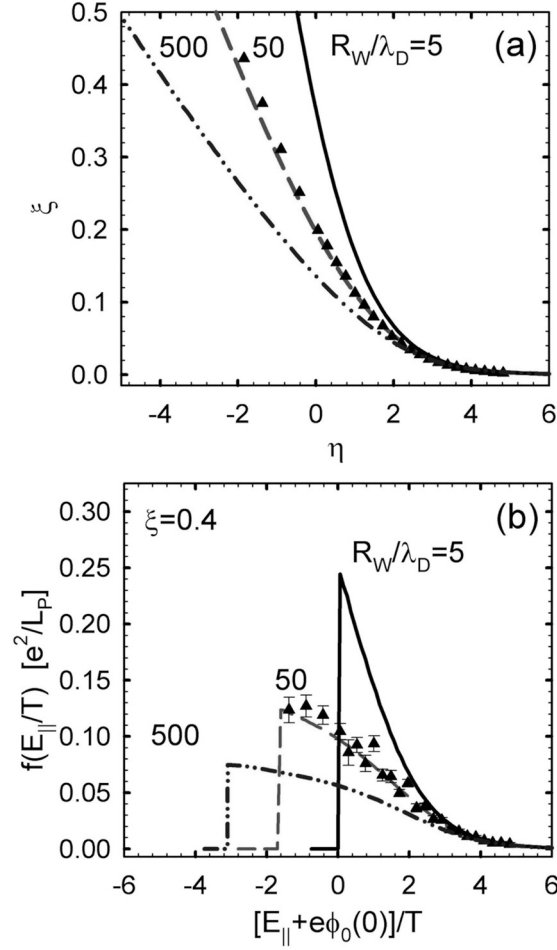
Figure 3.3: (a) Numerical solutions to Eq. 3.13 (—, - - -, -··) are shown for values of R_W/λ_D of 5, 50, and 500, respectively. (b) the corresponding energy distribution functions $f(E_\parallel)$ are shown scaled by $(e^2/L_p)^{-1}$, calculated with Eq. 3.16 using the solutions shown in (a). Data from Fig. 3.1 (▲) are also plotted in (a) and (b).

and seen to be in good agreement with the predictions. For applications where good energy resolution is required, it is desirable to have as small a value of $\triangle E$ as possible. While increasing the beam amplitude increases $\triangle E/T$, this has a diminishing effect for plasmas with smaller R_W/λ_D. The reason for this can be seen by approximating $\triangle\phi(0)$ as that from a 'flat top' and then expressing it as,

$$\left|\frac{e\triangle\phi(0)}{T}\right| \approx \xi\left[1 + 2\ln\frac{R_W}{\lambda_D} - \ln 4\,(1+\xi)\right]. \tag{3.21}$$

The increase in $\triangle E/T$ with R_W/λ_D is related to the number of particles that are prevented from escaping at $r = 0$ by the change in $\triangle\phi(0)$. Equation 3.21 shows that for small R_W/λ_D, $\triangle\phi(0)$ has a diminishing effect. Notice that for a given ξ, while increasing R_W/λ_D does increase $e\triangle\phi/T$, it does so slowly (i.e., logarithmically). Physically, this can happen either by decreasing λ_D thereby making the beam smaller which increases $\triangle\phi(0)$, or by increasing R_W which decreases the effect of the screening image charge on the cylindrical electrodes, hence increasing $\triangle\phi(0)$. As mentioned above, increasing $\triangle\phi$ will prevent more particles from escaping thus increasing the energy spread of the resulting beam (c.f., Fig. 3.4).

Note in Fig. 3.4, as ξ increases the spread in $E_\perp$ remains constant; only the parallel energy distribution contributes to the increase in $\delta\bar{E}$ and $\triangle E/T$. In particular, the dispersion in the parallel energy is given in Eq. 3.20. This provides a convenient relation between $\triangle E$ and $\triangle E_\parallel$. Notice $\triangle E_\parallel$ increases from 0.9 to 1.5 as ξ increases from 0.02 to 0.4 in the data shown in Fig. 3.4.

3.3   Summary

It has been shown that the method to create beams with small transverse spatial extent presented in this thesis also produces cold beams of narrow energy spreads. Specifically, the energy spread of the beam is set by the parent plasma temperature, which can be made mall via cycltron cooling (e.g., $T < 25$ meV). Such beams are expected to be useful in many applications. For example, the creation of beams with small transverse spatial and energy spreads is critical in the development of positron microscopic techniques to study materials [29, 51]. In
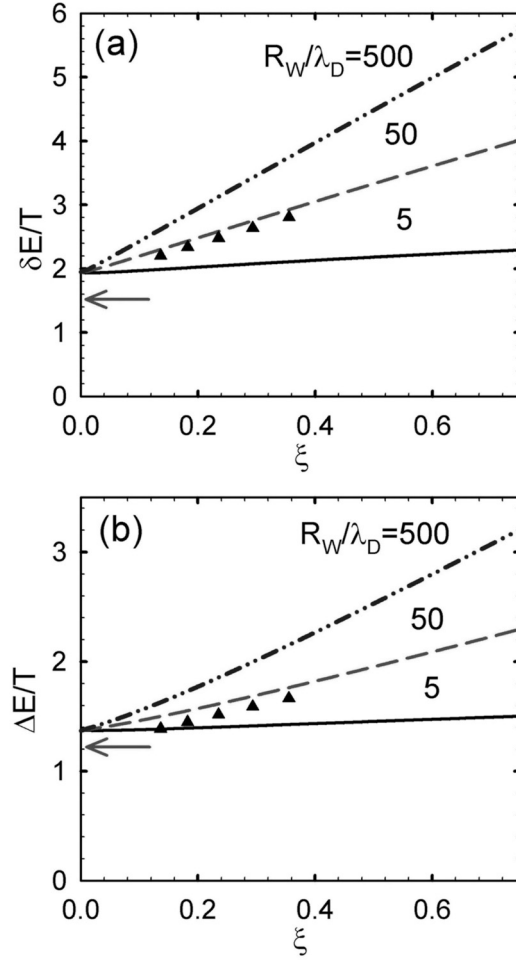
Figure 3.4: The quantities (a) the mean energy, $\delta \bar{E}/T = \langle E - E_{\min} \rangle /T$ (i.e., $E_{\min} = -eV_{\mathrm{E}}$); (b) rms spread in total energy $\triangle E/T$ calculated using Eqs. 3.13, 3.16, 3.17 and 3.18 are shown as a function of ξ for three values of $R_{\mathrm{W}}/\lambda_{\mathrm{D}}$. Data for plasma parameters given in Fig. 3.1 (▲) are also shown for $R_{\mathrm{W}}/\lambda_{\mathrm{D}} = 50$. Arrows indicate the value for a Maxwellian beam. Curves are marked the same as Fig. 3.3. See text for details.

other applications, beams with small total energy spreads will enable new kinds of spectroscopic studies of positron interactions with matter such as higher resolution studies of positron-impact excitation of vibrational and rotational transitions in molecules [58, 41, 60]. Similarly, beams with narrow parallel energy spreads will facilitate pulse compression in the time domain. This, in turn, could enable the development of new techniques for positron annihilation lifetime spectroscopic (PALS) studies of materials [43, 56, 55, 20, 62, 24, 1, 9]. A final important application of cold positron beams is the creation of cold antihydrogen atoms [21, 2]. For this applications, the low energies of antihydrogen required for magnetic trapping (< 4 K) necessitate extremely cold positron and antiproton beams.

Chapter 4

Electrostatic Beam

4.1 Introduction

A current limitation on beams created in Chs. 2 and 3 is that they reside in a large magnetic field. This presents a problem for applications that require an electrostatic positron beam (i.e., a positron beam in a magnetic field free region) [42, 60]. For example, electrostatic beams provide increased sensitivity in studying angular scattering from atomic and molecular targets [60, 36], and they have the long-term potential of leading to a positron reaction microscope [64]. One can also use electrostatic techniques for additional positron beam focusing and so-called "remoderation" to further enhance beam brightness [42, 24] for applications such as Ps_2 and Ps-BEC formation [45]. For these applications, extraction of the beam from the magnetic field is required. However, this process presents many difficulties including a potentially dramatic increase in the beam width and mean transverse energy $\overline{E}_\perp$ [32], which is deleterious for some applications.

Motivated by these considerations, we will now demonstrate a technique to extract a class of high quality electrostatic beams from a Penning-Malmberg trap. The initial beam is formed using the techniques presented in Ch. 2. The extraction from the field is then done in two stages: the beam is first transported to a region of much lower field (1 mT), followed by a fast (i.e., non-adiabatic) extraction to zero field. Once in this zero-field region, the beam is focused using an Einzel lens to demonstrate electrostatic beam control and to decrease the transverse beam size

while conserving the beam emittance ϵ [54].

4.2   Description of the experiments

The initial beam formation process in the 4.8 T field is identical to that used in the previous two chapters. As a reminder, these beams have Gaussian radial profiles [i.e., z-integrated areal particle distribution $\sigma_b(r)$] of the form,

$$\sigma_b(r) = \sigma_{b0} \exp\left[-\left(r/\rho_b\right)^2 \right], \tag{4.1}$$

where σ_{b0} is a constant and,

$$\rho_b = 2\lambda_D \left(1 + \xi\right)^{1/2}, \tag{4.2}$$

with

$$\xi = e^2 N_b / T L_p, \tag{4.3}$$

the total number of beam particles per pulse N_b scaled by the plasma temperature T and length L_p.

The magnetic extraction process is illustrated in Fig. 4.1. The beam is first transported adiabatically from the 4.8 T field to 1 mT before undergoing a rapid extraction from the field. The beam-transport energy used here is ≈ 30 eV. An important parameter used to measure the (non)adiabaticity of the process is,

$$\gamma = \frac{\tau_{cyc} dB/dt}{B}, \tag{4.4}$$

where τ_{cyc} is an electron gyroperiod and dB/dt is the rate of change of the magnetic field in the beam frame. Ideally, transport to low field is done in a manner such that $\gamma \ll 1$. In this case, the beam particles conserve the adiabatic invariant J defined by,

$$J = \frac{E_\perp}{B}, \tag{4.5}$$
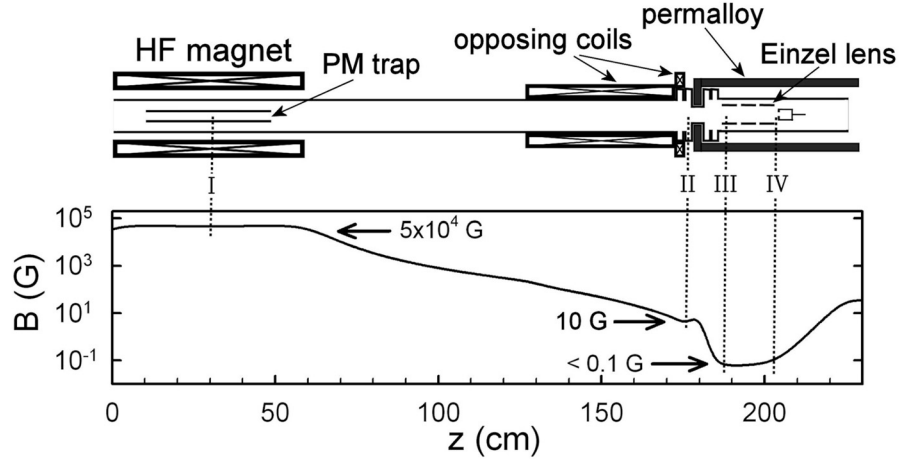
Figure 4.1: (above) Schematic diagram of the experiment illustrating the magnetic extraction, followed by the Einzel lens spatial focus to a collector cup. (below) The on-axis magnetic field (oriented in the z direction) $B_z(r = 0)$. Saddle coils used to align the field at $z \approx 140$ cm are not shown.

where $E_\perp$ is the kinetic energy in the motion perpendicular to the magnetic field, namely $E_\perp = 1/2mv_\perp^2$, with $v_\perp = \sqrt{v_\theta^2 + v_r^2}$ [67]. Qualitatively, during the transition to lower fields, the particles stay glued to their respective magnetic field lines while undergoing small-scale gyromotion. As illustrated in Fig. 4.1, the field is allowed to fall off naturally as the particles exit the high field (HF) magnet. Opposing coils (at $z \approx 150$ and 175 cm in Fig. 4.1) precisely define the field after the magnetic reduction and shorten the length of the experiment. Over most of the slow magnetic reduction, Eq. 4.5 is well satisfied while in the last 10 cm, gamma is larger, namely $|\gamma| \approx 0.6$.

One key difficulty in this experimental arrangement is aligning precisely the HF magnet with respect to the beam tube (i.e., the vacuum chamber supporting the opposing solenoid). This is accomplished by first imaging the beam on a phosphor screen temporarily mounted at the end of the low field region where the permalloy shield begins. The orientation of the HF magnet is adjustable, and it is aligned until the beam is visible on the screen. Once this is accomplished, saddle coils, placed at the beginning of the first opposing solenoid ($z \approx 140$ cm in Fig. 4.1), are used to center the beam in the tube.
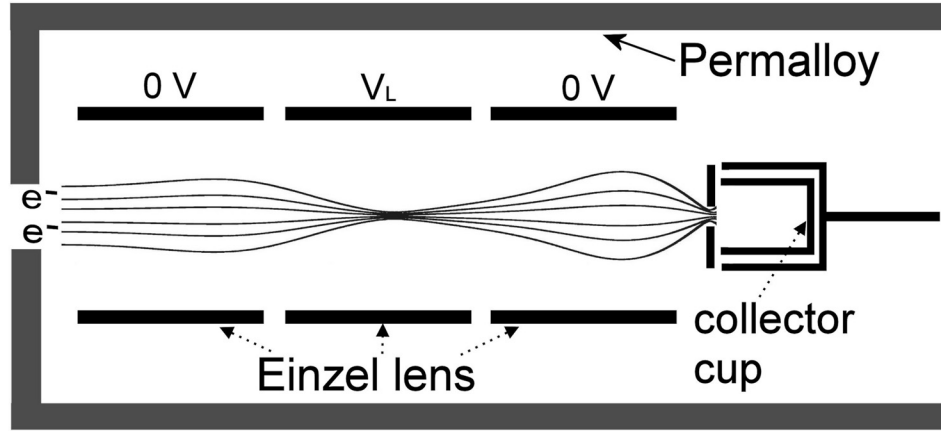
Figure 4.2: Schematic diagram of the Einzel lens and collector cup.

At the end of the low field region ($z \approx 180$ cm in Fig. 4.1), a non-adiabatic (i.e., $\gamma \gg 1$), fast extraction is performed in which the adiabatic invariant in Eq. 4.5 is not conserved. In this more or less standard technique [51], the particle has no time to respond to the $v \times B$ forces from the flaring magnetic field due to the fact that the field changes so quickly. As a result, the radial positions of the particles remain constant while they undergo an increase in the azimuthal component of their velocity v_θ from the short impulse due to the Lorentz force. This impulse is radially dependent and will be referred to later as a "kick".

Experimental details of the fast extraction are shown in Figs. 4.1 and 4.2. It is accomplished using a high magnetic permeability shield (made of sheets of Permalloy, $\mu_\mathrm{r} \sim 2 \times 10^4$) with a front cap that has a hole in the center of diameter $d \approx 5$ cm. This hole forms a tight fit around the necked down portion of the beam tube ($z \approx 175$ cm in Fig. 4.1). The Permalloy screens the magnetic field from inside the shield and creates a fast extraction region at the beginning of the front-cap hole where $B = 1 \to 0$ mT.

The currents required in the two opposing coils to obtain the desired fields were initially calculated numerically using the Poisson Superfish codes [6]. They were then determined more precisely by measuring the on-axis magnetic field near the shield using a Hall probe. This was necessary because the computer code could not achieve the magnetic field precision that is required (i.e., a reduction in B by

a factor $\sim 10^4$).

Inside the magnetic shield, the beam is guided only by electrostatic fields (i.e., a so-called electrostatic beam). As illustrated in Fig. 4.2, it is then focused with an Einzel lens and the beam properties are measured with an apertured collector cup mounted on a movable linear feed-through. The Einzel lens consists of three identical hollow cylinders (≈ 6 cm in length and inner diameter) that are electrically isolated from the chamber and from each other. The lens is operated in an acceleration-deceleration mode where the center electrode is biased to a large positive voltage V_L and the two exterior electrodes are grounded.

Once focused, the z-integrated central beam intensity is measured with the collector cup. The aperture on the cup has a centered hole of diameter $d \approx 0.24$ cm which is used to estimate the maximum rms transverse spatial spread of the beam $\Delta r = <r^2>^{1/2}$. Note that for a Gaussian beam, $\Delta r = \rho_b$. By moving the collector in the z direction, the focal position of the lens is found as the position of maximum collector signal. After the approximate focal position is determined, the saddle coils are adjusted to (iteratively) maximize the signal on the collector and thereby precisely center the beam. This process must be repeated every few days to account for small systematic changes in the experiment. The beam-pulse intensity is also measured upstream by gathering charge on a collector plate. This measurement is used together with the collector-cup signal to obtain the percentage of the beam that passes through the collector-cup aperture.

4.3   Experimental results

Electrostatic beams were created using the experimental apparatus and procedures described in Sec. 4.2. Figure 4.3 illustrates the initial radial beam distribution in the 4.8 T field. Beam pulses (≈ 5 μsec in duration) were extracted from parent plasmas with parameters: $N \approx 3.5 \times 10^8$ electrons; $n \approx 1.2 \times 10^{10}$ cm^{-3}; $T \approx 0.1$ eV; and $L_p \approx 15$ cm. The beam parameters are the number of particles per pulse $N_b \approx 3.4 \times 10^6$ and scaled beam amplitude $\xi \approx 0.4$ [cf., Eq. 4.3]. The transport energy of the beam is 30 V, which is set by the plasma potential. The

perpendicular energy spread is Maxwellian with $T = 0.1$ eV, while the parallel energy spread is non-Maxwellian [65]. The total energy spread is found to be $\triangle E \approx 0.24$ eV from previous work [65]. Inserting the relevant parameters into Eq. 4.2 yields a beam width $\rho_b \approx 54$ μm in the 4.8 T field, which is in reasonable agreement with the measured value of $\rho_b = 65$ μm.

This beam is then extracted from the 4.8 T field in the manner described in Sec. 4.2 to produce an electrostatic beam. Due to adiabatic expansion from the slow reduction to $B = 1$ mT, the beam has a width $\rho_b \approx 0.45$ cm, which remains unchanged in the extraction from the field. The beam is then focused with an Einzel lens and detected using the apertured collector cup illustrated in Fig. 4.2. Data for the collected beam particles as a function of the z-position of the collector aperture are plotted as solid points in Fig. 4.4, where $z = 0$ corresponds to the end of the lens ($z \approx 205$ cm in Fig. 4.1), and the sign convention for z is that used in Fig. 4.1. The data are expressed as the percentage of beam particles transmitted through the aperture at a given value of z. The voltage applied to the center electrode of the lens for this scan was $V_L = 5$ kV. Operationally, we define the focus (i.e., the focal position) of the lens as the z position of maximum transmission through the aperture. For the data shown in Fig. 4.4, it occurs at $z \approx 5$ mm, where $\approx 43\%$ of the beam passes through the aperture of diameter $d = 0.24$ cm. Note the marked asymmetry of the focusing curve as a function of z, namely a fast rise followed by a slower decline beyond the focus. This is related to lens abberations and will be discussed further in the next section.

Unfortunately, this experiment does not have the capabilities to measure a beam profile at the focal position. Because these beams are non-Gaussian (cf., Sec. 4.4), the only quantity that can be reported is the maximum width of the attenuated beam that passes through the collector aperture (i.e., $\Delta r < 0.12$ cm for the data shown in Fig. 4.4).

To study the dependence of the focusing on the lens voltage, V_L was varied from 2 to 6 kV while curves similar to those shown in Fig. 4.4 were measured. The focal position as a function of V_L is plotted in Fig. 4.5. As V_L is decreased, the position of maximum focus moves farther away from the lens, while for larger
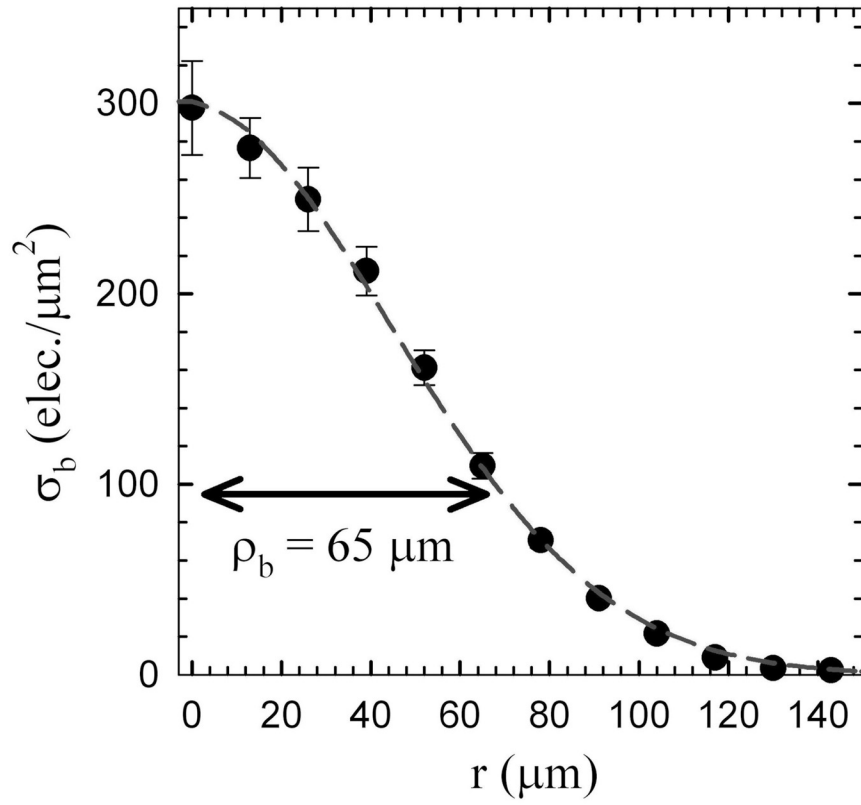
Figure 4.3: The initial beam in the 4.8 T field. The beam parameters are $N_b \approx 3.4 \times 10^6$, $\xi \approx 0.4$, and $\triangle E \approx 0.24$ eV. A fit to Eq. 4.1 is plotted (- - -), with $\rho_b \approx 65$ μm.
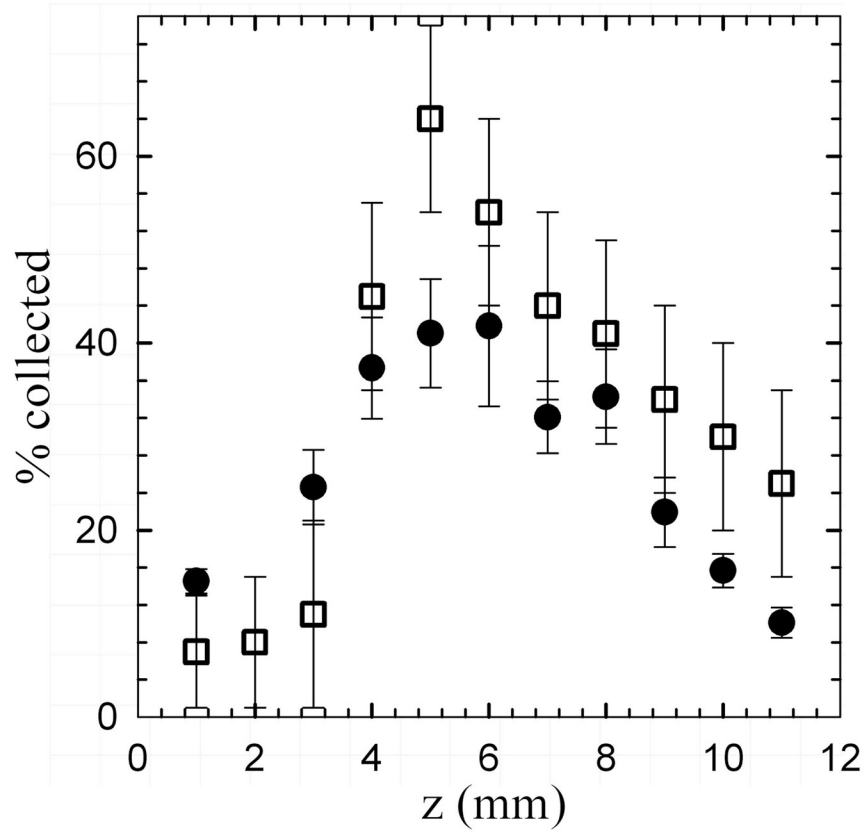
Figure 4.4: The percentage of the beam that is transmitted through the collector aperture ($d = 0.24$ cm) vs. the z-position of the aperture ($\bullet$). Here, $V_\mathrm{L} = 5$ kV. Shown also are the predictions ($\square$) based on numerical simulations of the particle trajectories (cf., Sec. 4.4).
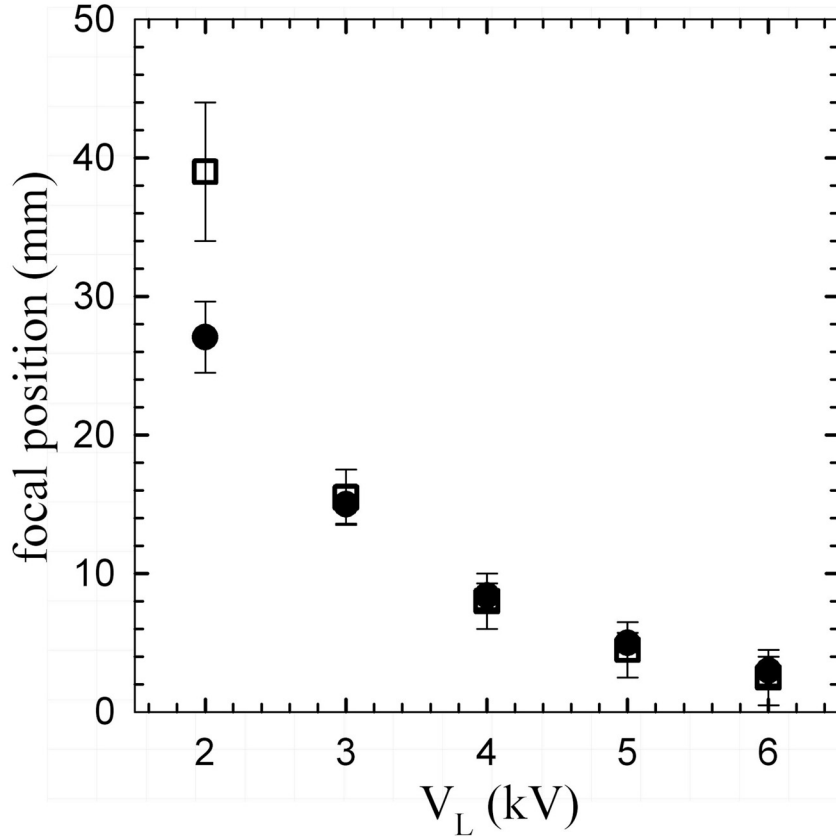
Figure 4.5: The measured focusing position of the lens vs. the applied lens voltage V_{L} (●). Shown also are the predictions of numerical particle simulations (□) described in Sec. 4.4.

values of V_{L}, the focus approaches the position of the end of the lens at $z = 0$.

In Fig. 4.6, the percentage of beam particles passing through the aperture is plotted as a function of the lens voltage V_{L} for the same initial beam conditions as the data in Fig. 4.4 [1]. The transmission rises as a function of V_{L} and then saturates. At $V_{\mathrm{L}} = 6$ kV, $\approx 55\%$ of the beam passes through the aperture.

[1]The data point at the focal point in Fig. 4.4 differs slightly from that at $V_{\mathrm{L}} = 5$ kV in Fig. 4.6, likely due to run-to-run differences in the experimental conditions.
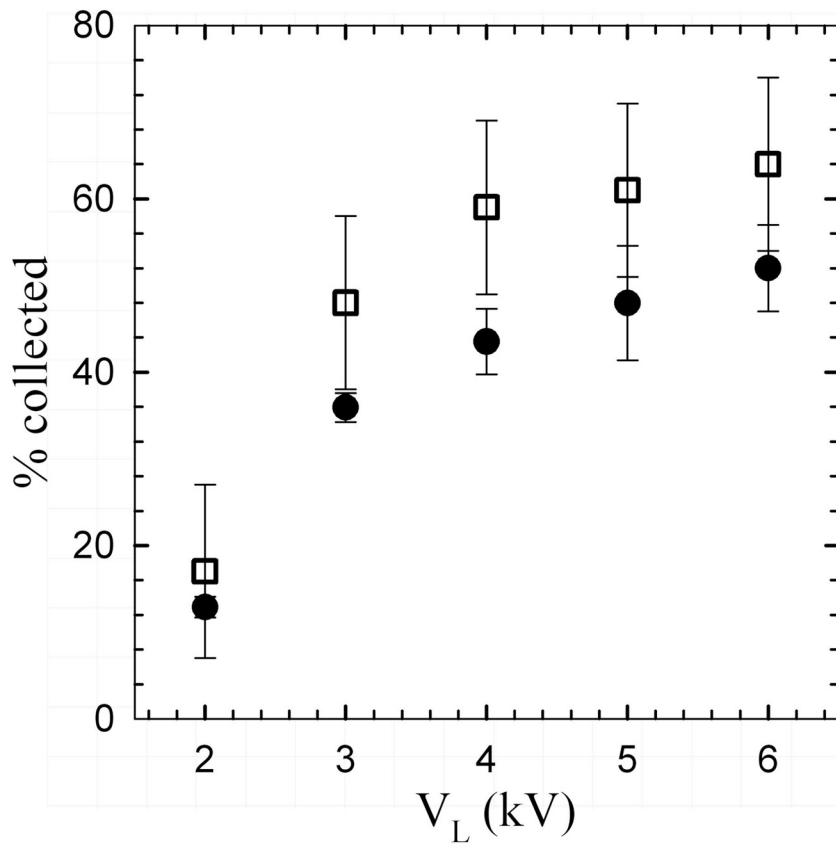
Figure 4.6: The percentage of the beam particles transmitted through the aperture vs. V_L ($\bullet$) for the beam shown in Fig. 4.3. Theoretical predictions based on the particle simulations discussed in Sec. 4.4 are also shown ($\square$).

4.4 Numerical simulations

In order to interpret the experimental data and extrapolate to different experimental conditions, the electron trajectories through the electric and magnetic fields during the fast extraction and Einzel lens focus were simulated using numerical methods. The electric and magnetic fields are calculated from the lens, collector, permalloy, and coils (see Fig. 4.1) using the Poisson Superfish code [6]. The assumption is made that the Gaussian beam in Fig. 4.3 has been slowly transported from the HF trap to 1 mT. Then, a sampling of the beam particle trajectories is calculated through the fast extraction region and Einzel lens. The percentage of beam particles passing through the aperture and focal position of the lens are estimated from these trajectories.

Three of these trajectories are plotted in Fig. 4.7 for two different values of V_L. Notice the scale difference in both z and r between the two panels shown in Fig. 4.7. For $V_L = 5$ kV, the focus occurs at significantly smaller values of r, and across a smaller region in z, than for $V_L = 2$ kV. For a given initial radius and kick (cf., Sec. 4.5), the minimum particle radius scales as $1/V_L$. For all trajectories studied (ignoring aberrations, discussed below), there is a linear relation between the initial radius r_i and the minimum radius $r_f$. This minimum radius is set by the initial angular momentum of the particles immediately following extraction from the field, which is proportional to the δv_θ kick that they receive when exiting the magnetic field (cf., Sec. 4.5). The smaller the kick, the closer the particles approach the z-axis at $r = 0$. The focus moves farther away from the lens as the incident beam energy is increased. This is because at higher incoming energies the beam particles spend less time in the lens, and hence are less affected by the focusing electric fields. For $V_L = 5$ kV, the focus is at 2, 6 and 27 cm for beam energies of 15, 30 and 60 eV, respectively.

Predictions for the radial beam profiles at the focus are also plotted in Fig. 4.7. They show relatively large departures from the initial Gaussian beam profiles used as inputs in the simulations. This is primarily due to lens aberrations, namely the fact that particles with different initial radii focus at different values of z. For $V_L = 2$ kV, the profile shows a significant departure from the initial

Gaussian, while for $V_{\mathrm{L}} = 5$ kV, the distortion is even more extreme. Thus the Gaussian parameter ρ_{b} is no longer a good measure of the beam width at the focus. Instead, we use the rms transverse spatial spread of the beam Δr. In Fig. 4.7, the values for Δr are 2.0 and 1.0 mm for $V_{\mathrm{L}} = 2$ and 5 kV respectively.

The observed aberrations arise when particle trajectories pass through larger values of r in the lens (i.e., when $r \sim 0.5 R_L$, where R_L is the radius of the lens). There are two primary mechanisms for particles sampling large values of r. One is that when the particles start out at larger radii, they experience stronger radial electric fields and larger δv_θ kicks (cf., Sec. 4.5) thus causing their trajectories to traverse larger radii in the lens. The second mechanism is due to the fact that for large values of V_{L}, the large radial electric fields of the lens push particle orbits to larger radii in the lens.

The trajectories shown in Fig. 4.7 do not include effects from the collector. Including the potential surfaces of the collector makes only small changes, namely shifting the trajectories in the z direction by a relatively small amount ($\delta z \approx -2$ mm) and increasing the minimum radius by $\approx 5\%$. When comparing the calculated trajectories to the experimental data, as described below, these collector effects were included.

Trajectories such as those shown in Fig. 4.7 were used to simulate the experimental data shown in Figs. 4.4-4.6. The predictions rely on knowledge of the beam profile in the 1 mT region. This quantity could only be estimated and is subject to (what turns out to be) significant error (i.e., $\rho_{\mathrm{b}} = 0.45 \pm .05$ cm). One factor contributing to this uncertainty is that the orbits are not strictly adiabatic in the 10 cm or so just before the fast extraction (i.e., here $|\gamma| \sim 0.4 - 0.6$). There are also uncertainties in the exact magnetic topology at the extraction point and imperfections in the beam transport system such as the effect of the saddle coils. Both effects would alter the beam width while the latter would additionally change the assumed Gaussian form of the beam, thus altering the predicted values. The image of the beam on a phosphor screen near the entrance to the field-free region does indicate a moderate degree of asymmetry, implying imperfections in the beam transport system. As a result, the theoretical predictions shown in Figs. 4.4-4.6

have relatively large uncertainties, as indicated by the error bars on the simulated data points in these figures. It is important to note that these uncertainties are related to a systematic error in the estimate of ρ_b and are therefore correlated. Thus, the error bars in Figs. 4.4-4.6 represent the range of potential systematic shifts of the theoretical curves.

The experimental data and theoretical predictions plotted in Fig. 4.4 are found to be in fair agreement. Note that both the data and simulations exhibit the same asymmetry as a function of z about the focal position. This arises from the aberrations discussed above and illustrated in Fig. 4.7. The magnitudes at the peak disagree by $\approx 25\%$. This is likely due to misalignments in the system decreasing the maximum throughput at the focal position. Due to the dramatic field reduction and the extreme sensivity of the lens and collector system, maintaining the alignment of the beam-line for maximum signal is difficult. Daily variations in the superconducting magnet cyrogens and small thermal expansions of the experimental apparatus have the potential to significantly alter the alignment. Other data sets have yielded data in better agreement with the numerical predictions (e.g., compare the $V_L = 5$ kV point in Fig. 4.6 with the maximum percentage transmission in Fig. 4.4).

The focal position as a function of V_L is shown in Fig. 4.5. With the exception of the point at $V_L = 2$ kV, the theoretical predictions are in excellent agreement with the measurements with no fitted parameters. The disagreement at 2 kV is likely due to two things. One is that the small signals and broad focusing region at small V_L create systematic difficulties in determining the position of maximum focus. The other is that for low lens voltages, the particle simulations are very sensitive to incoming beam energy, estimated to be 30.0 eV.

The maximum collector signal as a function of V_L is shown in Fig. 4.6. There is a significant discrepancy between the experimental and simulated data of $\approx 20 - 30\%$. As mentioned above, this could be due to an incorrect estimate of the beam width ρ_b. As a result, the error bars on the theoretical points in Fig. 4.6 represent the potential range of corrrelated vertical shifts of the predicted data points.

To further test the experimental apparatus and model, the aperture diameter was increased to $d \approx 0.48$ cm and ≈ 80 % of the beam was measured to pass through the collector aperture. This agrees well with the numerical prediction from orbit calculations of ≈ 90 % transmission.

4.5   Theoretical description

It is difficult to construct a complete and accurate analytical model of all parts of the experiment described here. However, relatively simple models of important parts of the beam transport and fast extraction processes can be described, and are done so here. They provide further insights into the characteristics of the transported and extracted beam.

4.5.1   Single particle dynamics

Ignoring the relatively small $E \times B$ drift motion in the θ direction, the beam particles undergo cyclotron motion of radius $\rho_{\rm c} \approx 1$ μm in the 4.8 T field while streaming along the magnetic field with a velocity $v_{\rm z}$. As described in Sec. 4.2, the first step in the extraction of a charged particle from the magnetic field is a "slow" $(\gamma < 1)$ transport to 1 mT. During this process, a particle undergoes small-scale gyromotion about its magnetic field line while the guiding-center position increases as $r_f = r_i \sqrt{B_{\rm i}/B_{\rm f}}$ due to magnetic flux conservation. (The subscripts i and f will here and henceforth refer to the initial and final values of a quantity before and after each of the two stages of the extraction process.)

In addition to the radial position of the particle, the perpendicular and parallel energies change as well. Due to the constancy of J [cf., Eq. 4.5],

$$E_{\perp \rm f} = \frac{B_{\rm f}}{B_{\rm i}} E_{\perp \rm i}, \tag{4.6}$$

$$E_{\parallel \rm f} = E_{\parallel \rm i} + E_{\perp \rm i} \left(1 - \frac{B_{\rm f}}{B_{\rm i}} \right), \tag{4.7}$$

where $E_{\parallel}$ and $E_{\perp}$ are the parallel and perpendicular kinetic energies defined in Sec. 4.2, and $E_{\parallel \rm f}$ is obtained from energy conservation.
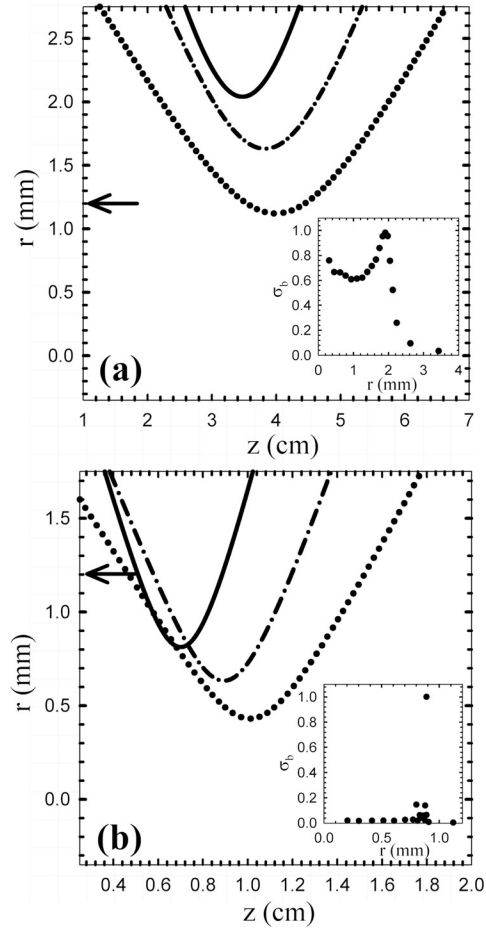
Figure 4.7: Numerically calculated particle trajectories for three different initial radii: 4 ($-$), 3 ($\cdot-\cdot$), and 2 mm ($\cdots$) for (a) $V_L = 2$ kV, and (b) $V_L = 5$ kV. Arrows indicate the radial extent of the aperture used in the experiment. A theoretically calculated beam profile (i.e., $\sigma_b(r)$, in arbitrary units) at the lens focusing position for each case are inset into the figures. Collector effects are not included.

After the first phase of this process, a fast extraction is performed. In this case, the magnetic field in the beam frame changes sufficiently quickly that $\gamma \gg 1$. For an ideal fast extraction, the radius of the particle remains constant as the charged particle is ripped off the field line, hence $r_f = r_i$.

In this cylindrically symmetric case, the canonical angular momentum $P_\theta = rmv_\theta - (e/c)rA_\theta$ is conserved [54], where A_θ is the θ component of the magnetic vector potential. (Here and elsewhere in this paper, CGS units are used and the sign of e is taken to be positive.) Using this relation, the change in v_θ ($\delta v_\theta = v_{\theta f} - v_{\theta i}$) for a fast extraction (i.e., $B \to 0$) is,

$$\delta v_\theta = -\frac{eB}{2cm}r, \tag{4.8}$$

where $r = r_i = r_f$, and B is the initial magnetic field before the rapid decrease to zero. From Eq. 4.8, the parallel and perpendicular energy can be written as,

$$E_{\perp \mathrm{f}} = E_{\perp \mathrm{i}} - v_{\theta i}\frac{eB}{2c}r + \frac{e^2 B^2}{8mc^2}r^2, \tag{4.9}$$

$$E_{\parallel \mathrm{f}} = E_{\parallel \mathrm{i}} + v_{\theta i}\frac{eB}{2c}r - \frac{e^2 B^2}{8mc^2}r^2, \tag{4.10}$$

where $E_{\parallel \mathrm{f}}$ is a result of energy conservation.

4.5.2 Effect of the extraction on the beam distribution function

While the previous section discussed the single particle dynamics during the magnetic extraction process, the beam consists of many particles with a distribution of positions and energies. Discussed here is the effect of the magnetic extraction on these distributions.

The linear scaling of initial and final radii following the slow magnetic field reduction (i.e., $r_f = r_i\sqrt{B_\mathrm{i}/B_\mathrm{f}}$) preserves the shape of the beam profile while rescaling the transverse dimension, namely $\sigma_\mathrm{bf}(r_f) = \sigma_\mathrm{bi}(r_f\sqrt{B_\mathrm{f}/B_\mathrm{i}})$. In the fast extraction, the radial positions of the particles do not change (i.e., $r_f = r_i$) causing the areal density profile to also remain unchanged [i.e., $\sigma_\mathrm{bf}(r) = \sigma_\mathrm{bi}(r)$].

The modifications to the beam energy distribution function are more complicated. The final energy distribution after the transition to low magnetic field $f_f(E_{\|f}, E_{\perp f})$ can be obtained from the initial distribution $f_i(E_{\|i}, E_{\perp i})$ using Eqs. 4.6 and 4.7 to perform the required coordinate transformation. However, in many if not most cases, only knowledge of the mean energy and the rms energy spread is required, namely $(\overline{E}_j \equiv\, < E_j >)$ and $(\Delta E_j \equiv \sqrt{< (E_j -\, < E_j >)^2 >})$, where j indicates the components of the $\|$, $\perp$, and total particle energy. These moments of the distribution can be calculated by averaging the appropriate function from Eqs. 4.6 and 4.7 over the original distribution f_i. This is made possible because $E_{\|f}$ and $E_{\perp f}$ are functions of $E_{\|i}$ and $E_{\perp i}$ (and $v_{\theta i}$) only.

The first moments of f_f after a slow magnetic reduction are,

$$\overline{E}_{\|f} = \overline{E}_{\|i} + \overline{E}_{\perp i}\left(1 - \frac{B_f}{B_i}\right), \tag{4.11}$$

$$\overline{E}_{\perp f} = \overline{E}_{\perp i}\frac{B_f}{B_i}. \tag{4.12}$$

The second moments are,

$$\triangle E_{\|f} = \sqrt{\triangle E_{\|i}^2 + \triangle E_{\perp i}^2 \left(1 - \frac{B_f}{B_i}\right)^2}, \tag{4.13}$$

$$\triangle E_{\perp f} = \triangle E_{\perp i}\frac{B_f}{B_i}. \tag{4.14}$$

Although $\overline{E}_{\|f}$, $\overline{E}_{\perp f}$, $\triangle E_{\|f}$, and $\triangle E_{\perp f}$ change, the total energy $\overline{E}$ and the rms energy spread $\triangle E$ remain constant because the magnetic field does no work. The same is true for the fast magnetic extraction, described below.

Considering now the effect of the fast extraction on the energy distribution, the radial dependence of the beam distribution must be included, since Eqs. 4.9 and 4.10 depend on r. With this in mind, $f_f(E_{\|f}, E_{\perp f}, r_f)$ after the fast extraction can be obtained by another coordinate transformation, this time using Eqs. 4.9 and 4.10. However, this transformation must be performed in velocity space because v_θ appears explicitly in Eqs. 4.9 and 4.10.

Similar to the slow reduction in the field, the moments of f_f after the fast extraction are obtained by averaging functions of the quantities defined in Eqs. 4.9

and 4.10 over the original distribution function $f_i(E_{\|i}, E_{\perp i}, r_i)$. Using $<>_i$ to denote this average (i.e., over $E_{\|i}$, $E_{\perp i}$ and r_i), the first moments of f_f after a fast extraction are,

$$\overline{E}_{\|f} = \left\langle E_{\|i} - \frac{e^2 B^2}{8mc^2} r^2 \right\rangle_i, \tag{4.15}$$

$$\overline{E}_{\perp f} = \left\langle E_{\perp i} + \frac{e^2 B^2}{8mc^2} r^2 \right\rangle_i. \tag{4.16}$$

In Eqs. 4.15 and 4.16, we have used the fact that, for the gyromotion in the perpendicular direction considered here, $< v_{\theta i} >_i = 0$ and $r_i = r_f = r$. The kick δv_θ transfers energy from the parallel to perpendicular direction.

The seconds moments of f_f after a fast extraction are,

$$\triangle E_{\|f} = \left\langle \left(E_{\|i} - v_{\theta i} \frac{eB}{2c} r - \frac{e^2 B^2}{8mc^2} r^2 - \overline{E}_{\|f} \right)^2 \right\rangle_i^{\frac{1}{2}}, \tag{4.17}$$

$$\triangle E_{\perp f} = \left\langle \left(E_{\perp i} + v_{\theta i} \frac{eB}{2c} r + \frac{e^2 B^2}{8mc^2} r^2 - \overline{E}_{\perp f} \right)^2 \right\rangle_i^{\frac{1}{2}}. \tag{4.18}$$

Similar to the transition to low field, although $\overline{E}_\|$, $\overline{E}_\perp$, $\triangle E_\|$, and $\triangle E_\perp$ change, the total energy $\overline{E}$ and the rms energy spread $\triangle E$ remain constant. Now, for a given f_i, we have all the information needed to find either f_f or the first two moments of f_f following the slow reduction in, or fast extraction from, the field.

4.5.3   Results for a Gaussian radial profile and Maxwellian velocity distribution

Moments of the distribution function

Knowledge of the initial beam distribution function is necessary to proceed further. Chapters 2 and 3 described in detail the initial distribution functions for the beams created here. If the beam is initially formed by extraction from a plasma at temperature T and $\xi \leq 1$, the initial beam distribution function can be written as [65],

$$f_i(E_\parallel, E_\perp, r) \approx \frac{2e^{-E_\perp/T}}{T\rho_b^2} f_i(E_\parallel) \exp\left[-\left(\frac{r}{\rho_b}\right)^2\right], \qquad (4.19)$$

where $f_i(E_\parallel)$ is written symbolically for convenience. Procedures for calculating it are described in Ch. 3. Equation 4.19 neglects correlations between r and $E_\parallel$. These correlations are only significant in describing the fast extraction process but are negligible for the beams relevant here where $\xi < 0.5$. Where necessary, the velocity distribution function $f_i(v_z, v_\perp, r)$ can be obtained by a coordinate transformation using the expressions stated earlier.

Following the slow reduction in magnetic field, the linear scaling of the radius of each particle discussed in Sec. 4.5.1 preserves the Gaussian form of Eq. 4.1 leading to a simple expression for the modified beam width,

$$\rho_{bf} = \sqrt{\frac{B_i}{B_f}} \rho_{bi}. \qquad \text{(slow extraction)} \qquad (4.20)$$

For the fast extraction, the radial positions of the particles do not change hence,

$$\rho_{bf} = \rho_{bi}. \qquad \text{(fast extraction)} \qquad (4.21)$$

Considering now the energy distributions, the modifications to f_i after the transition to low field or the fast extraction can be obtained by performing the coordinate transformations described in Sec. 4.5.2 on Eq. 4.19. While this is relatively complicated, much information is contained in the low-order moments of the distributions. In particular, knowledge of only $< r^2 >^{1/2}$, $\overline{E}_{\parallel i}$, $\overline{E}_{\perp i}$, $\triangle E_{\parallel i}$, and $\triangle E_{\perp i}$ is needed to evaluate Eqs. 4.11-4.18. Further, all except the moments of the parallel energy distribution are elementary, namely $< r^2 >^{1/2} = \rho_b$, $\overline{E}_{\perp i} = T$ and $\triangle E_{\perp i} = T$.

The quantities $\overline{E}_{\parallel i}$ and $\triangle E_{\parallel i}$ are more complicated due to plasma space-charge effects (cf., Ch. 3). They have corrections of the order of the temperature T of the trapped plasma that depend upon both the scaled beam amplitude ξ and the scaled electrode radius R_W/λ_D. For the specific case studied in Sec. 4.3 with $\xi = 0.4$ and $R_W/\lambda_D = 500$, $\overline{E}_{\parallel i} \approx |eV_E| + 3.1T$ and $\triangle E_{\parallel i} \approx 2.2T$ (cf., Ch. 3).

For the slow reduction in magnetic field with the assumed beam distribution function in Eq. 4.19, the first moments are obtained by evaluating Eqs. 4.11 and 4.12,

$$\overline{E}_{\|\mathrm{f}} = \overline{E}_{\|\mathrm{i}} + T\left(1 - \frac{B_{\mathrm{f}}}{B_{\mathrm{i}}}\right), \tag{4.22}$$

$$\overline{E}_{\perp\mathrm{f}} = T\frac{B_{\mathrm{f}}}{B_{\mathrm{i}}}. \tag{4.23}$$

The corresponding second moments are obtained by evaluating Eqs. 4.13 and 4.14,

$$\triangle E_{\|f} = \sqrt{\triangle E_{\|i}^2 + T^2\left(1 - \frac{B_{\mathrm{f}}}{B_{\mathrm{i}}}\right)^2}, \tag{4.24}$$

$$\triangle E_{\perp f} = T\frac{B_{\mathrm{f}}}{B_{\mathrm{i}}}. \tag{4.25}$$

Following the fast extraction (i.e., $B \rightarrow 0$), the first moments of f_{f} are obtained by evaluating Eqs. 4.15 and 4.16,

$$\overline{E}_{\|\mathrm{f}} = |eV_{\mathrm{E}}| + \overline{E}_{\|\mathrm{i}} - \frac{e^2 B^2}{8mc^2}\rho_{\mathrm{b}}^2, \tag{4.26}$$

$$\overline{E}_{\perp\mathrm{f}} = T + \frac{e^2 B^2}{8mc^2}\rho_{\mathrm{b}}^2. \tag{4.27}$$

The second moments of f_{f} for this case are similarly found using Eqs. 4.17 and 4.18 along with Eq. 4.19,

$$\triangle E_{\|f} = \sqrt{\triangle E_{\|i} + T\frac{e^2 B^2}{4mc^2}\rho_{\mathrm{b}}^2 + \left(\frac{e^2 B^2}{8mc^2}\right)^2 \rho_{\mathrm{b}}^4}, \tag{4.28}$$

$$\triangle E_{\perp f} = \sqrt{T^2 + T\frac{e^2 B^2}{4mc^2}\rho_{\mathrm{b}}^2 + \left(\frac{e^2 B^2}{8mc^2}\right)^2 \rho_{\mathrm{b}}^4}, \tag{4.29}$$

Here we have used the fact that, for the gyromotion in the perpendicular direction considered here, $< v_{\theta i}^2 >_i = T/2m$ and $< v_{\theta i} >_i = 0$. Note that Eqs. 4.26-4.29 refer to a fast extraction of the initial beams created here (i.e., that given by Eq. 4.19). They assume that no slow reduction of the initial beam has occurred.

Measure of beam quality

Once a fast extraction is performed, the beam is "electrostatic". A key measure of the quality of such a beam is the invariant emittance ϵ. To within constants of proportionality, it is defined as the product of the rms spread in radius times the rms spread in perpendicular velocities (or equivalently momenta) of the beam [54],

$$\epsilon = \sqrt{\left(\overline{r^2}\right)\left(\overline{E}_\perp\right)}. \tag{4.30}$$

In the case considered here, where the beam particles are initially in a region of non-zero magnetic field, the conservation of the canonical angular momentum results in a large increase in perpendicular velocities when the beam is extracted from the field. In this case, the relevant quantity is the so-called *generalized invariant emittance*, ϵ^*. For the Gaussian radial profile and Maxwellian velocity distributions considered here, the value of $\overline{E}_\perp$ from Eq. 4.27 can be inserted into Eq. 4.30 to obtain,

$$\epsilon^* = \rho_{\rm b}\sqrt{T + \frac{e^2 B^2}{8mc^2}\rho_{\rm b}^2}. \tag{4.31}$$

Note that this equation is only valid for a cylindrically symmetric case and the assumed Gaussian radial profile. A non-cylindrically symmetric system (e.g., extraction through a high-permeability grid or radial spoke arrangement) would lead to different results.

This quantity is invariant throughout the entire magnetic extraction process and reduces to the standard emittance ϵ once the beam is in the field free region. That ϵ^* is conserved during the first magnetic reduction can quickly be seen by inserting $\rho_{\rm bf} = \rho_{\rm bi}\sqrt{B_{\rm i}/B_{\rm f}}$, and $T_f = T_i(B_{\rm f}/B_{\rm i})$ into Eq. 4.31, then noting the invariance.

While we do not find the expression of Eq. 4.31 for ϵ^* in the literature, it can be compared with [32],

$$\epsilon \approx \rho_{\rm b}\sqrt{T} + \rho_{\rm b}\sqrt{\frac{e^2 B^2}{8mc^2}\rho_{\rm b}^2}, \tag{4.32}$$

which was developed as an approximate expression for the fast extraction of a thermal beam from a field of strength B. The formulas are in good agreement when $T \gg e^2 B^2 \rho_\mathrm{b}^2/(8mc^2)$ or $T \ll e^2 B^2 \rho_\mathrm{b}^2/(8mc^2)$, but otherwise disagree.

Equation 4.31 is valid at all points during the magnetic extraction process. Thus, for the beam creation and the two-stage extraction process considered here, the emittance of the electrostatic beam is set by Eq. 4.31 at the point where the beam is initially created (i.e., in the 4.8 T field).

Equation 4.31 can also be written in the physically insightful form,

$$\epsilon^* = \rho_\mathrm{b}\sqrt{T}\left(1 + \left(\frac{\rho_\mathrm{b}}{2\rho_\mathrm{c}}\right)^2\right)^{1/2}, \tag{4.33}$$

where ρ_c is the cyclotron radius, $\rho_\mathrm{c} = \sqrt{2T/m}/(eB/mc)$. By definition, for a beam in a magnetic field, $\rho_\mathrm{b} \gg \rho_\mathrm{c}$. Thus for a given T, ϵ^* is always significantly larger if the beam is born in a magnetic field. In a magnetic field of any strength, where the terms T and $e^2 B^2/8mc^2 \rho_\mathrm{b}^2$ appear as above [c.f., Eq. 4.31], the latter term is dominant unless $\rho_\mathrm{b} \approx \rho_\mathrm{c}$ (i.e., the case of a weakly magnetized beam).

One of the utilities of the emittance is that it is conserved during an electrostatic focusing process. Thus it can be used to estimate the average perpendicular beam energy $\overline{E}_\perp$ at the focal point. If a beam is focused in transverse width from ρ_bi to ρ_bf, the average perpendicular energy will change as,

$$\overline{E}_{\perp\mathrm{f}} = \overline{E}_{\perp\mathrm{i}}\left(\frac{\rho_\mathrm{bi}}{\rho_\mathrm{bf}}\right)^2. \tag{4.34}$$

4.6   Summary and conclusion

In Chs. 2 and 3, we developed a technique to create high quality positron beams in a 4.8 T magnetic field by pulsed extraction from a Penning-Malmberg trap. It was demonstrated that one can use the tools available in such a UHV high-field trap, namely rotating-wall radial plasma compression and cyclotron cooling, to tailor plasmas and improve beam quality. This chapter expands on that work and describes a procedure to extract these beams from the confining magnetic field to

create a class of electrostatic beams. The beams were then focused electrostatically to smaller transverse dimensions.

Table 4.1 summarizes the beam parameters during the magnetic extraction and electrostatic focusing processes for $V_L = 6$ kV, the lens voltage for which maximum focusing was achieved. Values in the first stage are those measured in the 4.8 T field. Values in the next two stages are obtained using Eqs. 4.20, 4.21, and 4.22-4.29 along with energy conservation. Values in the final stage are from measurements, and the conservation of ϵ^* in Eq. 4.31. The value for Δr in the final stage (IV) is an upper bound for the ≈ 55 % of the beam that makes it through the aperture. The values for T are found from the relation $T = \overline{E}_{\perp i}$. In the focusing region, the electrical potential is found to be constant as a function of r, causing $\triangle E$ to remain unchanged from the value in Stage I.

Considering the values in Tab. 4.1, the fact that the initial value of $\triangle E_{\parallel}$ is a factor of two larger than the plasma temperature is because ξ is not close to zero (i.e., $\xi = 0.4$). Working at smaller values of ξ would bring $\triangle E_{\parallel}$ closer to T. The increase in ρ_b during the slow extraction contrasts the relatively small increases in $\triangle E_{\parallel}$, and large decrease in $\triangle E_{\perp}$. Similarly, during the fast extraction (Stage III), Δr remains constant but $\triangle E_{\parallel}$ and $\triangle E_{\perp}$ increase significantly as a result of the δv_{θ} kick that the particles experience when exiting the field. Beneficially, during the entire magnetic extraction and electrostatic focusing processes, $\triangle E$ remains constant. Finally, the large increase in $\overline{E}_{\perp}$ that occurs at the focus of the Einzel lens is a result of the conservation of the beam emittance ϵ.

At the present stage of development, the beam emittance is not significantly greater than that obtained by taking a beam directly from a buffer-gas positron accumulator (i.e., such as that which would be used to fill the HF trap described here). However, the transverse beam width, and hence the beam emittance, is set by the Debye length of the parent plasma in the high magnetic field. Colder, higher density plasmas could be used to produce higher quality beams. Thus, the ability to create cryogenic plasmas and potential improvements in RW compression can be expected to create significantly better beams.

Considering applications to positron scattering, the present electrostatic

Table 4.1: Beam parameters for a slow reduction from a 5 T field (I), to a 1 mT field (II), followed by a fast extraction to zero field (III), and finally focus with an Einzel lens (IV), of the beam in Fig. 4.3. $V_\mathrm{L} = 6$ kV and the invariant beam emittance ϵ^* is 0.3 cm-$\sqrt{\mathrm{eV}}$. In stages I, II, and III, the beam is Gaussian and $\Delta r = \rho_\mathrm{b}$. See text for further details.

Stage	I	II	III	IV
B (G)	4.8×10^4	10	0	0
$\Delta E_\parallel$ (eV)	0.22	0.26	0.51	–
$\Delta E_\perp$ (eV)	0.1	2.1×10^{-5}	0.45	–
ΔE (eV)	0.24	0.24	0.24	0.24
$\overline{E}_\perp$ (eV)	0.1	2.1×10^{-5}	0.45	6
Δr (cm)	6.5×10^{-3}	0.45	0.45	< 0.12

beams would be quite useful. The total energy spread of the beam is set by the parent-plasma temperature and is preserved in the extraction process. For a single particle, any change in $E_\perp$ is accompanied by an equal and opposite change in $E_\parallel$ to conserve energy; this effect keeps $\triangle E$ constant at all times during the magnetic extraction process. Thus, the electrostatic beams created in this manner could be used in energy-spectroscopy experiments that benefit from small energy spreads. Plasmas with temperatures < 20 meV have been achieved using electrodes cooled to ≈ 80 K, allowing for beams with $\triangle E < 30$ meV. These beams could be quite useful without further HF-trap improvements.

A high-permeability grid or spoke arrangement [57, 22] could be used to significantly reduce the effect of the fast extraction on the particles without changing the initial magnetic field from which the beam is (fast) extracted. In essence, this would reduce the kick received by the particles upon fast extraction, thereby producing electrostatic beams with even lower emittance values.

Finally, using the procedures described here, remoderation techniques could also be used to advantage to further reduce the beam emittance. However in this case, the energy spread will be set by the characteristics of the (re)moderator and the number of beam particles will be reduced.

Chapter 5

Rotating wall compression in two tesla magnetic fields

5.1 Background

In a paradigm shift, this short final chapter documents a brief study of rotating wall (RW) radial plasma compression in relatively low magnetic fields ($B = 2.0$ T). While this study is far from complete, it documents a regime in which RW compression becomes significantly limited when compared to the more ideal behavior observed at higher magnetic fields (e.g., $3 \leq B \leq 4.8$ T). As mentioned in Ch. 1, the RW is a valuable tool for two reasons: it enables fine tuning of the trapped plasma density, and it allows for indefinite confinement times (e.g., $\tau \sim$ days) by counteracting natural expansion of the plasma due to small trap asymmetries. Unfortunately, the RW acts to significantly heat the plasma, particular when it is initially turned on [14]. If adequately strong cyclotron cooling is not present, the plasma will heat to sufficiently high temperatures such that the background neutral gas becomes ionized. Then, freshly created ions cause an ion instability that destroys confinement [35]. At $B = 5$ T ($\tau_{\mathrm{c}} = 0.16$ sec), we have successfully used the RW to compress plasmas to high densities ($n > 2 \times 10^{10}$ cm^{-3}) using large RW frequencies $f_{\mathrm{RW}} > 6$ MHz while maintaining cold plasmas (i.e., $T < 0.1$ eV) [12, 13, 14]. We here report a recent effort to operate the RW in

lower fields, where cyclotron cooling is diminished.

5.2   Results

For operation of the RW in this experiment, see Sec. 1.3 or Ref. [13]. Although a continuum of field strengths $0 < B < 5$ T are accessible on this experiment, we focus here on $B = 2$ T only. We choose this field because it appears to be the onset of significant RW compression limitations, and it has been well documented that the RW works well in larger fields [30, 13].

Figure 5.1 summarizes the results for RW compression in a 2 Tesla field ($\tau_c = 1.0$ sec). Here, the plasma parameters are $L_p \approx 10$ cm and $N \approx 4 \times 10^8$. Two modes of RW operation are plotted: a fast-ramp mode where the RW voltage V_{RW} is quickly ($\Delta t < 10$ μsec) ramped from 0 to 1.2 V, and a slow-ramp mode where V_{RW} is slowly ($\Delta t \approx 1$ sec) ramped from 0 to 1.2 V. After either the slow-ramp or fast-ramp mode, the RW is then left on until the plasma reaches a steady state. Here, this time is ≈ 20 sec. For the fast-ramp mode of operation, the plasma was only able to be compressed up to $n = 3 \times 10^9$ cm^{-3} without inducing any plasma instabilities from ionization of the background gas. For the slow-ramp mode, the plasma was able to be compressed to $n = 4 \times 10^9$ cm^{-3}. As discussed below, this difference in steady-state density is possibly related to the fact that for the slow-ramp mode, the plasma cools to lower temperatures once in steady-state.

In normal operation, the plasma spins up to approximately the applied frequency $f_E = f_{RW}$. Here, this is seen until $f_{RW} = 2$ MHz, at which point noticeable "slip" appears, or a difference between the applied wall and plasma rotation frequency $f_{RW} - f_E$. This is illustrated in Fig. 5.1, where the theoretically achievable plasma density when $f_{RW} = f_E$ is plotted. As mentioned above, at roughly $f_{RW} = 2$ MHz, slip begins to appear. In the slow-ramp mode of operation, the slip appears only above $f_{RW} = 2.5$ MHz. This may have some relation to the increased heating observed and described below.

Also plotted in Fig. 5.1 is the plasma temperature as a function of f_{RW}. Notice that the plasma temperature increases approximately linearly with f_{RW}.

Table 5.1: The numerical values of Fig. 5.4

B(G)	1	1.5	2	2.5	3
τ_c theory (sec)	0.44	0.64	1.0	1.77	3.98
τ_c data (sec)	0.45	0.56	0.6	1.11	4.78

This contrasts the behavior seen at 5 T, where the temperature has been shown to remain low (i.e., $T \sim 0.1$ eV) and constant as a function of f_{RW} [14]. For the slow-ramp mode, the plasma reaches lower temperatures when it achieves a steady state. A detailed explanation of this behavior requires further investigations that will not be performed here.

For completeness, examples of the plasma profiles from Fig. 5.1 are plotted in Fig. 5.2 for both the slow and fast modes of RW operation. Additionally, to illustrate the expansion of the plasma, Fig. 5.3 shows the time evolution of the plasma profiles after the RW has been turned off.

As mentioned above, when $B \leq 2$ T, the RW becomes exceedingly difficult to operate. For $B = 1$ T, even in a slow ramped mode of operation, compression only occurs for $f_{RW} < 0.25$ MHz. For $f_{RW} > 0.25$ MHz, the plasma becomes unstable.

On a different note, the measured cyclotron cooling times at magnetic fields ≥ 3 T agree well with the theoretical cooling rate. However at lower fields, the rates depart significantly from the theoretical predictions. Figure 5.4 and Table 5.1 summarize these results. For $B = 2$ and 1.5 T, measured values of τ_c depart significantly from those predicted by theory. At $B = 1$ T, measured values of τ_c appear to return to the expected value. Presently, the reasons for this discrepancy is unclear. Further work is needed to resolve this problem.

For completeness, an example of a data set used to extract a plasma cooling time τ_c is shown in Fig. 5.5. Here, the plasma temperature after RW compression is recorded for a series of times waited after turning the RW off. Just as in Fig. 5.3, the RW is applied until the plasma achieves a steady-state, then turned off. An exponential is then fit to data to extract a 1/e falling time of the plasma temperature, or τ_c.
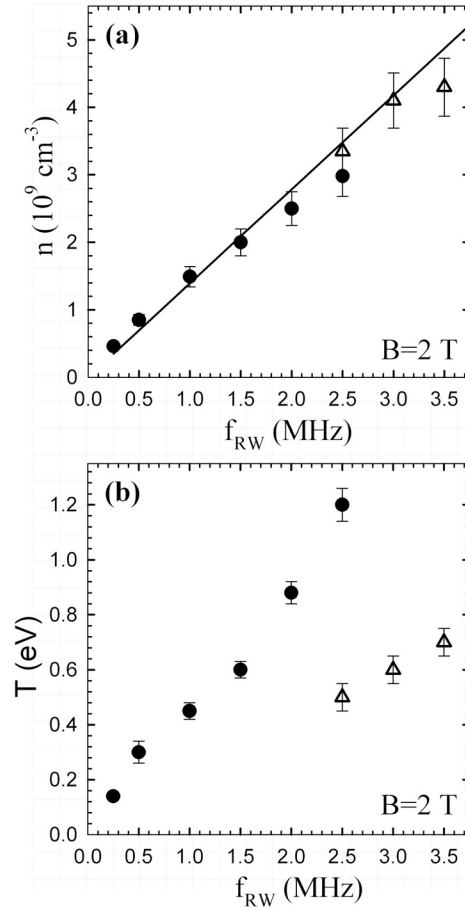
Figure 5.1: (a) the RW frequency f_{RW} vs. the plasma density after application of the RW for ≈ 20 sec. Data are plotted for both a fast-ramp (•) and a slow-ramp ($\triangle$) mode of RW operation. Theoretical predictions for $f_{RW} = f_E$ are also plotted (—). (b) The temperature of the plasma immediately after a steady state is achieved with RW application. See text for details.
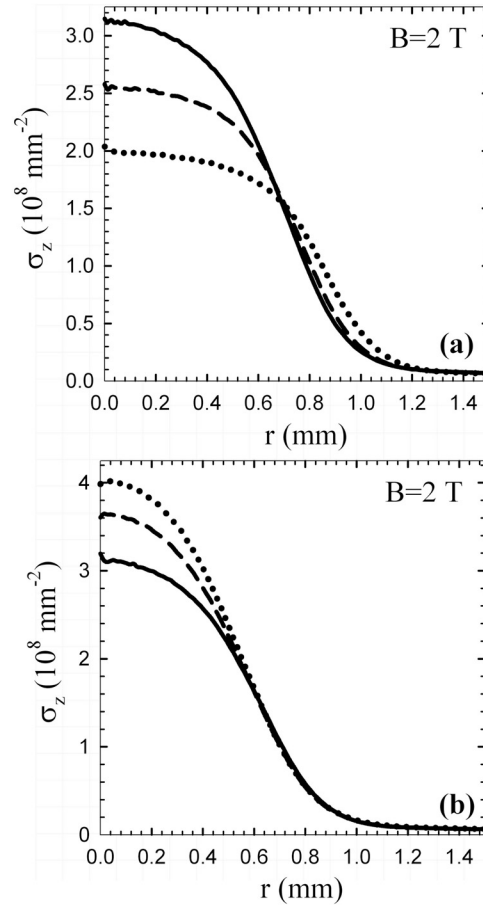
Figure 5.2: Plasma profiles from Fig. 5.1 plotted for (a) fast-ramp RW operation at $f_{RW} = 1.5$ ($\cdots$), 2 (- - -), and 2.5 MHz (—); and (b) slow-ramp RW operation at $f_{RW} = 2.5$ (—), 3 (- - -), and 3.5 ($\cdots$). For the 3 plasmas in (a), $\lambda_D \approx 0.14$ mm, while for the 3 plasmas in (b), $\lambda_D \approx 0.09$ mm.
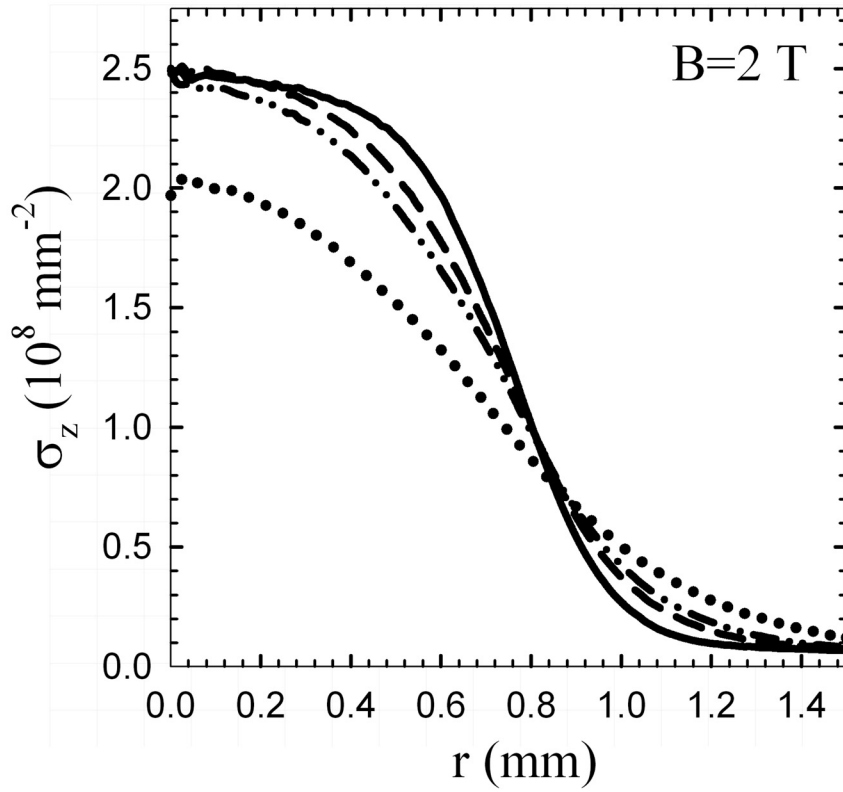
Figure 5.3: Time evolution of the plasma profile plotted after the RW was applied, a steady state reached, then the RW turned off and times waited of 0 (—), 0.5 (- - -), 1 (- ··) and 5 seconds (···). Here, the RW is operated in fast-ramp mode, and $f_{\mathrm{RW}} = 2$ MHz.
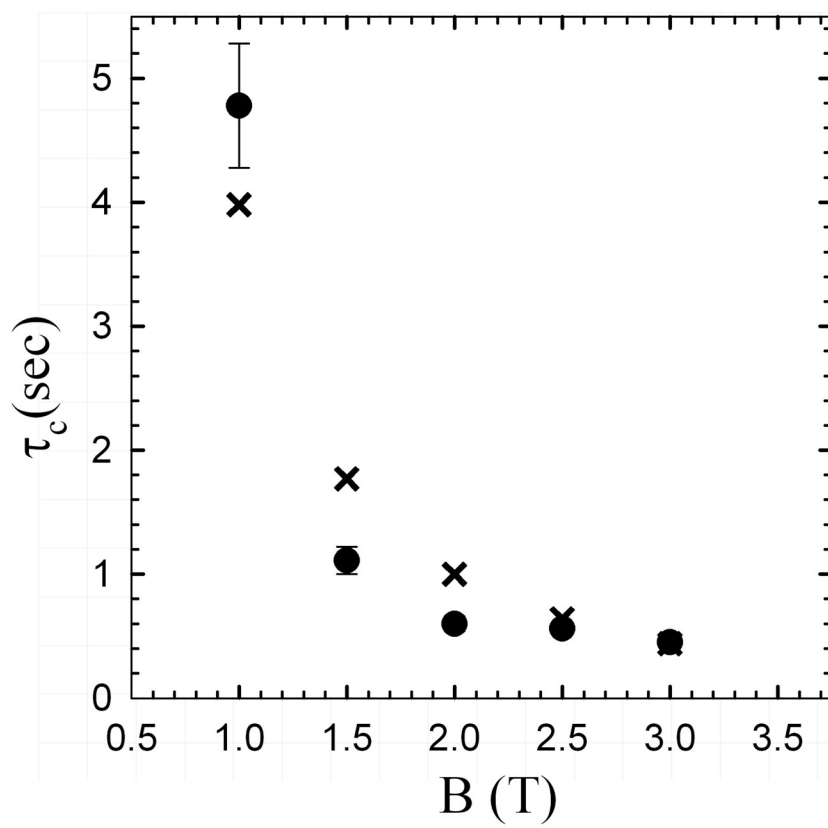
Figure 5.4: The measured cyclotron cooling times τ_c of the plasma ($\bullet$) vs. the predicted values (cross).
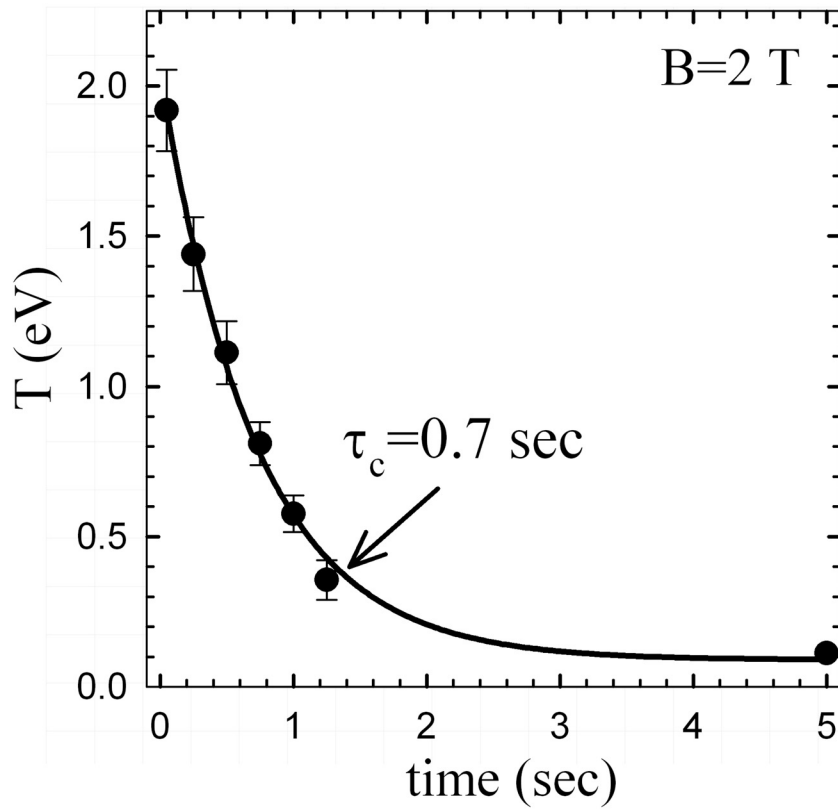
Figure 5.5: An example of data used to extract a plasma cooling time $\tau_{\rm c}$. The plasma temperature T is plotted vs. the wait time after RW application (•). The exponential fit used to determine $\tau_{\rm c} = 0.7$ sec is included (—).

5.3   Summary

We have shown that the RW can be used at magnetic fields as low as $B = 1$ T. However, for significant compressions to densities $n > 1 \times 10^9$, a field of $B \geq 2$ T is required. Further, slowly ramping up the RW voltage V_{RW} permits higher compression by avoiding ion instabilities and achieving lower temperatures in steady-state. As mentioned above, the results presented here for $B = 2$ T are far from complete. More systematic studies are warranted to explore the limits of RW plasma compression in low magnetic fields along with the anomalous plasma cooling times that are observed.

Chapter 6

Summary and concluding remarks

There are numerous exciting antimatter applications, but many are fundamentally limited by the antimatter source [2, 52, 45]. A lack of readily available, bright positron sources has seriously hindered the development of positron applications and, in turn, the understanding of many aspects of positron physics. Fortunately, advances in charge particle trapping allow for the creation of bright, effective sources by accumulating large numbers of positrons in a electromagnetic trap [59]. Specifically, recent advances in Penning-Malmberg traps (PMT) allow for the confinement of large numbers of positrons ($\sim 10^{10}$) for long periods of time ($\tau \sim$ days) [59]. With this new technology comes the challenge of creating high quality beams from the trapped particles. For many applications, a large number of trapped positrons is not sufficient: bright and cold positron beams are required. For example, the creation of Bose-Einstein condensed positronium would require a bright, narrow and cold beam to achieve sufficient densities of cold positrons for positronium formation and condensation [45]. Positron atomic physics applications require cold positron beams to obtain good energy resolution of positron-atom collisions [3]. Finally, for a positron microscope, a narrow beam is necessary to obtain good spatial resolution, for example, of a material surface [15]. For all these applications, the properties of a beam created from a trapped particle population is critical. Adding to this demand is the desire to create beams in a nondestructive and reproducible manner so as to efficiently use all of the trapped particles. This is extremely important because of the potentially long trap times ($\sim$ hours) required

to load a high capacity trap from, say, a typical moderated radioactive positron source.

This thesis has successfully demonstrated a procedure to create high quality, tailored beams from electrons in a PMT that satisfy all of the above demands. Beams are extracted in an approximately 100 % efficient manner with narrow transverse widths (e.g., $\rho_{\rm b} < 20~\mu$m), small energy spreads (e.g., $\triangle E \leq 30$ meV), and high reproducibility (e.g., $\Delta N_b/N_b \leq 5$ %). A solid physical understanding of the beam extraction physics was demonstrated by using a simple model to derive analytic expressions for the beam number $N_{\rm b}$, transverse spatial profile $\sigma_{\rm b}(r)$, and complete energy distribution function $f(E_\parallel, E_\perp)$. The transverse spatial width of the beams was shown to be set by the Debye length of the parent plasma, namely $\rho_{\rm b} = 2\lambda_{\rm D}\sqrt{1+\xi}$. For small ξ, the beam width is $\approx 2\lambda_{\rm D}$, while for larger ξ, the beam width increases. The radial distribution of the beam is Gaussian for all beams with $\xi < 1$. The energy distribution function, when scaled to the plasma temperature, was shown to depend only on ξ and $R_{\rm W}/\lambda_{\rm D}$. For small ξ, the beam energy spread $\triangle E$ is approximately the temperature of the parent plasma T. For larger ξ, the energy spread increases, but only by moderate amounts. The larger $R_{\rm W}/\lambda_{\rm D}$, the faster $\triangle E$ increases with ξ. The main take home message here is that for $\xi < 0.5$, beams are small (i.e., $\rho_{\rm b} \approx 2\lambda_{\rm D}$) and cold (i.e., $\triangle E < 2.5T$). It is possible to obtain beams of $\xi < 0.5$ by either limiting the total number of escaping particles $N_{\rm b}$, or increasing the plasma length $L_{\rm p}$.

Although these beams are created in a large magnetic field, it was successfully demonstrated that electrostatic beams (beams in a magnetic field-free region) can be created using this technique along with a slow reduction in, then fast extraction from, the confining magnetic field. Further detailed analysis was presented deriving properties of the electrostatic beams including the transverse spatial profile, energy distribution function, and invariant emittance. Electrostatic beams were then focused to smaller transverse dimensions while conserving the initial energy spread $\triangle E$ of the beam in the high magnetic field. Although this magnetic extraction process results in a large beam emittance increase, the total energy spread $\triangle E$ remains constant, and equal to that at the time of initial

creation. Further, by using smaller initial beams, the emittance increase can be minimized.

At this point, the trapped based positron beams described here offer immediate improvements for current positron applications. However, there is still potential for much improvement in both trapping and beam-creation techniques to significantly improve beam quality. The most promising possibility is that of creating cryogenic positron plasmas. Such cold plasmas would allow for dramatically narrower ($\rho_b < 5\ \mu$m) and colder ($\triangle E \approx 10$ K) beams. Previously, cryogenic nonneutral plasmas have been achieved by submerging a PMT in a dewar of liquid helium [5]. Unfortunately, submerging a trap in liquid helium is not compatible with the demands of many positron applications. However, this difficulty can be overcome by simply cooling the trap electrodes to cryogenic temperatures, approximating the conditions of a submerged trap.

While the apparatus used here has this capacity, problems with the cryogenic system have prevented cooling the electrodes below 80 K. Further, due to difficulties measuring low plasma temperatures, only an upper bound has been placed on the plasma temperature of $T \leq 200$ K. Results of beam extraction experiments further suggest that the plasma is no colder then 200 K. This implies that external heating sources in the trap overcome cyclotron cooling at 200 K. Possible external heating sources are small trap asymmetries, plasma expansion heating, or room temperature black body radiation entering from the ends of the trap. In the future, if cryogenic positron plasmas are to be achieved for the purpose of trap-based positron beams, these external heating sources must be addressed. One possibility may be to trap the beam in neighboring trap electrodes immediately after is is formed. This would eliminate plasma expansion heating, and other effects related to the large plasma potential, allowing the beam to cool to lower temperatures in perhaps a more quiescent state. Additionally, it may turn out that RW compression is more effective on a small beam close to the plasma limit (i.e., $\lambda_D \approx R_p$). In this case, further RW compression could be achieved on the trapped beam.

Another way to increase beam quality is by pushing the limits of RW com-

pression. This will both further decrease the width of the beam by decreasing the Debye length of the parent plasma, and increase beam brightness. On this experiment, RW compression is currently limited to roughly $f_{\text{RW}} \approx 6 - 8$ MHz. There are two possible reasons for this limit. First, an imbalance in the 4 electrode sectors and their corresponding circuits may lead to small phase shifts that limit RW compression at high frequencies. Secondly, the capacitive load of an RW sector on the end of the transmission line may significantly attenuate the RW signal on the sectors at high frequencies. This would further limit RW compression at high frequencies. In order to compress plasmas at RW frequencies > 8 MHz, a methodical investigation must be made of the two above effects in order to pin down the source of the current RW limitation.

Both of the above techniques would improve the electrostatic beams created here, as the invariant beam emittance decreases with decreasing ρ_{b}. In addition to this, in the case of electrostatic beams, there is also the possibility of extracting the beam through a magnetic grid or spoke arrangement [22]. Such a magnetic extraction would decrease the perpendicular kick experienced by the beam particles as they exit the magnetic field. This could dramatically decrease the final beam emittance of the electrostatic beams.

This work suggests that trapped based positron sources have an exciting potential role in future antimatter research. With further improvements in trapping tools, there is the potential for cryogenic positron beams with small energy spreads (e.g., $\triangle E \leq 10$ K), and small transverse spatial extents (e.g., $\rho_{\text{b}} \leq 5$ μm) [59]. Even with current trapping technology, trapped based positron beams appear to be of considerable worth to the future of positron applications.

Bibliography

[1] N. Alberola, T. Anthonioz, A. Badertscher, A. S. Belov C. Bas and, P. Crivelli, S. N. Gninenko, N. A. Golubev, M. M. Kirsanov, A. Rubbia, and D. Sillou. Development of a high-efficiency pulsed slow positron beam for measurements with orthopositronium in vacuum. *Nuclear Instruments and Methods in Physics Research Section A*, 560(2):224–232, 2006.

[2] M. Amoretti, C. Amsler, G. Bonomi, A. Bouchta, P. Bowe, C. Carraro, C. L. Cesar, M. Charlton, M. J. T. Collier, M. Doser, V. Filippini, K. S. Fine, A. Fontana, M. C. Fujiwara, R. Funakoshi, P. Genova, J. S. Hangst, R. S. Hayano, M. H. Holzscheiter, L. V. Jorgensen, V. Lagomarsino, R. Landua, D. Lindelof, E. Lodi Rizzini, M. Macri, N. Madsen, G. Manuzio, M. Marchesotti, P. Montagna, H. Pruys, C. Regenfus, P. Riedler, J. Rochet, A. Rotondi, G. Rouleau, G. Testera, A. Variola, T. L. Watson, and D. P. van der Werf. Production and detection of cold antihydrogen atom. *Nature*, 419:456–459, 2002.

[3] L. D. Barnes, J. A. Young, and C. M. Surko. Energy-resolved positron annihilation rates for molecules. *Physical Review A*, 74:012706–1–012706–10, 2006.

[4] B. R. Beck. *Measurement of the magnetic and temperature dependence of the electron-electron anisotropic temperature relaxation rate*. PhD thesis, University of California, San Diego, San Diego, 1990.

[5] B. R. Beck, J. Fajans, and J. H. Malmberg. Temperature and anisotropic-temperature relaxation measurements in cold, pure-electron plasmas. *Physics of Plasmas*, 3(4):1250–1258, 1996.

[6] J. H. Billen and L. M. Young. Poisson/superfish on pc compatibles. *Proceedings of the 1993 Particle Accelator Conference*, page 193, 1993.

[7] R. Bluhm, A. Kostelecky, and N. Russell. Cpt and lorentz tests in hydrogen and antihydrogen. *Physical Review Letters*, 82(11):2254–2257, 1999.

[8] K. F. Canter, A. P. Mills Jr., and S. Berko. Observations of positronium lyman-alpha radiation. *Physical Review Letters*, 34(4):177–180, 1975.

[9] D. B. Cassidy, S. H. M. Deng, H. K. M. Tanaka, and A. P. Mills Jr. Single shot positron annihilation lifetime spectroscopy. *Applied Physics Letters*, 88(19):194105–1–194105–3, 2006.

[10] D. M. Chen, S. Berko, K. F. Canter, K. G. Lynn, A. P. Mills Jr., L. O. Roellig, P. Sferlazzo, M. Weinert, and R. N. West. Angle-resolved positronium emission spectroscopy. *Physical Review Letters*, 58(9):921–924, 1987.

[11] W. S. Crane and A. P. Mills. Subnanosecond bunching of a positron beam. *Review of Scientific Instruments*, 56(9):1723, 1985.

[12] J. R. Danielson and C. M. Surko. Torque-balanced high-density steady states of single-component plasmas. *Physical Review Letters*, 94:035001–1–035001–4, 2005.

[13] J. R. Danielson and C. M. Surko. Radial compression and torque-balanced steady states of single-component plasmas in penning-malmberg traps. *Physics of Plasmas*, 13:055706–1–055706–10, 2006.

[14] J. R. Danielson, C. M. Surko, and T. M. O'Neil. High-density fixed point for radially compressed single-component plasmas. *Physical Review Letters*, 99:135005–1–135005–4, 2007.

[15] A. David, G. Kogel, P. Sperr, and W. Triftshauser. Lifetime measurements with a scanning positron microscope. *Physical Review Letters*, 87(6):067402–1–067402–4, 2001.

[16] C. F. Driscoll. Observation of an unstable l=1 diocotron mode on a hollow electron column. *Physical Review Letters*, 64(4):645–648, 1990.

[17] D. H. E. Dubin and T. M. O'Neil. Trapped nonneutral plasmas, liquids, and crystals (the thermal equilibrium states). *Review of Modern Physics*, 71(1):87–171, 1999.

[18] D. L. Eggleston, C. F. Driscoll, B. R. Beck, A. W. Hyatt, and J. H. Malmberg. Parallel energy analyzer for pure electron plasmas devices. *Physics of Fluids B*, 4(10):3432–3439, 1992.

[19] A. Enomoto, I. Sato, A. Asami, G. Horikoshi, and J. Tanaka. Focusing system of the kek positron generator. *Nuclear Instruments and Methods in Physics Research Section A: Accelerators, Spectrometers, Detectors and Associated Equipment*, 281(1):1–9, 1995.

[20] K. Fallstrom and T. Laine. Construction of the helsinki university of technology (hut) pulsed positron beam. *Applied Surface Science*, 149(1–4):44–48, 1999.

[21] G. Gabrielse, N. S. Bowden, P. Oxley, A. Speck, C. H. Storry, J. N. Tan, M. Wessels, D. Grzonka, W. Oelert, G. Schepers, T. Sefzick, J. Walz, H. Pittner, T. W. Hansch, and E. A. Hessels. Background-free observation of cold antihydrogen with field-ionization analysis of its states. *Physical Review Letters*, 89(21):213401–1–213401–4, 2006.

[22] D. Gerola, W. B. Waeber, M. Shi, and S. J. Wang. Quasidivergency-free extraction of a slow positron beam from high magnetic fields. *Review of Scientific Instruments*, 66(7):3819–3825, 1995.

[23] S. J. Gilbert, C. Kurz, R. G. Greaves, and C. M. Surko. Creation of a monoenergetic pulsed positron beam. *Applied Physics Letters*, 70(15):1944–1946, 1997.

[24] R. G. Greaves, S. J. Gilbert, and C. M. Surko. Trap-based positron beams. *Applied Surface Science*, 194(1–4):56–60, 2002.

[25] R. G. Greaves and C. M. Surko. Antimatter plasmas and antihydrogen. *Physics of Plasmas*, 4:1528–1543, 1997.

[26] A. G. Hathaway, M. Skalsey, W. E. Frieze, R. S. Vallery, D. W. Gidley, A. I. Hawari, and J. Xu. Implementation of a prototype slow positron beam at the nc state university pulstar reactor. *Nuclear Instruments and Methods in Physics Research Section A: Accelerators, Spectrometers, Detectors and Associated Equipment*, 579(1):538–541, 2007.

[27] P. Hautojarvi, A. Vehanen, and V. S. Mikhalenkov. Recovery of deformed iron studied by positrons. *Applied Physics A: Materials Science and Processing*, 11(2):191–192, 1976.

[28] M. Hirose, M. Washio, and K. Takahasi. Production of an intense slow positron eam using a compact cyclotron. *Applied Surface Science*, 85(2):111–117, 1995.

[29] P. Hommelhoff, Y. Sortais, A. Aghajani-Talesh, and M. A. Kasevich. Field emission tip as a nanometer source of free electron femtosecond pulses. *Physical Review Letters*, 96(7):077401–1–077401–4, 2006.

[30] X. P. Huang, F. Anderegg, E. M. Hollmann, C. F. Driscoll, and T. M. ONeil. Steady-state confinement of non-neutral plasmas by rotating electric fields. *Physical Review Letters*, 78(5):875–878, 1997.

[31] C. Hugenschmidt, G. Kogel, R. Repper, K. Schreckenbach, P. Sperr, B. Straber, , and W. Triftshauser. The neutron induced positron source at munich nepomuc. *Nuclear Instruments and Methods in Physics Research Section B: Beam Interactions with Materials and Atoms*, 221:160–164, 2004.

[32] V. W. Hughes, R. L. Long, M. S. Lubel, M. Posner, and W. Raith. Polarized electrons from photoionization of polarized alkali atoms. *Physical Review A*, 5(1):195–222, 1972.

[33] K. Iwata. *Positron anihilation on atoms and molecules*. PhD thesis, University of California, San Diego, San Diego, 1997.

[34] A. P. Mills Jr., S. Berko, and K. F. Canter. Fine-structure measurement in the first excited state of positronium. *Physical Review Letters*, 34(25):1541–1544, 1975.

[35] A. A. Kabantsev and C. F. Driscoll. Fast measurement of picoamp plasma flows using trapped electron clouds. *Review of Scientific Instruments*, 75(10):3628–3630, 2004.

[36] W. E. Kauppila and T. S. Stein. Comparisons of positron and electron scattering by gases. *Advances in Atomic, Molecular, and Optical Physics*, 26:1, 1990.

[37] R. Khatri, M. Charlton, P. Sferlazzo, K. G. Lynn, A. P. Mills, and L. O. Roellig. Improvement of rare-gas solid moderators by using conical geometry. *Applied Physics Letters*, 57(22):2374–2376, 1990.

[38] Y. Kobayashi, I. Kojima, S. Hishita, T. Suzuki, E. Asari, and M. Kitajima. Damage-depth profiling of an ion-irradiated polymer by monoenergetic positron beams. *Physical Review B*, 52(2):823–828, 1995.

[39] C. Kurz, S. J. Gilbert, R. G. Greaves, and C. M. Surko. New source of ultra-cold positron and electron beams. *Nuclear Instruments and Methods in Physics Research Section B: Beam Interactions with Materials and Atoms*, 143:188–194, 1998.

[40] K. G. Lynn, W. E. Frieze, and P. J. Schultz. Measurement of the positron surface-state lifetime for al. *Physics Review Letters*, 52(13):1137–114, 1984.

[41] J. P. Marler and C. M. Surko. Ionization and positronium formation in noble gases. *Physical Review A*, 71(2):022701–1– 022701–10, 2005.

[42] A. P. Mills. Time bunching of slow positrons for annihilation lifetime and pulsed laser photon absorption experiments. *Applied Physics A: Materials Science and Processing*, 22(3):273–276, 1980.

[43] A. P. Mills. Surface analysis and atomic physics with slow positron beams. *Science*, 218(4570):335–340, 1982.

[44] A. P. Mills. Positronium molecule formation, bose einstein condensation and stimulated annihilation. *Nuclear Instruments and Methods in Physics Research Section B: Beam Interactions with Materials and Atoms*, 192:107–116, 2001.

[45] A. P. Mills, D. B. Cassidy, and R. G. Greaves. Prospects for making a bose einstein condensed positronium annihilation gamma ray laser. *Materials Science Forum*, 445–446:424–429, 2004.

[46] A. P. Mills and E. M. Gullikson. Solid neon moderator for producing slow positrons. *Applied Physics Letters*, 49(17):1121–1123, 1986.

[47] T. J. Murphy and C. M. Surko. Positron trapping in an electrostatic well by inelastic collisions with nitrogen molecules. *Physical Review A*, 46(9):5696–5705, 1992.

[48] T. Omori, M. Fukuda, T. Hirose, Y. Kurihara, R. Kuroda, M. Nomura, A. Ohashi, T. Okugi, K. Sakaue, T. Saito, J. Urakawa, M. Washio, and I. Yamazaki. Efficient propagation of polarization from laser photons to positrons through compton scattering and electron-positron pair creation. *Physical Review Letters*, 96(11):114801–114804, 2006.

[49] T. M. O'Neil. Trapped plasmas with a single sign of charge (from coulomb crystals to 2d turbulence and vortex dynamics). *Physics Today*, 52:24–30, 1999.

[50] T. M. O'Neil and D. H. E. Dubin. Thermal equilibria and thermodynamics of trapped plasmas with a single sign of charge. *Physics of Plasmas*, 5(6):2163–2193, 2001.

[51] N. Oshima, R. Suzuki, T. Ohdaira, A. Kinomura, T. Narumi, A. Uedono, and M. Fujinami. Brightness enhancement method for a high-intensity positron beam produced by an electron accelerator. *Journal of Applied Physics*, 103(9):094916–1–094916–7, 2008.

[52] T. S. Pedersen, A. H. Boozer, W. Dorland, J. P. Kremer, and R. Schmitt. Prospects for the creation of positron-electron plasmas in a non-neutral stellarator. *Journal of Physics B*, 36(5):1029–1039, 2003.

[53] A. J. Peurrung and J. Fajans. Non-neutral plasma shapes and edge profiles. *Physics of Fluids B*, 2(4):693–699, 1990.

[54] M. Reiser. *Theory and Design of Charged Particle Beams*. John Wiley and Sons, Inc., 1999.

[55] D. Schodlbauera, P. Sperra, G. Kogela, and W. Triftshausera. A pulsing system for low energy positrons. *Nuclear Instruments and Methods in Physics Research Section B*, 34(2):258–268, 1988.

[56] P. J. Schultz and K. G. Lynn. Interaction of positron beams with surfaces, thin films, and interfaces. *Review of Modern Physics*, 60(3):701–779, 1988.

[57] W. Stoeffl, P. Asoka-Kumar, and R. Howell. The positron microprobe at llnl. *Applied Surface Science*, 149:1–6, 1999.

[58] J. P. Sullivan, S. J. Gilbert, and C. M. Surko. Excitation of molecular vibrations by positron impact. *Physical Review Letters*, 86(8):1494–1497, 2001.

[59] C. M. Surko and R. G. Greaves. Emerging science and technology of antimatter plasmas and trap-based beams. *Physics of Plasmas*, 11(5):2333–2348, 2004.

[60] C. M. Surko, G. F. Gribakin, and S. J. Buckman. Low-energy positron interactions with atoms and molecules. *Journal of Physics B*, 38:R–57–R–126, 2005.

[61] C. M. Surko, M. Leventhal, W. S. Crane, A. Passner, F. Wysocki, T. J. Murphy, J. Strachan, and W. L. Rowan. Use of positrons to study transport in tokamak plasmas (invited). *Review of Scientific Instruments*, 57(8):1862–1867, 1986.

[62] R. Suzuki, T. Ohdaira, and T. Mikado. A positron lifetime spectroscopy apparatus for surface and near-surface positronium experiments. *Applied Surface Science*, 58(5–6):603–606, 2000.

[63] A. Uedono, S. F. Chichibu, Z. Q. Chen, M. Sumiya, R. Suzuki, T. Ohdaira, T. Mikado, T. Mukai, and S. Nakamura. Study of defects in gan grown by the two-flow metalorganic chemical vapor deposition technique using monoenergetic positron beams. *Journal of Applied Physics*, 90(1):181–186, 2001.

[64] J. Ullrich, R. Moshammer, A. Dorn, R. Dorner, L. Ph H. Schmidt, and H. Schmidt-Bocking. Recoil-ion and electron momentum spectroscopy: reaction-microscopes. *Reports on Progress in Physics*, 66(9):1463–1545, 2003.

[65] T. R. Weber, J. R. Danielson, and C. M. Surko. Energy spectra of tailored particle beams from trapped single-component plasmas. *Physics of Plasmas*, 16(5):057105–1–057105–8, 2009.

[66] J. Young. *Energy-resolved annihilation studies: Vibrational Feshbach resonances and positron-molecule bound states.* PhD thesis, University of California, San Diego, San Diego, 2007.

[67] J. A. Young and C. M. Surko. Charged particle motion in spatially varying electric and magnetic fields. *Nuclear Instruments and Methods in Physics Research Section B: Beam Interactions with Materials and Atoms*, 247(1):147–154, 2006.